Borehole Breakouts in Transversely Isotropic Posidonia Shale

Kumulative Dissertation zur Erlangung des akademischen Grades

"doctor rerum naturalium" (Dr. rer. nat.) in der

Wissenschaftsdisziplin Geologie

eingereicht an der

Mathematisch-Naturwissenschaftlichen Fakultät

der Universität Potsdam

von

Tobias Meier

Potsdam, den 15.12.2016

EIDESSTATTLICHE ERKLÄRUNG

Hiermit erkläre ich, Tobias Meier, an Eides statt, dass die vorliegende Arbeit an keiner anderen Hochschule eingereicht worden ist sowie selbstständig und ausschließlich mit den angegebenen Mitteln angefertigt wurde.

Tobias Meier

GUTACHTER

Prof. Dr. Georg Dresen (GFZ Potsdam, Universität Potsdam)

Prof. Dr. Michael Alber (Ruhr-Universität Bochum)

Prof. Dr. Andreas Henk (Technische Universität Darmstadt)

STATEMENT OF CONTRIBUTIONS

The cumulative thesis "Borehole Breakouts in Transversely Isotropic Posidonia Shale" consists of three peer-reviewed, published papers and one manuscript in preparation. In two out of three published papers as well as the manuscript under preparation the Ph.D. candidate is the first author. This fulfills the guidelines for a cumulative thesis of the Institute of Earth and Environmental Science at the Faculty of Science located at the University of Potsdam. The articles and the manuscript respectively made up single chapters (i.e., **Chapter 2.1**, **3**, **4**, **5**) including their own abstract, introduction, methodology, discussion, conclusion, and acknowledgement. In addition, a general introduction (**Chapter 1**), a conclusion (**Chapter 6**), and an outlook (**Chapter 7**) were written for this thesis exclusively. References of all citations are given at the end of this thesis.

The paper "*What Controls the Mechanical Properties of Shale Rocks? – Part I: Strength and Young's Modulus*" in **Chapter 2.1** was authored by Dr. Erik Rybacki. The Ph.D. candidate submitted data to the publication, coauthored and reviewed the manuscript. The paper deals with mechanical properties of different shales and lays the basis for the conducted research on borehole breakouts in Posidonia shale.

The papers "*Influence of Borehole Diameter on the Formation of Borehole Breakouts in black shale*" (**Chapter 3**) and "*Influence of Bedding Angle on Borehole Stability: A Laboratory Investigation of Transverse Isotropic Oil Shale*" (**Chapter 4**) were written entirely by the Ph.D. candidate. The presented data was obtained, analyzed and interpreted by the Ph.D. candidate. The co-authors reviewed early stages of the manuscript and made substantial improvements to the manuscripts.

The manuscript under preparation entitled "*Influence of True-Triaxial Loading Conditions on Borehole Breakouts in Isotropic Sandstone and Transversely Isotropic Shales*" (**Chapter 5**) was written entirely by the Ph.D. candidate. The presented data was obtained, analyzed and interpreted by the Ph.D. candidate. The co-authors reviewed early stages of the manuscript.

Paper overview in chronological order:

Influence of Borehole Diameter on the Formation of Borehole Breakouts in Black Shale

Authors: *T. Meier, E. Rybacki, A. Reinicke, G. Dresen*
Submitted: 12 April 2012 to the *International Journal of Rock Mechanics and Mining Sciences*
Available Online: *21 May 2013*
Printed: *September 2013, Volume 62, Pages 74 -85*

What Controls the Mechanical Properties of Shale Rocks? – Part I: Strength and Young's Modulus

Authors: *E. Rybacki, A. Reinicke, T. Meier, M. Makasi, G. Dresen*
Submitted: *4 June 2015* to the *Journal of Petroleum Science and Engineering*
Available Online: *26 October 2015*
Printed: *November 2015, Volume 13, Pages 702 -722*

Influence of Bedding Angle on Borehole Stability: A Laboratory Investigation of Transverse Isotropic Oil Shale

Authors: *T. Meier E. Rybacki, T. Backers, G. Dresen*
Submitted: *25 May 2014* to *Rock Mechanics and Rock Engineering*
Available Online: *26 September 2014*
Printed: *July 2015, Volume 48, Issue 4, Pages 1535 -1546*

Influence of True-Triaxial Loading Conditions on Borehole Breakouts in Isotropic Sandstone and Transversely Isotropic Shales

Authors: *T. Meier, B. Haimson, E. Rybacki, G. Dresen*
In Preparation: *International Journal of Rock Mechanics and Mining Sciences*

DECLARATION

This work was funded by the GeoEn Project of the Federal Ministry of Education and Research in Germany (BMBF, Förderkennzeichen: 03G0671A-C) and supported by the GASH (Gas Shales in Europe) project, which are gratefully acknowledged.

Experimental work and analyses presented in this thesis were mainly done by the Ph.D. candidate (Tobias Meier). Work performed by others is clearly indicated, quoted as references and kindly acknowledged. Collaborative researchers are listed as co-authors in each article. All experiments and analytical investigations were conducted at the GeoForschungsZentrum (GFZ) Potsdam, Germany and the University of Wisconsin-Madison, Madison, United States of America. Experiments involving the Paterson-type high temperature, high pressure deformation apparatus were conducted by Michael Naumann (GFZ). The Ph.D. candidate, Stefan Gehrmann (GFZ) and Mathias Kreplin (GFZ) conducted the specimen preparation. Thin sections were prepared by Stefan Gehrmann. X-ray diffraction analyses were conducted by Hans-Peter Nabein (GFZ). X-ray Computer Tomography scans were carried out by Erik Rybacki (GFZ). Scanning Electron Microscopy (SEM) was supported by Ilona Shäpan (GFZ) and Erik Rybacki. Luiz Morales (now ETH Zürich) prepared SEM images of Focused-Ion Beam (FIB) sections.

DANKSAGUNG

In erster Linie möchte ich mich bei Herrn Prof. Dr. Georg Dresen für die Möglichkeit bedanken, die Doktorarbeit in der Sektion Geomechanik und Rheologie des Helmholtz-Zentrum Potsdam, Deutsches GeoForschungsZentrum (GFZ) durchzuführen. Seine fokussierte, engagierte Art zu arbeiten, ist ein Leitbild wissenschaftlichen Handelns geworden und ich bin froh, das über die Jahre aus dem „Sie“ ein „Du“ geworden ist. Danke.

Bei Dr. Erik Rybacki (GFZ) kann ich mich nicht genug bedanken für seine permanente Unterstützung und bei der Kontrolle meiner Manuskripte. Unvergessen bleibt mir unsere Probennahme mit Stefan Gehrmann im Süddeutschen. Letzterem sei gedankt für die exzellente Probenpräparation, den unterstützenden Gesprächen und dem ständigen Interesse an meiner Arbeit. An dieser Stelle auch ein großes Dankeschön an Matthias Kreplin (GFZ). Ich melde mich wenn ich eine Möglichkeit gefunden habe „etwas ranschleifen“ zu können.

Dr. Sergei Stanchits sei gedankt für seine unermüdliche Arbeit und der Einführung in die MTS.

Michael Naumann (GFZ), dein Witz und deine positive Energie haben mich immer motiviert. Ein großer Dank gebührt Dir für die Durchführung vieler Hochdruck-Experimente an der Paterson-Apparatur, deiner durchdenkenden Tatkraft und dem Bewusstsein jederzeit auf dich bauen zu können, wenn etwas nicht funktioniert.

Ein großes Kompliment für ihre Unterstützung all meinen ehemaligen Mitdoktoranden und Kollegen in der Sektion und bei der geomecon: Andreas, Carina, Eva, Frank, Masline, Peter, Rita, Sara, Simon, und Vanessa. Die Doktorandenzeit wäre nur halb so schön ohne euch gewesen.

Bei Prof. erim. Dr. Bezalel Haimson bedanke ich mich für die Möglichkeit Versuche in der Universität Wisconsin-Madison durchzuführen. Der Aufenthalt in den USA war ein großer Meilenstein in meinem Leben und ich möchte mich dafür bei allen Beteiligten, die das ermöglicht haben, sehr bedanken.

Dr. Tobias Backers. Ich verdanke Dir zu viel, um es hier aufzuführen. Das besprechen wir beim Bier.

Meinen lieben Eltern gebührt der größte Dank. Ohne euch wäre all das nicht möglich gewesen.

Meiner Frau – *bisous!*

ABSTRACT

Borehole instabilities are frequently encountered when drilling through finely laminated, organic rich shales (Økland and Cook, 1998; Ottesen, 2010; etc.); such instabilities should be avoided to assure a successful exploitation and safe production of the contained unconventional hydrocarbons. Borehole instabilities, such as borehole breakouts or drilling induced tensile fractures, may lead to poor cementing of the borehole annulus, difficulties with recording and interpretation of geophysical logs, low directional control and in the worst case the loss of the well. If these problems are not recognized and expertly remedied, pollution of the groundwater or the emission of gases into the atmosphere can occur since the migration paths of the hydrocarbons in the subsurface are not yet fully understood (e.g., Davies et al., 2014; Zoback et al., 2010). In addition, it is often mentioned that the drilling problems encountered and the resulting downtimes of the wellbore system in finely laminated shales significantly increase drilling costs (Fjaer et al., 2008; Aadnoy and Ong, 2003).

In order to understand and reduce the borehole instabilities during drilling in unconventional shales, we investigate stress-induced irregular extensions of the borehole diameter, which are also referred to as borehole breakouts. For this purpose, experiments with different borehole diameters, bedding plane angles and stress boundary conditions were performed on finely laminated Posidonia shales. The Lower Jurassic Posidonia shale is one of the most productive source rocks for conventional reservoirs in Europe and has the greatest potential for unconventional oil and gas in Europe (Littke et al., 2011).

In this work, Posidonia shale specimens from the North (PN) and South (PS) German basins were selected and characterized petrophysically and mechanically. The composition of the two shales is dominated by calcite (47-56%) followed by clays (23-28%) and quartz (16-17%). The remaining components are mainly pyrite and organic matter. The porosity of the shales varies considerably and is up to 10% for PS and 1% for PN, which is due to a larger deposition depth of PN. Both shales show marked elasticity and strength anisotropy, which can be attributed to a macroscopic distribution and orientation of soft and hard minerals. Under load the hard minerals form a load-bearing, supporting structure, while the soft minerals compensate the deformation. Therefore, if loaded parallel to the bedding, the Posidonia shale is more brittle than loaded normal to the bedding. The resulting elastic anisotropy, which can be defined by the ratio of the modulus of elasticity parallel and normal to the bedding, is about 50%, while the strength anisotropy (i.e., the ratio of uniaxial compressive strength normal and parallel to the bedding) is up to 66%. Based on the petrophysical characterization of the two rocks, a transverse isotropy

(TVI) was derived. In general, PS is softer and weaker than PN, which is due to the stronger compaction of the material due to the higher burial depth.

Conventional triaxial borehole breakout experiments on specimens with different borehole diameters showed that, when the diameter of the borehole is increased, the stress required to initiate borehole breakout decreases to a constant value. This value can be expressed as the ratio of the tangential stress and the uniaxial compressive strength of the rock. The ratio increases exponentially with decreasing borehole diameter from about 2.5 for a 10 mm diameter hole to ~ 7 for a 1 mm borehole (increase of initiation stress by 280%) and can be described by a fracture mechanic based criterion. The reduction in borehole diameter is therefore a considerable aspect in reducing the risk of breakouts. New drilling techniques with significantly reduced borehole diameters, such as "fish-bone" holes, are already underway and are currently being tested (e.g., Xing et al., 2012).

The observed strength anisotropy and the TVI material behavior are also reflected in the observed breakout processes at the borehole wall. Drill holes normal to the bedding develop breakouts in a plane of isotropy and are not affected by the strength or elasticity anisotropy. The observed breakouts are point-symmetric and form compressive shear failure planes, which can be predicted by a Mohr-Coulomb failure approach. If the shear failure planes intersect, conjugate breakouts can be described as "dog-eared" breakouts.

While the initiation of breakouts for wells oriented normal to the stratification has been triggered by random local defects, reduced strengths parallel to bedding planes are the starting point for breakouts for wells parallel to the bedding. In the case of a deflected borehole trajectory, therefore, the observed failure type changes from shear-induced failure surfaces to buckling failure of individual layer packages. In addition, the breakout depths and widths increased, resulting in a stress-induced enlargement of the borehole cross-section and an increased output of rock material into the borehole. With the transition from shear to buckling failure and changing bedding plane angle with respect to the borehole axis, the stress required for inducing wellbore breakouts drops by 65%.

These observations under conventional triaxial stress boundary conditions could also be confirmed under true triaxial stress conditions. Here breakouts grew into the rock as a result of buckling failure, too. In this process, the broken layer packs rotate into the pressure-free drill hole and detach themselves from the surrounding rock by tensile cracking. The final breakout shape in Posidonia shale can be described as trapezoidal when the bedding planes are parallel to the greatest horizontal stress and to the borehole axis. In the event that the largest horizontal stress is normal to the stratification, breakouts were formed entirely by shear fractures between the stratification and required higher stresses to initiate similar to breakouts in conventional triaxial experiments with boreholes oriented normal to the bedding.

In the content of this work, a fracture mechanics-based failure criterion for conventional triaxial loading conditions in isotropic rocks (Dresen et al., 2010) has been successfully extended to true triaxial loading conditions in the transverse isotropic rock to predict the initiation of borehole breakouts. The criterion was successfully verified on the experiments carried out.

The extended failure criterion and the conclusions from the laboratory and numerical work may help to reduce the risk of borehole breakouts in unconventional shales.

ZUSAMMENFASSUNG

Bei Bohrungen in feinlaminierten, organikreichen Schiefern werden häufig Bohrlochinstabilitäten beobachtet (Økland und Cook, 1998; Ottesen, 2010 und weitere), welche für eine sichere und erfolgreiche Erschließung der darin gespeicherten unkonventionellen Kohlenwasserstoffe vermieden werden sollten. Bohrlochinstabilitäten, wie zum Beispiel Bohrlochrandausbrüche oder bohrungsbedingte Zugrisse, führen unter Umständen zu einer schlechten bzw. unzureichenden Zementierung des Ringraum, zu Schwierigkeiten bei der Aufnahme und späteren Interpretation bohrlochgeophysikalischer Messungen sowie zu einer verringerten Kontrolle über die Auslenkung der Bohrung und im schlimmsten Fall zum Verlust der Bohrung. Werden diese Probleme nicht erkannt und fachmännisch behoben, kann es zur Verschmutzung des Grundwassers oder zum Austritt von Gasen in die Atmosphäre kommen, da die Migrationspfade der Kohlenwasserstoffe im Untergrund noch nicht vollständig verstanden sind (z.B. Davies et al., 2014; Zoback et al., 2010). Darüber hinaus wird häufig erwähnt, dass die angetroffenen Bohrprobleme und die daraus entstehenden Ausfallzeiten der Bohrlochanlage in feinlaminierten Schiefern die Bohrkosten erheblich erhöhen (Fjaer et al., 2008; Aadnoy und Ong, 2003).

Um die Bohrlochinstabilitäten während des Bohrens in unkonventionellen Speichergesteinen zu verstehen und zu reduzieren, untersuchen wir in dieser Arbeit spannungsbedingte unregelmäßige Erweiterungen des Bohrlochdurchmessers, die auch als Bohrlochrandausbrüche (borehole breakouts) bezeichnet werden. Dazu wurden Versuche mit unterschiedlichen Bohrlochdurchmessern, Schichteinfallswinkeln und Belastungsrandbedingungen an feinlaminierten Posidonienschiefern durchgeführt. Der aus dem Unteren Jura stammende Posidonienschiefer ist eines der produktivsten Muttergesteine für konventionelle Lagerstätten in Europa und besitzt zeitgleich das größte Potential für unkonventionelles Öl und Gas in Europa (Littke et al., 2011).

Im Rahmen dieser Arbeit wurden Posidonienschieferproben aus dem Norddeutschen (PN) und Süddeutschen (PS) Becken ausgewählt und petrophysikalisch sowie mechanisch charakterisiert. Die Zusammensetzung der beiden Schiefer wird dominiert von Kalzit (47-56%) gefolgt von Tonen (23-28%) und Quarz (16-17%). Die verbleibenden Komponenten sind hauptsächlich Pyrit und organische Substanz. Die Porosität des Schiefers schwankt beträchtlich und beträgt bis zu 10% für PS und 1% für PN, was auf eine größere Versenkungstiefe von PN zurückzuführen ist. Beide Schiefer zeigen ausgeprägte Elastizitäts- und Festigkeitsanisotropie, welche einer makroskopischen Verteilung und Orientierung von weichen und harten Mineralen zugeschrieben werden kann. Unter Belastung bilden die harten Minerale eine tragende Struktur, während die

weichen Minerale die Verformung kompensieren. Daher verhält sich der Posidonienschiefer bei Belastung parallel zur Schichtfläche spröder als bei einer Belastung normal zur Schichtfläche. Die resultierende elastische Anisotropie, die über das Verhältnis des Elastizitätsmoduls parallel und normal zu Schichtung definiert werden kann, beträgt circa 50%, während die Festigkeitsanisotropie (d.h. das Verhältnis der uniaxialen Druckfestigkeit normal und parallel zur Schichtung) bis zu 66% beträgt. Basierend auf der petrophysikalischen Charakterisierung der beiden Gesteine konnte eine transversale Isotropie (TVI) abgeleitet werden. Im Allgemeinen ist PS weicher und schwächer als PN, was auf der stärkeren Verdichtung des Materials aufgrund der höheren Versenkungstiefe beruht.

Konventionelle triaxiale Experimente zur Entstehung von Bohrlochrandausbrüchen an Proben mit unterschiedlichen Bohrlochdurchmessern zeigten, dass bei Vergrößerung des Bohrlochdurchmessers die zum Auslösen des Randausbruches erforderliche Spannung gegen einen konstanten Wert absinkt. Dieser kann als Verhältnis der Tangentialspannung und der einachsialen Druckfestigkeit des Gesteins ausgedrückt werden. Das Verhältnis erhöht sich exponentiell mit kleiner werdendem Bohrlochdurchmesser von circa 2,5 für ein 10 mm großes Bohrloch auf ~7 für ein 1 mm großes Bohrloch (Zunahme der Initiierungsspannung um 280%) und kann durch ein bruchmechanisch basiertes Kriterium beschrieben werden. Die Verringerung des Bohrlochdurchmessers stellt daher einen beträchtlichen Aspekt bei der Verringerung des Risikos für Bohrlochausbrüche dar. Neue Bohrtechniken mit deutlich reduzierten Bohrlochdurchmessern wie zum Beispiel „fish-bone“ Bohrungen nehmen dieses Konzept bereits auf und werden derzeit getestet (z. B. Xing et al., 2012).

Die beobachtete Festigkeitsanisotropie und das TVI Materialverhalten spiegeln sich auch in den beobachteten Ausbruchsprozessen am Bohrlochrand wider. Bohrlöcher normal zur Schichtung entwickeln Randausbrüche in einer Ebene der Isotropie und werden nicht durch die Festigkeits- oder Elastizitätsanisotropie beeinflusst. Die beobachteten Ausbrüche sind punktsymmetrisch und bilden kompressive Schubversagensebenen, die durch einen Mohr-Coulomb-Versagensansatz vorhergesagt werden können. Falls sich die Schubversagensebenen schneiden, bilden sich konjugierte Ausbrüche die als „hundeohrförmig“ (dog-eared breakout) beschrieben werden können.

Während die Initiierung von Randausbrüchen für Bohrlöcher normal zur Schichtung durch zufällige lokale Defekte ausgelöst wurde, sind reduzierte Festigkeiten parallel zur Schichtung der Ausgangspunkt für Bohrlochrandausbrüche für Bohrlöcher parallel zur Schichtung. Im Falle einer abgelenkten Bohrlochtrajektorie ändert sich daher der beobachtete Versagenstyp von schubdominiertem Versagensflächen zu Knickversagen einzelner Schichtpakete. Darüber hinaus nahmen die Ausbruchtiefen und -breiten zu, was zu einer spannungsbedingten Vergrößerung des Bohrlochquerschnitts und einem vermehrten Ausstoß von Gesteinsmaterial in das Bohrloch führte. Zeitgleich sinkt beim Übergang von Schub- zu Knickversagen und sich ändernden Schichteinfallswinkel, die für das Induzieren von Bohrlochrandausbrüchen notwendige Spannung um 65%, deutlich ab.

Diese Beobachtungen unter konventionellen triaxialen Belastungsrandbedingungen konnten auch unter echt-triaxialen Belastungsrandbedingungen bestätigt werden. Hier wuchsen die Randausbrüche ebenfalls normal zur Schichtfläche durch Knickfehler in das Gestein. Dabei rotierten die gebrochenen Schichtpakete in das druckfreie Bohrloch und lösten sich vom umgebenden Gestein durch Zugrisse ab. Die endgültige Ausbruchform im Posidonienschiefer kann als trapezförmig beschrieben werden, wenn die Schichtfläche parallel zur größten horizontalen Spannung liegt. In dem Fall, dass die größte horizontale Spannung normal zur Schichtung orientiert ist, wurden Ausbrüche vollständig durch Scherbrüche zwischen den Schichtflächen gebildet und benötigten höhere Spannungen zur Initiierung.

Im Rahmen dieser Arbeit wurde ein bruchmechanisch-basiertes Versagenskriterium für konventionelle triaxiale Belastungsbedingungen in isotropen Gesteinen (Dresen et al., 2010) erfolgreich auf echte triaxiale Belastungsbedingungen im transversal isotropen Gestein erweitert, um die Initiierung von Bohrlochrandausbrüchen vorherzusagen. Das Kriterium konnte erfolgreich an den durchgeführten Versuchen verifiziert werden.

Das erweiterte Versagenskriterium und die Schlussfolgerungen aus dem Labor und der numerischen Arbeit helfen, das Risiko von Bohrlochausbrüchen in unkonventionellen Schiefern zu reduzieren.

CONTENTS

NOMENCLATURE

α	bedding plane dip
β	angle of attack (90°- α)
γ	angle between SH and bedding
ε	strain
$\dot{\varepsilon}$	strain rate
θ	angle measured counter clockwise from SH
μ	friction coefficient
ν	(static) Poisson's ratio
σ_{max}	(confined) peak (differential) strength
σ_t	(unconfined) tensile strength (St)
σ_c	uniaxial (unconfined) compressive strength
σ_n	normal stress
τ	shear stress
Φ	porosity
ω	breakout angle
a	borehole radius
ALM	Alum shale
AE	acoustic emission
b	specimen radius
BAR	Barnett shale
BST	Bentheim sandstone
c	half crack length
C	cohesion
C_w	bedding plane cohesion
C_{bulk}	bulk modulus
CAR	Carrara marble
COA	bituminous coal
ClyTOC	clay+TOC
CT	Computer tomography
Cly	clay
Cb	carbonate
d	grain size
DOT	Dotternhausen (Posidonia) shale (PS)
e	strain
E	(static) Young's modulus
Fsp	feldspar
FST	Flechtingen sandstone
f_i	volume fraction of phase i
HAD	Haddessen (Posidonia) shale
HAR	Harderode (Posidonia) shale (PN)
HC	hollow cylinder
G	(static) shear modulus
GAB	Panzhihua gabbro
GMR	general mixture rule with empirical parameters s and sp
GRA	Westerly granite
K_{IC}	mode I fracture toughness
l	specimen length
LIM	Solnhofen limestone
LSB	lower strength bound
M	material property
MIP	mercury injection porosimetry
NOV	Arkansas novaculite
$P = P_o$	confining pressure
P*	critical confining pressure
P_ε	P* based on strain measurement
P_{AE}	P* based on acoustic emission
P_{amp}	P* based on ultrasonic amplitude
$P_{closure}$	crack closure pressure
P_{Cbulk}	P* based on bulk modulus
P_{CT}	P* based on CT observations
P_{vp}	P* based on ultrasonic velocity
PN	Posidonia shale from N Germany (HAR)
PS	Posidonia shale from S Germany (DOT)
Py	pyrite
Px	pyroxene
QFP	Qtz+Fsp+Py
Qtz	quartz
r	distance from borehole wall
R^2	Coefficient of determination
Rm	maturity (R_o)
Ro	maturity (R_m)
Sh	minimum horizontal stress
SH	maximum horizontal stress
St	tensile strength (σ_t)
SV	vertical stress
TOC	total organic carbon content
TWHC	thick-walled hollow cylinder
UCS	uniaxial (unconfined) compressive strength
USB	upper strength bound
VRr	vitrinite reflectance
WIC	Wickensen (Posidonia) shale

subscript cp porous composite (index c)
subscript cnop non-porous composite (index c)
subscripts p, xy loading parallel to bedding orientation
subscripts n, z loading normal to bedding orientation
superscript* property normalized to 0% porosity

X, Y, Z	global coordinate system
x, y, z	material coordinate system
r, θ, z	cylindrical coordinate system
l, m, n	direction cosines

1 GENERAL INTRODUCTION

Since the shale oil and shale gas boom in the United States (U.S.) of America more countries re-investigate their unconventional oil and gas shale potential. According to reports by the U.S. Energy Information Administration (EIA) the unconventional plays in the U.S. have proven that gas and oil can be produced rapidly from these resources by the usage of new extraction technologies (EIA, 2015). Common production techniques used for conventional fields are not applicable due to the almost impermeable shale matrix. Hence, long horizontal wells are required to expose as much of the oil and gas bearing shale matrix as possible (e.g., Fuller & Meehan, 2010). Additional massive hydraulic stimulation, reactivate pre-existing fractures and create new fractures that provide migration pathways and thereby increase the permeability of the shale (Boyer et al., 2006).

The "oil and gas shale revolution" led to independence of the U.S. from oil and gas imports and transformed the world's largest economy to an exporting oil country. "Because they have proven to be quickly producible in large volumes at a relatively low cost, tight oil and shale gas resources have revolutionized U.S. oil and natural gas production, providing 29 percent of total U.S. crude oil production and 40 percent of total U.S. natural gas production in 2012" (EIA, 2015). And in 2015 the EIA claims that in 2028 the U.S. will be in balance between energy import and export and predicts a "transition from a net importer to a net exporter of natural gas and petroleum in the next decades due to increasing domestic production from tight formations" (Conti et al., 2015).

The thereby induced changes affect the worldwide oil price and the geopolitical situation dramatically as the independence of oil and gas imports will affect the way once oil consuming countries looked at oil producing countries. This is a threat not only to the financial and political stability of oil producing (e.g., Saudi Arabia, Russia, Venezuela) but also to the linked wealth of oil-consuming countries (e.g., Germany, Japan). Furthermore, it has been argued that the U.S. will step back in "securing" oil producing countries in the Middle East (Helm, 2013). The high production rate of the oil producing countries (OPEC) can be regarded as a first sign.

It is therefore of utmost importance for importing countries to examine their unconventional oil and gas potential in order to secure its oil and gas supply and maintain its productivity and stability. Furthermore, by looking at the potential of unconventional resources the negotiation position for oil and gas pricing can be strengthened. In the particular case of Germany, shale gas would be a good and comparable clean additive to the uprising renewable energies. According to

Andruleit et al. (2012) about 13 trillion m^3 shale gas are in place in Germany from which approximately 10% (1.3 trillion m^3) are recoverable. These resources exceed the conventional gas resources by a factor of 10 and can be an important contribution to the transition from fossil and nuclear to renewable energy in the context of the “Energiewende”.

To successfully exploit these resources all drilling related problems have to be analyzed and minimized. However, problems related to borehole instabilities have been barely addressed for unconventional oil and gas shales. Instead most of the related research is about borehole stability issues when drilling wells through shales which are not considered as unconventional (see for example Ottesen, 2010 and references therein; Økland and Cook, 1998; Blümling et al., 2007; etc.). The reported problems are vast and encompass for example mud loss, stuck pipe, reaming and the necessity to side-track a lost hole as for example documented in high-angle wells drilled in an organic-rich shale formation in the North Sea by Økland and Cook (1998). These problems significantly increase the downtime in drilling and the costs per well. According to Aadnoy and Ong (2003), at least 10% of the well budget has to be spent on unplanned operations stemming from wellbore instability problems.

1.1 Borehole Breakouts

This thesis deals with stress-induced enlargements of the borehole diameter due to compressive failure, called borehole breakouts (see Figure 1.1a). Breakouts are oriented normal to the maximum far field stress acting in a plane normal to the borehole axis (S_1 in Figure 1.1b), e.g., normal to the maximum horizontal stress if the borehole is vertical, and can be observed by different logging tools from which caliper log (see Figure 1.1b) or acoustic borehole televiewer (Figure 1.1c) are the most common techniques (see Ask and Ask, 2007).

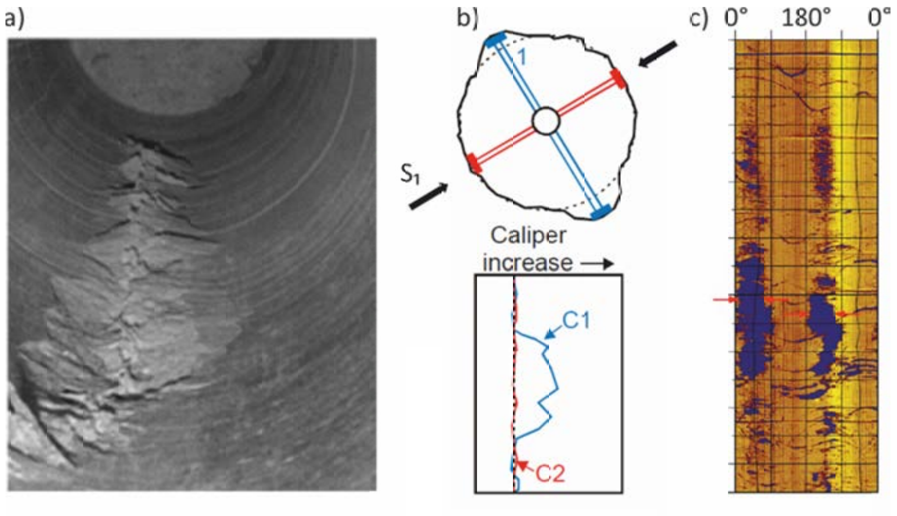

Figure 1.1 Ways of identifying borehole breakouts. a) Visual inspection of a borehole breakout (taken from Haimson 2007), b) observation of a breakout based on caliper log (taken from Plumb and Hickmann 1985), and c) bottom hole televiewer amplitude log (taken from Ask and Ask 2007).

Borehole breakouts have been proven to be reliable indicators for the direction of the maximum horizontal stress and are frequently used to determine the orientation of the stress field. The World Stress Map contains some 4125 data point's worldwide based on breakout orientation measurements (www.world-stress-map.org; Heidbach et al., 2008), which is the second largest contribution to the existing data set. Their wide spread use for stress field orientation and stress field determination is based on the so-called "Kirsch Equations" (Kirsch, 1898), which provide an analytical solution for the stress field in the vicinity of a hole located in an infinite plate under external stress. In general, these equations provide the possibility to calculate the borehole tangential and radial stress, which fluctuate up to a distance of approx. 3 times the borehole radius around the borehole in dependency to the far field stress (see for example Timoshenko and Goodier, 2010; Jaeger et al., 2007; Zoback, 2010). The theory behind the concept of a borehole being a concentrator for stress is described also in **Chapter 3** and **5** providing the equations for the stress field around a hole located in an infinite plate loaded under conventional triaxial and true-triaxial loading conditions, respectively.

It was Bell and Gough (1979) who proposed that borehole breakouts would occur in wells in case the tangential stress exceeds the compressive strength of the rock. Their analysis of observed breakouts in wells in Alberta (Canada) was the first interpretation of breakouts based on the stress field. Since then the breakout theory has been extended and successfully applied to a variety of borehole orientations (e.g., Mastin, 1988), rock types (e.g., Zoback et al., 1985; Zoback, 2010), anisotropic rocks (see for example Amadei and Stephansson, 1997; Pei, 2008), temperature and pore pressure effects (see Schmitt et al., 2012 and reference therein) or various failure criteria (e.g., Gholami et al., 2014; Rahimi, 2014; Zang and Stephansson, 2012). The theory became a part of a Suggested Method for the rock stress estimation in the International Society of Rock Mechanics (ISRM SM, Stephansson and Zang, 2012).

Different breakout types have been reported so-far ranging from cusp and dog-ear shaped failures in low- to medium porous sandstone, limestones and granites to slot-like breakouts in high porous sandstone (Cuss et al., 2003; Gay, 1973; Haimson, 2007). When drilling in shale, breakouts are frequently reported to cause trouble in deviated wells. In particular, during angle built-up as the borehole trajectory deviates from vertical, i.e., normal to the bedding, to horizontal, i.e., parallel to the bedding (Økland and Cook, 1998). A change in the borehole trajectory is always related to a change in the stress field acting on the borehole (e.g., Al-Ajmi and Zimmerman, 2009) but applies to all rocks in the same manner. The problems must therefore be related to the anisotropic nature of shales that can be quantified by measuring elastic parameters (e.g., Vernik and Lui, 1997; Dewhurst and Siggins, 2005; Johnston and Christensen, 1995) and strength parameters (e.g., Horsrud et al., 1998; Sone and Zoback, 2013a; Aoki et al., 1993). With regard to the bedding orientation, these parameters might vary significantly with the lowest strength and highest stiffness parallel to the bedding. This change in strength and elastic properties causes unpredictable problems for the drillers if the strength and elastic properties of the shale in bedding parallel and normal direction have not been determined beforehand (e.g., Zoback, 2007).

As the borehole changes from vertical to parallel to the bedding the strength of the shale might reduce considerably, inducing severe breakouts with all the related drilling problems. But not only is the drilling at risk. Also post drilling operations like logging might be severely affected due to very uneven borehole walls, no centered tools or no contact of tools with the borehole wall. The biggest threat however is the risk of contamination. According to Zoback et al. (2010): “Failure of the cement or casing surrounding the wellbore poses a far greater risk to water supplies. If the annulus is improperly sealed, natural gas, fracturing fluids, and formation water containing high concentrations of dissolved solids may be communicated directly along the outside of the wellbore among the target formation, drinking water aquifers, and layers of rock in between. For example, in 2007, a well that had been drilled almost 4,000 feet into a tight sand formation in Bainbridge (Ohio) was not properly sealed with cement, allowing gas from a shale layer above the target tight sand formation to travel through the annulus into an underground source of drinking water. The methane eventually built up until an explosion in a resident‘s basement alerted state officials to the problem.”

A variety of tools and tests have been developed to check the integrity of casing and cement jobs (Zoback et al., op. cit.), however, the best way to prevent accidents such as in Bainbridge would be to avoid borehole instabilities, which always possess the risk of being potential migration pathways.

1.2 Motivation & Structure

The main goal of this work is to improve the understanding of borehole breakouts in unconventional oil and gas shale in order to a) assure the dimensional accuracy of the well, b) reduce the operational downtime and thereby the cost per well, c) increase the quality of geophysical logs and d) to assure a tight cementation in the annulus. The following questions can be motivated a priori and will be answered synoptically in **Chapter 6**:

1) What are the geomechanical properties controlling borehole instabilities in unconventional shales?
2) How can the dimensional accuracy of the well be assured and the risk for borehole breakouts minimized in unconventional shales?
3) Can breakouts in shales be used to derive the orientation and magnitude of the maximum horizontal stress?

Therefore, the experimental investigation has been divided into four separate parts, which built up on each other and each addressing specific tasks to answer the aforementioned questions. Firstly in **Chapter 2** the mechanical properties of the rock at hand and other European oil and gas shales are investigated under different pressure and temperature conditions to classify the behavior of the rock. The full characterization of the rock lays the basis for any sound borehole stability evaluation or laboratory testing campaign. Secondly in **Chapter 3**, conventional triaxial experiments are performed on thick-walled hollow cylinders with the borehole normal to the bedding plane to investigate the influence of the borehole diameter on the breakout initiation stress under isotropic material behavior. Thirdly in **Chapter 4**, thick-walled hollow cylinder experiments with varying bedding plane orientation are carried out to monitor the changes in breakout mechanics and initiation stresses by moving towards transverse isotropic material behavior. And in **Chapter 5**, true-triaxial experiments are conducted with the bedding planes parallel to the borehole. Those experiments simulate in situ conditions and represent the highest complexity as anisotropic stresses and material properties need to be considered.

This workflow ensures that the complexity of a borehole planned in unconventional shales in terms of borehole stability can be addressed at each stage of its appraisal. It also ensures that the genesis of the most complicated breakout pattern can still be explained.

Borehole stability problems might also arise due to chemical processes, like swelling, ballooning, washouts or sloughing as for example summarized by van Oort (2003). However, those effects as well as drilling-related processes like key seats are beyond the scope of this work.

2 UNCONVENTIONAL OIL AND GAS SHALE

Oil and gas shale are organic-rich fine-grained sedimentary rock (Curtis, 1980) from which liquid or gaseous hydrocarbons, called shale oil or shales gas, respectively, can be produced. The matrix of the shale mainly consists of a mixture of organic carbon, clay, quartz, and calcite (Füchtbauer, 1988).

The reservoir from which shale oil and shale gas are produced is defined by low permeability and porosity and thereby set itself apart from conventional reservoirs with higher permeability and porosity even though unconventional shales might contain fissure or show a high fissility arising from lamination (Curtis, 1980; Fürchtbauer, 1988). Furthermore, the shale oil and shale gas was originated and trapped in this rock and the reservoir becomes its own source. Such a reservoir is a counterpart to a conventional reservoir and therefore termed unconventional reservoir. There are other unconventional reservoirs, like tight sands or coal beds (e.g., Cander, 2012), however, in the context of this work unconventional reservoirs are an alias for oil and gas shale.

The best conditions for exploiting such an unconventional reservoir have been summarized for petrophysical parameters (e.g., Boyer et al., 2006; Horsfield and Schulz, 2010; Kerschke and Schulz, 2015). For example, Horsfield and Schulz (2010) state that the reservoir should have a thickness greater than 20 m and buried at depth less than 4 km. From a petrophysical point of view Boyer et al. (2006) mentions that porosity should be greater than 4% and permeability greater 100 nD for successful production, which is in line with the maximum permeability of 0.001 mD to define unconventional shales according to the EIA (2013a). The total organic content (TOC) should be greater than 2% and the maturity should lie in between 1.2% to 3.3% (Boyer et al., 2006; Horsfield and Schulz, 2010).

As the boom in “unconventionals” started about a decade ago, geomechanical data of these rocks are rare. Their striking geomechanical features are their narrow spaced bedding planes, resulting in planes of weaknesses along which the shale can split. The elastic properties of the reservoir, which can be a function of the composition of the rock, do also play a significant role once the reservoir has been proven a resource as they determine whether or not the shale oil and shale gas can be extracted economically by hydraulic fracturing. However, the heterogeneous nature and the large variety of rocks summarized under the term unconventional shale, made approaches to link the strength and elastic properties with petrophysical parameters cumbersome.

In the following subchapter, we characterize geomechanical and petrophysical parameters of some European oil and gas shale, highlighting the complexity of unconventional shale and laying the basis for any borehole stability analysis. Especially the differences in the elastic and strength parameters of the rock with respect to the bedding plane angle are of high importance for the evaluation of the onset stress for borehole breakouts.

For example, with increasing elastic anisotropy, which is given by the ratio of the Young's modulus normal and parallel to the bedding, the stress distribution around the borehole deviates from the stress distribution commonly calculated for isotropic rocks (Blümling, 1986; Aadnoy, 1989; Gaede et al., 2012). According to Blümling (1986) the error by neglecting anisotropic elasticity is significant for ratios larger than three and might lead to wrong assumptions for the stress field around the borehole. On the other hand, with increasing anisotropy in strength, e.g. uniaxial compressive strength, breakouts might initiate at much lower stresses or forming much larger cavities than predicted by using isotropic material strength (Zoback, 2010; Daemen, 1983; etc.). Therefore, linking geomechanical parameters with other petrophysical parameters and reservoir conditions helps to forecast the rock behavior under in-situ conditions and is crucial when predicting the stability in "unconventionals".

2.1 What Controls the Mechanical Properties of Shale Rocks? - Part I: Strength and Young's Modulus[1]

SUMMARY

We performed mechanical tests on several, mainly European black shales with different mineralogical composition, porosity and maturity. The uniaxial and triaxial compressive strength, tensile strength and static Young's modulus were measured at varying confining pressures, temperatures and strain rates. Mechanical properties such as compressive strength and elastic moduli strongly depend on shale composition, porosity and water content, as well as pressure (*P*) and temperature (*T*) conditions, but less on strain rate. The shales are orthotropic as strength and elastic properties vary with bedding orientation to the loading direction. We found a transition from brittle to semibrittle deformation at high *P*–*T* conditions, in particular for high-porosity shales. In the predominantly brittle regime up to about 100 MPa pressure, the compressive strength increases non-linearly with increasing pressure and correlates almost linearly with Young's modulus. The internal friction coefficients vary substantially between ≈ 0.2 and 1.1 for the investigated shales. The effect of strain rate and temperature on peak strength can be described by a power or exponential law constitutive equation with a strain rate sensitivity typical for brittle rocks and a temperature sensitivity inferring to dislocation glide of clay minerals. Ignoring the influence of water and structural anisotropy, at given *P*–*T* conditions the variation of compressive strength and Young's modulus with composition for a specific shale formation may be roughly estimated from the volumetric proportion of all constituents and pores using a generalized mixture rule (GMR) approach. In contrast, this model cannot be used to approximate the tensile strength.

2.1.1 Introduction

In recent years, the exploitation of unconventional hydrocarbon reservoirs strongly increased, in particular in North America (e.g., McGlade et al., 2013). Unconventional resources are characterized by low rock permeability, for example oil and gas shales or tight sandstones and carbonates (McGlade et al., 2013). To be economically attractive, advanced stimulation techniques, like hydraulic fracturing and drilling of long horizontal boreholes, are required to achieve economic production rates. In order to keep the artificially induced fractures open,

---

[1] E. Rybacki, A. Reinicke, T. Meier, M. Makasi, G. Dresen, What controls the mechanical properties of shale rocks? – Part I: Strength and Young's modulus, Journal of Petroleum Science and Engineering, Volume 135, November 2015, Pages 702-722, ISSN 0920-4105, http://dx.doi.org/10.1016/j.petrol.2015.10.028.

commonly used frac fluids contain proppants, e.g., quartz sand, ceramic or bauxite, depending on the expected fracture closure stress.

For shale gas plays, several criteria for prospective 'sweet spots' have been developed in the past, based on geochemistry (e.g., total organic carbon content and thermal maturity), petrology (porosity, permeability), mineralogy (mineral content and clay composition), and geomechanics (in-situ stress state, natural fracture network and rock brittleness), among others (e.g., Rickman et al., 2008; Sondergeld et al., 2010; Berard et al., 2012; Glorioso and Rattia, 2012; Bjorlykke, 2010; Speight, 2013). Rock mechanical properties (strength, elastic moduli) are important parameters for the assessment of borehole stability and evaluation of stable mud weight windows for drilling (e.g., Fjaer et al., 2008; Gholami et al., 2014; Meier et al., 2013, 2015) and hydrofracturing (e.g., Warpinski et al., 2008; Britt and Schoeffler, 2009; Economides and Nolte, 2000; Soliman et al., 2012). Successful stimulation campaigns to produce fracture networks and enhance production rates depend on shale mechanical properties. In addition, knowledge of the mechanics of shales is crucial to constrain the caprock behavior during Steam Assisted Gravity Drainage (SAGD) operations for enhanced recovery of heavy oil reservoirs (e.g., Rahmati et al., 2014, 2015).

In the past, the geomechanical behavior of various individual shales and clays were examined in numerous experimental studies showing that the strength, static elastic moduli and ultrasonic velocities of these materials depend on the applied pressure (e.g., Islam and Skalle, 2013; Kuila et al., 2011; Naumann et al., 2007; Niandou et al., 1997; Petley, 1999), temperature (e.g., Johnston, 1987; Masri et al., 2014) and strain rate (e.g., Chong and Boresi, 1990; Ibanez and Kronenberg, 1993; Kwon and Kronenberg, 1994; Swan et al., 1989). Commonly, shales show a pronounced anisotropy due to bedding (Speight, 2013). Some studies also investigated the creep behavior of shales (e.g., Cogan, 1976; Gasc-Barbier et al., 2004; Chang and Zoback, 2009; Sone and Zoback, 2013a, 2014). In addition, empirical relations between different mechanical properties were suggested to allow correlations to well logging results (e.g., Chang et al., 2006, Horsrud, 2001). Recently, so-called brittleness index terms were formulated to assess the prospectivity of gas shale plays. These index terms are often based on dynamic elastic parameters (e.g., Grieser and Bray, 2007; Rieckman et al., 2008) or composition (e.g., Jarvie et al., 2007; Wang and Gale, 2009).

Here, we present deformation experiments on various, particularly European, black shales with different composition, maturity and porosity, performed at varying (confining) pressures, temperatures and deformation rates. We determined compressive and tensile strength and the static Young's moduli of these rocks in order to constrain their dependence on the external test conditions and on their volumetric mineral content and porosity. The relation of these parameters to the concept of brittleness will be discussed in a companion paper that may help to improve the efficiency of stimulations.

2.1.2 Sample Materials

The investigated rocks were collected from various European black shale locations within the framework of the European gas shale research projects GASH and GeoEn (Littke et al., 2011; Horsfield et al., 2010). These include samples from Mesozoic (Lower Jurassic) Posidonia shale and from Paleozoic (Cambrian) Alum shale. We examined 4 different types of Posidonia shale: (1) Dotternhausen (DOT), an immature oil shale, freshly blasted in a quarry in SW Germany, (2) Wickensen (WIC, immature), (3) Harderode (HAR, peak oil maturity), and (4) Haddessen (HAD, overmature gas shale). The last 3 types were taken from old cores of the corresponding research wells (depth ≈ 30–50 m) drilled in the Hils Syncline in NW Germany (e.g., Gasparik et al., 2014). The highly overmature Alum (ALM) shale was obtained from fresh cores of the Skelbro-2 well (depth ≈ 17 m) in Bornholm, Denmark (e.g., Ghanizadeh et al., 2014a). In addition, we inspected some mature Paleozoic (Carboniferous) Barnett (BAR) gas shales from Texas, USA (e.g., Jarvie et al., 2007), obtained from cores (depth ≈ 1150 m) of the Mesquite-1 well.

Table 2.1 Petrophysical parameters of investigated samples.

Sample	d µm	VRr %	Φ vol%	TOC vol%	Cly vol%	Cb vol%	Qtz vol%	Py vol%	Fsp vol%	Px vol%	ClyTOC* vol%	Cb* vol%	QFP* vol%	uniaxial triaxial
ALM1	<5	3.6	1.3	16.5	51.0	0.7	24.6	3.7	2.1	0	68.4	0.7	30.9	u, t
ALMxx	<5	0.5-3.7	1.0-4.1	2.0-20.7	44.7-61.6	0.0-1.9	19.1-29.6	3.5-7.4	0.0-8.7	0				u
BAR1	<5	1.1	0.6	13.8	52.1	5.2	21.5	0.7	6.2	0	66.3	5.2	28.5	u, t
BARxx	<5	0.7-1.1	0.5-1.2	5.1-13.9	31.2-52.4	5.2-21.4	21.5-46.3	0.0-1.8	3.7-10.4	0				u
DOT1	<5	0.6	11	14.9	18.0	41.6	12.7	1.8	0	0	37.0	46.8	16.3	u, t
WIC1	<5	0.6	6.5	17.0	25.6	33.9	13.2	2.2	1.6	0	45.6	36.3	18.1	u, t
WIC2	<5	0.6	8	18.3	28.5	29.7	12.8	1.7	1.0	0	50.8	32.3	16.9	t
WICxx	<5	0.6	6.5-8.0	17.0-22.4	17.4-36.7	26.9-50.1	6.9-14.4	2.2-4.0	1.0-1.7	0				u
HAR1	<5	0.9	0.7	10.5	28.4	39.6	16.3	2.4	2.1	0	39.2	39.9	20.9	u, t
HARxx	<5	0.9	0.7-1.3	10.5-13.3	28.4-32.6	32.6-39.9	16.3-19.6	0.0-2.5	0.0-2.1	0				u
HAD1	<5	1.3	8.3	10.8	32.6	27.5	13.8	2.5	4.5	0	47.3	30.0	22.7	t
HAD2	<5	1.3	2.8	11.3	35.0	29.6	14.7	2.2	4.4	0	47.6	30.5	21.9	u
HADxx	<5	1.2-1.3	2.8-8.3	10.8-12.9	27.9-35.5	27.5-49.2	9.3-15.0	1.7-2.7	0.0-6.9	0				u
NOV	10^{a}		<1	0	0	0.0	100	0	0	0	0	0	100	t
FST	$200^{b,c}$		9.2	0	9.4	3.9	64.4	0	13.1	0	10.4	4.3	85.3	t
BST	360^{d}		23.9	0	1.6	0	73	0	1.5	0	2.1	0	97.9	t
LIM	6^{a}		<1	0	0	100	0	0	0.0	0	0	100	0	t
MAR	220^{a}		<1	0	0	100	0	0	0.0	0	0	100	0	t
COA			<1	100	0	0	0	0	0.0	0	100	0	0	t
GRA	750^{e}		<1	0	5.3	0	27.8	0	66.9	0	5.3	0	0	t
GAB	110^{f}		<1	0	0	0	0	5.8	67.5	26.6	0	0	94.7	t

Sample abbreviations with the extension 1 or 2 denote specimens of specific composition used for uniaxial (u) and triaxial (t) testing, whereas those with xx denote specimens with varying composition used for uniaxial testing at ambient conditions. ClyTOC* (= clay + TOC), Cb* (= Cb) and QFP* (= Qtz + Fsp + Py) are vol% of weak, intermediate and strong phases, normalized to 0% porosity. For abbreviations, see nomenclature. References: a) Rybacki et al. (2014), b) Reinicke et al. (2010), c) Backers et al. (2004), d) Dresen et al. (2010), e) Goebel et al. (2012), f) Zhou et al. (2012).

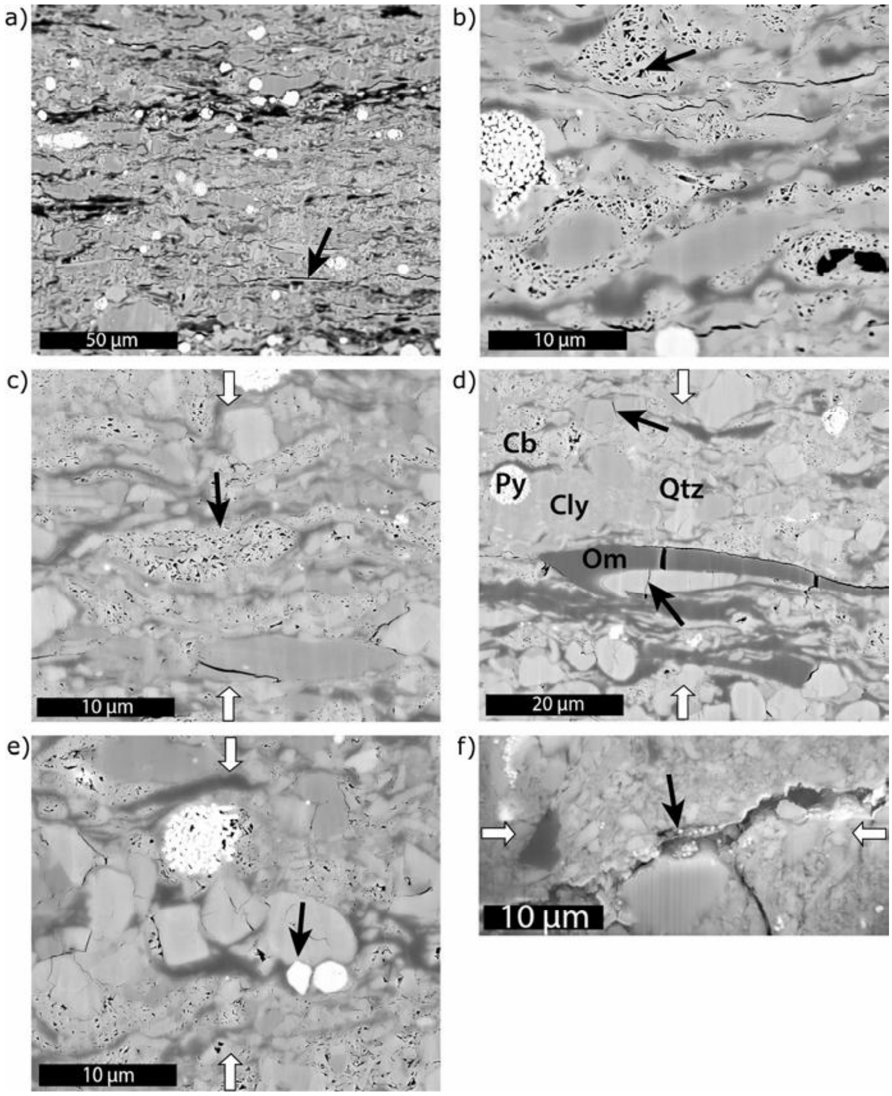

Figure 2.1 SEM images of undeformed (a and b) and deformed Dotternhausen (c–e) and Haddessen (f) samples. Loading direction is indicated by white arrows. Samples were deformed at a strain rate of $5 \cdot 10^{-4}$ s^{-1} at $P = 300$ MPa, $T = 20$°C for Dotternhausen (DOT) and $P = 50$ MPa, $T = 100$°C for the Haddessen (HAD) specimens. Section surfaces were polished using the broad ion beam (BIB) for DOT and the focused ion beam (FIB) technique for HAD samples, respectively. Bedding orientation is horizontal in (a–e) and vertical in (f). Organic matter (Om) appears dark gray, clay (Cly) and carbonate (Cb) minerals are medium gray, quartz (Qtz) is light gray, and pyrite (Py) almost white. Black arrows indicate unloading cracks (a) and intercrystalline pores (b) in undeformed samples and crystal aggregate bending (c), microcracking (d) and indentation (e) in deformed samples. Macrocracks often evolve along grain boundaries (black arrow in f).

All samples were very-fine grained (few µm size) shales with a pronounced fabric anisotropy, defined by bedding of organic matter (Figure 2.1a), calcareous bands and subparallel oriented framboidal pyrite flakes. The composition, determined by X-ray diffraction analysis (XRD, STOE STADI P diffractometer) is a mixture of various amounts of quartz (Qtz), carbonates (Cb), clay (Cly = illite, illite–smectite, kaolinite), pyrite (Py), feldspar (Fsp), organic matter (TOC), and some accessory minerals like chlorite (Table 2.1, Figure 2.1 and Figure 2.2). The porosity, measured by mercury injection porosimetry (MIP, Porotec Fisons 120+2000WS), varies between 0.6% and 11%. Note that this method does not capture micropores (< 2 nm), which may be abundant in highly mature shales and partially stay within the organic compounds (Bernard et al., 2013; Bernard and Horsfield, 2014). Measurements of the total connected porosity using He-pycnometry showed a 1–2 vol% higher porosity for Posidonia and up to 8 vol% higher porosity for overmature Alum shale compared to MIP measurements. Undeformed samples show evidence of unloading microcracks (black arrow in Figure 2.1a) and pores in between the calcite skeletons (black arrow in Figure 2.1b). It should be mentioned here that microstructural observations of shales on polished sections requires careful ion beam instead of mechanical polishing in order to preserve the pore space details. Shale maturity, characterized by vitrinite reflectance, varies between 0.6 and 3.6 VRr% (Table 2.1), which agrees with estimates from geochemical pyrolysis (Rock-Eval, T_{max}) data (Ghanizadeh et al., 2014a, 2014b and references therein).

For reference, we deformed also few samples composed of the main constituents of shales. These were (1) quarzitic rocks (Arkansas novaculite = NOV, Flechtingen sandstone = FST, Bentheim sandstone = BST), (2) carbonate rocks (Solnhofen limestone = LIM, Carrara marble = MAR), and (3) bituminous coal (COA, kindly provided by B. Krooss, Univ. Aachen, Germany). In addition, we deformed Westerly granite (GRA) and Panzhihua gabbro (GAB). Porosity Φ, grain size d and composition of all samples are listed in Table 2.1. Note that we present here the amount of components in vol% instead of wt%, since only the volumetric fraction is of interest for the mechanical behavior. Composition data are converted from wt% to vol% assuming densities of 1.3 g/cm^3 for TOC, 2.65 g/cm^3 for Qtz, 2.71 g/cm^3 for Cb, 5.01 g/cm^3 for Py, 3.3 g/cm^3 for Px, 2.6 g/cm^3 for Fsp, and 2.5 g/cm^3 for Cly, respectively. The differences between vol% and wt% affect mainly the TOC and pyrite content, which can deviate up to a factor of 2.

Unless specified, all samples were deformed under as-is moisture conditions. The water content was ≈ 1–2 wt% for Posidonia and Barnett shale and ≈ 4 wt% for fresh Alum shale, determined by drying of samples until zero weight loss.

For triaxial deformation experiments at elevated temperature, plan-parallel cylindrical samples were drilled and grinded to a length of 20 mm and diameter of 10 mm. Large samples of 50 mm length and 25 mm diameter were prepared for uniaxial tests to measure the uniaxial compressive strength σ_c at ambient temperature in a stiff deformation apparatus. To determine the tensile strength σ_t, we performed Brazilian disc tests on selected samples of 30 mm diameter and length > 15 mm. The axis of sample cylinders (loading direction) were oriented either normal or parallel to bedding.

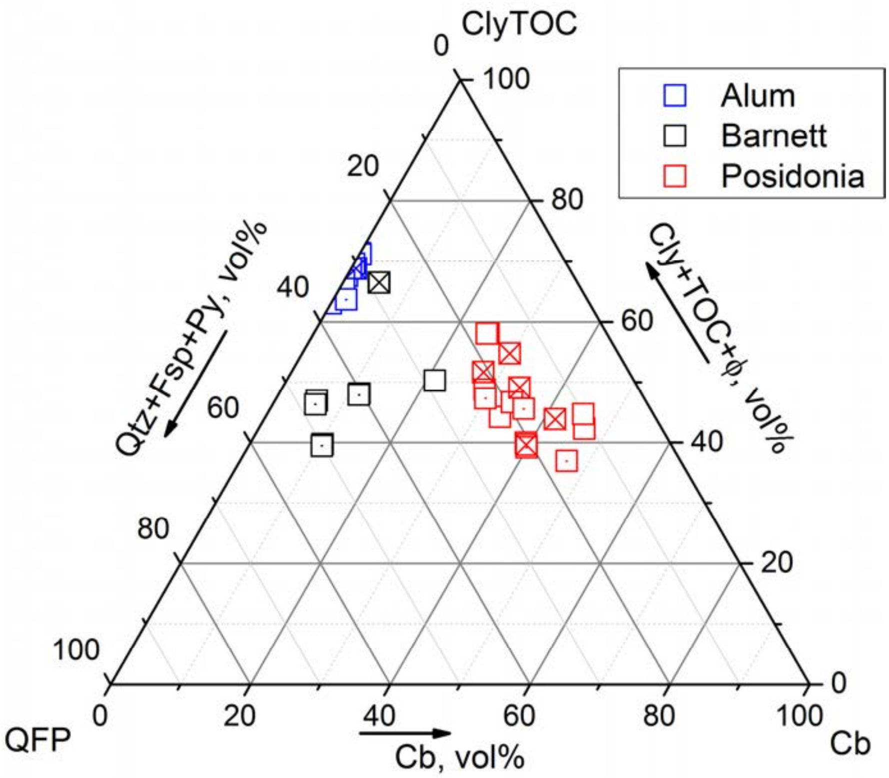

Figure 2.2 Composition of investigated shales, separated into fractions that are mechanically strong (Qtz, Fsp, Py), medium strong (Cb) and weak (Cly, TOC). Open and crossed symbols represent samples used for deformation measurements at ambient and elevated temperature, respectively. Qtz = quartz, Fsp = feldspar, Py = pyrite, Cb = carbonate, Cly = clay, TOC = total organic content. Note that the composition is normalized to vol%, taking into account the porosity Φ.

2.1.3 Experimental Methods

Triaxial deformation experiments were mainly performed in a Paterson-type high temperature, high pressure deformation apparatus (Paterson, 1970) at constant strain (deformation) rate. The confining pressure medium was argon gas, which allowed precise stress measurements using an internal load cell within the pressure vessel. To prevent intrusion of the pressure medium, samples were jacketed by thin (≈ 0.5 mm) copper sleeves. Measured forces and axial displacements were converted to axial stress and strain, assuming constant volume deformation and corrected for the jacket load and system compliance. The estimated error in stress and strain is < 4%. The estimated uncertainties of determined Young's moduli E are about 20%, due to the low intrinsic stiffness of the apparatus. Since almost all deformed shales showed continuous non-linear hardening with increasing strain and no well-defined yield point, which did not allow unambiguous determination of Young's modulus, we used the secant modulus, determined from the slope of stress–strain curves from the origin to the strain measured at 50% of the peak stress. Using instead the tangent modulus measured at ≈ 50% of the peak stress typically resulted in 20–30% lower Young's moduli, which is of similar uncertainty magnitude associated with the high system compliance.

Uniaxial compression experiments and Brazilian disc tests were done in a stiff and fast-reacting servo-hydraulically controlled deformation apparatus (MTS). The tests were performed at constant deformation rates of 0.2 mm/min, corresponding to an axial strain rate of $\approx 7 \times 10^{-5}$ s^{-1}. Recorded axial displacements were corrected for the system stiffness. The tensile strength was determined following the ISRM suggested method for Brazilian disc testing (Bieniawski and Hawkes, 1978). In addition, some triaxial deformation tests at room temperature and confining pressures between 17.5 and 70 MPa were performed on shales in the MTS machine to determine the internal friction coefficient.

2.1.4 Results

Here, we present only mechanical results of those samples, for which mineral composition, porosity and maturity were also determined. In total, we performed 87 triaxial compression tests, 34 uniaxial compression tests and 60 Brazilian disc tests. We first present results obtained at ambient conditions and then the data measured at elevated temperatures and pressures.

2.1.4.1 Mechanical Behavior at Ambient Conditions

Uniaxial compression and Brazilian disc tests at ambient pressure and temperature were performed on shale samples prepared parallel and perpendicular to bedding. For multiple tests on samples from the same depth, the mean values and associated error bars are shown in Figure 2.3.

The measured stress–strain curves during uniaxial compression typically show limited inelastic deformation until abrupt failure at stresses up to about 100 MPa (Figure 2.3a). Samples loaded normal to bedding exhibit lower Young's moduli compared to those deformed parallel to bedding. Posidonia samples often failed by axial splitting, Barnett samples developed a single shear crack and Alum samples showed multiple conjugate shear fractures. Irrespective of different failure modes, the three shales deformed brittle, showing low inelastic strain and hardening and sudden failure. The observed differences are likely attributed to different loading configurations (parallel or normal to bedding), composition, porosity and water content of the samples.

The uniaxial (unconfined) compressive strength (UCS) and the (unconfined) tensile strength depend on the loading direction with respect to bedding orientation, showing that the strength of shales is strongly orthotropic. UCS values are between 21 and 122 MPa, with higher strengths normal to bedding, whereas Young's modulus varies between 4 and 29 GPa, typically lower for bedding-normal compression (Table 2.2, Figure 2.3b). The unconfined compressive strength clearly increases with increasing Young's modulus for the different shale types, but is lower for most fresh Alum samples compared to as-is Posidonia and Barnett specimens (Figure 2.3b). The tensile strength of all tested samples varies between ≈3 and ≈19 MPa, with lower values if the samples were loaded parallel to bedding (Table 2.2, Figure 2.3c). In particular for Alum shale UCS also increases with increasing tensile strength (Figure 2.3c). Note that the correlations between σ_c and σ_t shown in Figure 2.3c contain only those data, which were measured on samples with similar composition, whereas Table 2.2 contains also the range of data measured on different sections. Interestingly, P-wave velocities of Alum shale, measured on-site via sonic-logging in the shallow well in Bornholm, clearly correlate with σ_c (Figure 2.3d) and E (not shown here), measured at ambient conditions in the laboratory. This suggests also a good correlation between quasi-static and dynamic Young's modulus since the latter is directly related to the longitudinal velocity.

Table 2.2 Mechanical data at ambient conditions (P = 0.1 MPa, T = 20 °C).

Sample	σ_{c_n} MPa	σ_{c_p} MPa	E_n GPa	E_p GPa	σ_{t_n} MPa	σ_{t_p} MPa
ALM1		41.2		11	-	6.9
ALMxx		21.3 - 94.5		8 - 29		4.7 - 10.1
BAR1		35.8		12	17.1	4.2
BARxx		35.8 - 105.7		12 - 25	5.3 - 18.7	4.1 - 4.2
DOT1	80.3	71.0	5	9.4	8.7	2.7
DOTxx	78.4 - 81.0	64.8 - 78.4	5	9 - 10	7.9 - 9.3	1.4 - 3.3
WIC1	87.7	78.8	4	11	10.0	10.8
WICxx	84.0 - 91.4	78.8	4	11	8.3 - 11.6	7.1 - 11.4
HAR1	115	82	10	15	7.0	9.1
HARxx	110 - 122	68 - 85	10 - 11	15 - 20	5.0 - 9.0	8.0 - 10.0
HAD2	85.5	106	8	15	9.1	4.2
HADxx	76 - 95	48 - 106	8	8 - 15	4.9 - 10.2	3.8 - 4.8
NOV	451	451	83[c]	83[c]	18.2	18.2
FST	96[a]	96[a]	21[a]	21[a]	6[a]	6[a]
BST	44	44	25[b]	25[b]	2	2
LIM	208	208	62[d]	62[d]	9.9	9.9
MAR	101[a]	101[a]	49[a]	49[a]	7[a]	7[a]
COA	26	26	3.4[e]	3.4[e]	2.5	2.5
GRA	230[c]	230[c]	70	70	12[c]	12[c]

σ_c, σ_t , E = unconfined compressive strength, tensile strength and Young's modulus, respectively. Strain rate in compression tests is 7x10^{-5} s^{-1}. Subscripts: *n* = normal, *p* = parallel to bedding. For abbreviations, see nomenclature. References: a) = Backers et al. (2004), b) = Dresen et al. (2010), c) = Rummel (1982), d) = Gebrande (1982), e) = Seidle (2011).

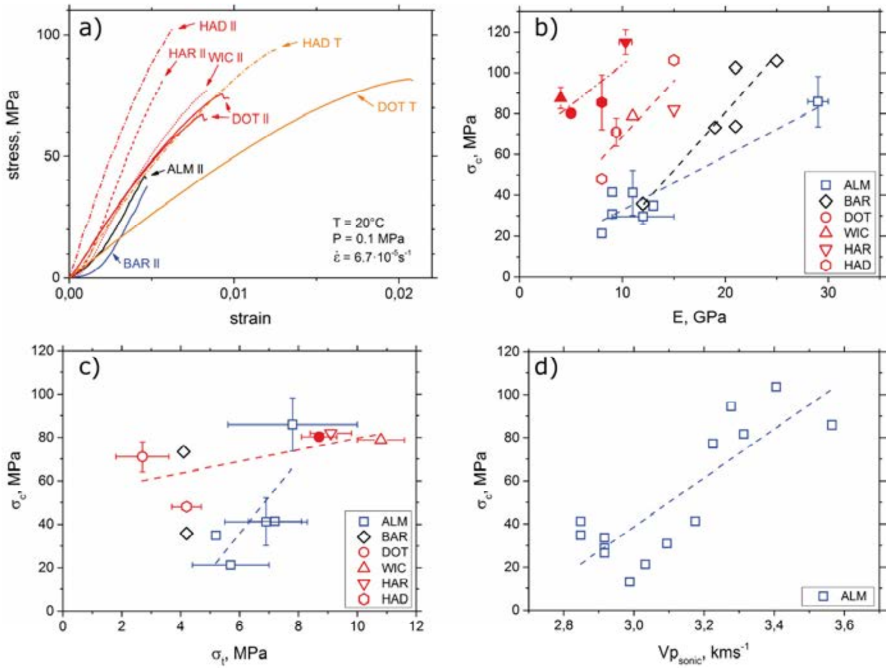

Figure 2.3 Representative stress–strain curves of black shales obtained at ambient temperature and pressure (a) and empirical cross-correlations between unconfined compressive strength σ_c and Young's modulus E (b), σ_c and unconfined tensile strength σ_t (c), and between σ_c and sonic–log velocity Vp_{sonic} (d). Open and filled symbols represent measurements parallel (ll) and normal (T) to bedding, respectively. ALM = Alum, BAR = Barnett, DOT = Dotternhausen, WIC = Wickensen, HAR = Harderode, and HAD = Haddessen shale.

2.1.4.2 Triaxial Deformation Behavior

We performed 54 triaxial compression tests on small samples in the Paterson apparatus at confining pressures of 50–400 MPa, temperatures between 20°C and 400°C, and axial strain rates of 5 x 10^{-3} – 5 x 10^{-7} s^{-1}. These tests were done on selected samples of the different shales with varying maturity, porosity, and composition (Table 2.1). In addition, 33 tests were performed at room temperature, axial strain rate of ≈7 x 10^{-5} s^{-1} and confining pressures up to 75 MPa using the MTS apparatus. In the following, we briefly describe the results with respect to sample composition and deformation conditions. Almost all tests were performed on cylindrical samples with loading direction normal to bedding.

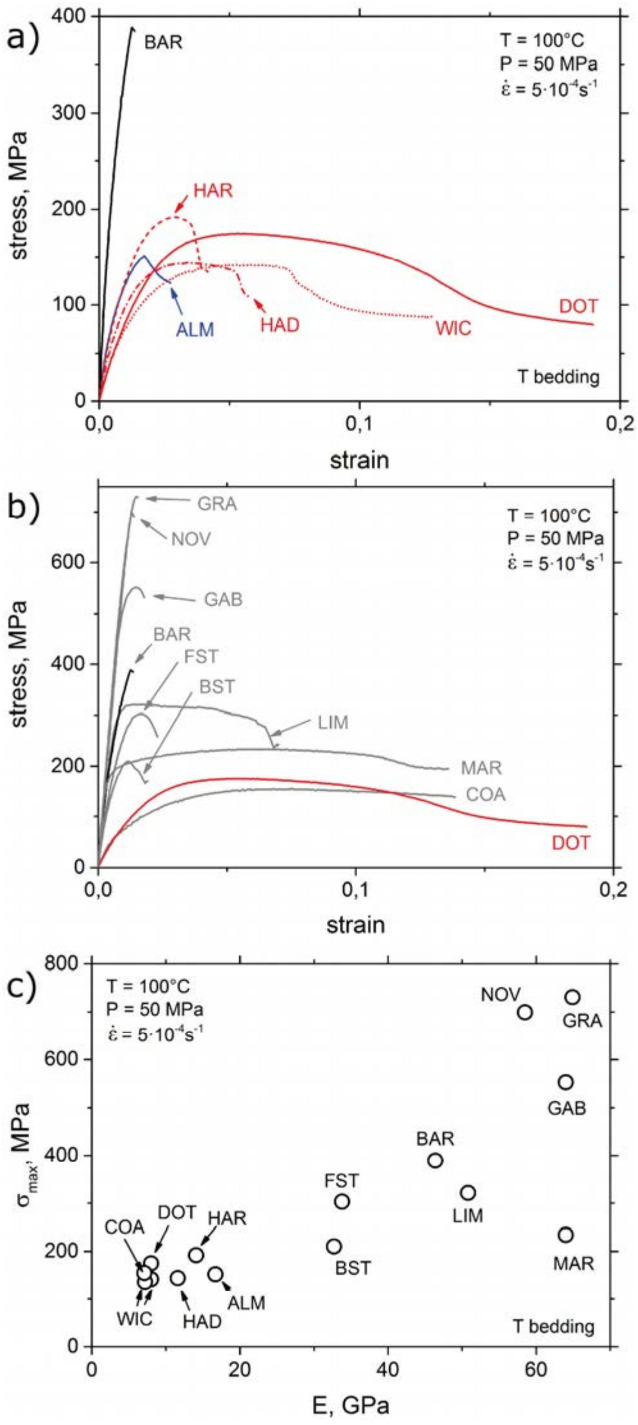

Figure 2.4 Stress–strain curves of shales (a) and reference rocks (b) (including curves of BAR and DOT for comparison) deformed under triaxial conditions. (c) Relation between peak strength σ_{max} and Young's modulus E. Deformation conditions are indicated. ALM = Alum, BAR = Barnett, DOT = Dotternhausen, WIC = Wickensen, HAR = Harderode, HAD = Haddessen shale, GRA = Westerly granite, NOV = Arkansas novaculite, GAB = Panzhihua gabbro, FST = Flechtingen sandstone, BST = Bentheim sandstone, LIM = Solnhofen limestone, CAR = Carrara marble, and COA = bituminous coal.

2.1.4.2.1 Influence of Porosity and Composition

We deformed one sample of each shale type normal to bedding at a relatively fast strain rate of 5×10^{-4} s^{-1}, confinement of 50 MPa, and temperature of 100°C, representing in-situ conditions of 2–4 km depth with a high geothermal gradient. The corresponding stress–strain curves (Figure 2.4a) reveal a considerably increased peak strength and peak strain compared to uniaxial conditions (cf., Figure 2.3a). Posidonia shales with high porosity (DOT, WIC, HAD) show semibrittle deformation with pronounced nonlinear hardening and weakening before and after peak stress (e.g., Evans et al., 1990). In contrast, the clay-rich, but low porosity, Alum and Barnett shales reveal distinct peak stresses, minor initial hardening and localized failure, typical for brittle deformation.

For reference, we also deformed samples composed of the main constituents of shales under similar conditions (Figure 2.4b, Table 2.3). The quartzite (NOV), granite (GRA) and gabbro (GAB), all with < 1% porosity and mainly consisting of strong quartz, feldspar and pyroxene minerals, exhibit very high strength and almost linear elastic behavior until failure. Compared to these rocks and Barnett (BAR) shale with 0.6% porosity, the strength of porous sandstones (FST, $\Phi \approx 9\%$; BST, $\Phi \approx 24\%$) is considerably lower. In contrast, the coal (COA) sample, assumed to be representative for weak kerogen and clay in this context, reveal almost steady state creep deformation up to high strain with at a stress level slightly below that of the Dotternhausen (DOT) Posidonia shale. The strength of the two low-porosity (< 1%) limestone (LIM) and marble (MAR) samples is comparable to that of sandstone, but both deformed to high strains at almost constant stress. Coarse-grained marble is weaker than fine-grained limestone, revealing the influence of grain size and/or cementation. Except for marble, the peak strength of all samples increases with increasing static Young's modulus (Figure 2.4c, Table 2.3). Here, we assume that the mechanical properties of the reference samples are isotropic, although some are laminated, in particular coal.

Deformed coal, Dotternhausen and Wickensen shale, marble and to some extend limestone samples deformed semibrittle to barrel-shaped specimens with abundant microcracks, whereas the remaining samples showed localized failure along single crosscutting shear fractures.

Table 2.3 Mechanical data at elevated *P–T* conditions.

T, °C	20		20		100		100		200		200	
P, MPa	50		100		50		100		50		100	
	σ_{max_n} MPa	$E_{\_n}$ GPa	σ_{max_n} MPa	$E_{\_n}$ GPa	σ_{max_n} MPa	$E_{\_n}$ GPa	σ_{max_n} MPa	$E_{\_n}$ GPa	σ_{max_n} MPa	$E_{\_n}$ GPa	σ_{max_n} MPa	$E_{\_n}$ GPa
Sample												
ALM1					152	16.7						
BAR1					389	46.4						
DOT1	177	9.8	199	8.7	175	8	201	8.4	141	6.2	153	6.2
WIC1	174	9.2	258	9.6	142	8	162	6.9	105	4.5	138	4.9
WIC2					136	7.2						
HAR1	236	19.3	265	11.6	192	14.1	201	12.5	155	11.4	171	12.6
HAD1	181	13.0	205	11.0	144	11.6						
NOV					699	58.8						
FST					303	33.8						
BST					210	32.7						
LIM					321	50.8						
MAR					234	64						
COA					155	7.1						
GRA					731	64.9						

σ_{max_n}, $E_{\_n}$ = peak strength and Young's modulus measured normal to bedding, respectively. Strain rate in compression tests is $5x10^{-4}$ s^{-1}. For abbreviations, see nomenclature.

2.1.4.2.2 Effect of Confining Pressure

With increasing isostatic pressure, DOT samples compact and the bulk modulus, obtained by volumetric strain measurements at ambient temperature and stepwise increased isostatic pressure, increases by about 34% approaching a value of ≈ 7 GPa at P ≈ 200 MPa (Figure 2.5a). This behavior indicates porosity reduction and closure of unloading cracks with increasing pressure.

The triaxial deformation of Posidonia (DOT) shale is also strongly pressure dependent in the range of 50–400 MPa (Figure 2.5b, Table 2.4). With increasing confining pressure, stress strain curves change from post-peak strain weakening at low pressure towards almost steady state deformation at the highest pressures. Below 150 MPa confining pressure, deformed samples show localized shear failure, but at higher pressure the samples were barrel-shaped without distinct shear bands. The peak differential stress σ_{max} first increases nonlinearly with increasing pressure up to about $P \approx 100$ MPa and shows an almost linear increase towards higher pressures (stippled line in Figure 2.5c). A similar nonlinear increase at low pressure appears for the other Posidonia shales. In the linear regime, σ_{max} changes by about 0.57 MPa per 1 MPa increase of confining pressure at T = 20°C. Assuming an overburden-related pressure gradient of 26 MPa/km, this translates into a strength increase of ≈ 15 MPa/km. At higher T of 100–200°C, the strength increase is about 8 MPa/km (Table 2.3).

For high-porosity Posidonia shale (DOT, WIC), Young's modulus increases up to about 150 MPa pressure and remains almost constant within error bars for higher pressures (Figure 2.5d). For Posidonia samples with low and varying porosity, there is no clear trend (HAR, HAD in Figure 2.5d). There is a positive relation between E and σ_{max} for individual shale rocks only at low pressures when deformation is dominantly brittle (Figure 2.5e; Table 2.3).

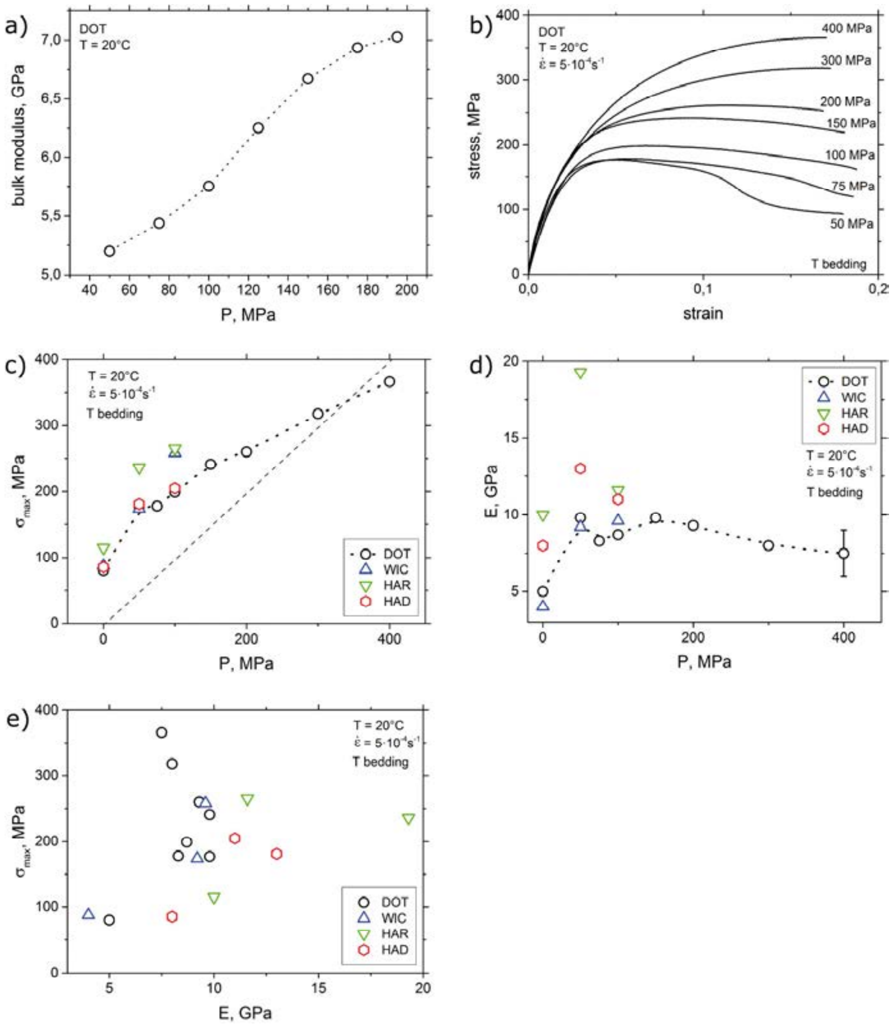

Figure 2.5 Influence of confining pressure on bulk modulus (a), stress–strain behavior (b), peak stress (c), Young's modulus (d) and correlation between peak stress strength and *E* (e). Deformation conditions are indicated. Note that the deformation rate of tests performed at ambient (0.1 MPa) pressure was ≈$7\cdot10^{-5}$ s^{-1}. DOT = Dotternhausen, WIC = Wickensen, HAR = Harderode, and HAD = Haddessen shale.

2.1.4.2.3 Temperature Effects

Several Posidonia samples were deformed at constant strain rate, confining pressures of 50 and 100 MPa and temperatures of 20, 100 and 200°C (Table 2.3). For DOT shale, additional tests were performed at 50, 75, 150, 300 and 400°C (Table 2.4). Typically, peak strength decreases with increasing temperature and increases with increasing pressure (Figure 2.6). For Dotternhausen shale deformed at 50 MPa pressure, the peak stress is roughly constant with increasing temperature but then decreases with temperature above 75–100°C (Figure 2.6a). Independent of temperature, all DOT samples showed a single fracture after failure except the sample tested at 400°C, which showed a broad shear zone and a sudden stress drop, probably associated with partial burning of the kerogen. At similar confining pressure of 50 MPa, the high-porosity Wickensen samples showed a transition from brittle (steep post failure weakening) to more ductile (smooth post-failure weakening) deformation behavior with increasing temperature from

20 to 200°C, associated with a change from discrete fracturing to barreling (Figure 2.6b). In contrast, low-porosity Harderode samples always showed brittle failure with a notable stress drop and formation of a single shear fracture. At 100 MPa pressure, also Harderode samples showed a transition from brittle to semibrittle deformation with increasing temperature (Figure 2.6c). High porosity Wickensen and Dotternhausen (not shown in Figure 2.6c for better readability) samples showed semibrittle deformation at almost constant stress.

All samples show a decrease in strength with an increase of temperature between 20 and 200°C at pressures of 50 and 100 MPa (Figure 2.6d). Also the Young's modulus decreases with T, albeit with a larger scatter (Figure 2.6e). The strength decrease is ≈ 9–11 MPa/km depth, assuming a geothermal gradient of 25°C/km (uncertainty < 30%). This decrease may balance the estimated pressure-induced strength increase of about 8–15 MPa/km at high pressures (> 100 MPa). Peak strength and Young's modulus are strongly correlated (Figure 2.6f), except for Harderode samples. This correlation is rather unaffected by temperature between 20°C and 200°C and appears to be slightly stronger at 100 MPa pressure than at 50 MPa confinement.

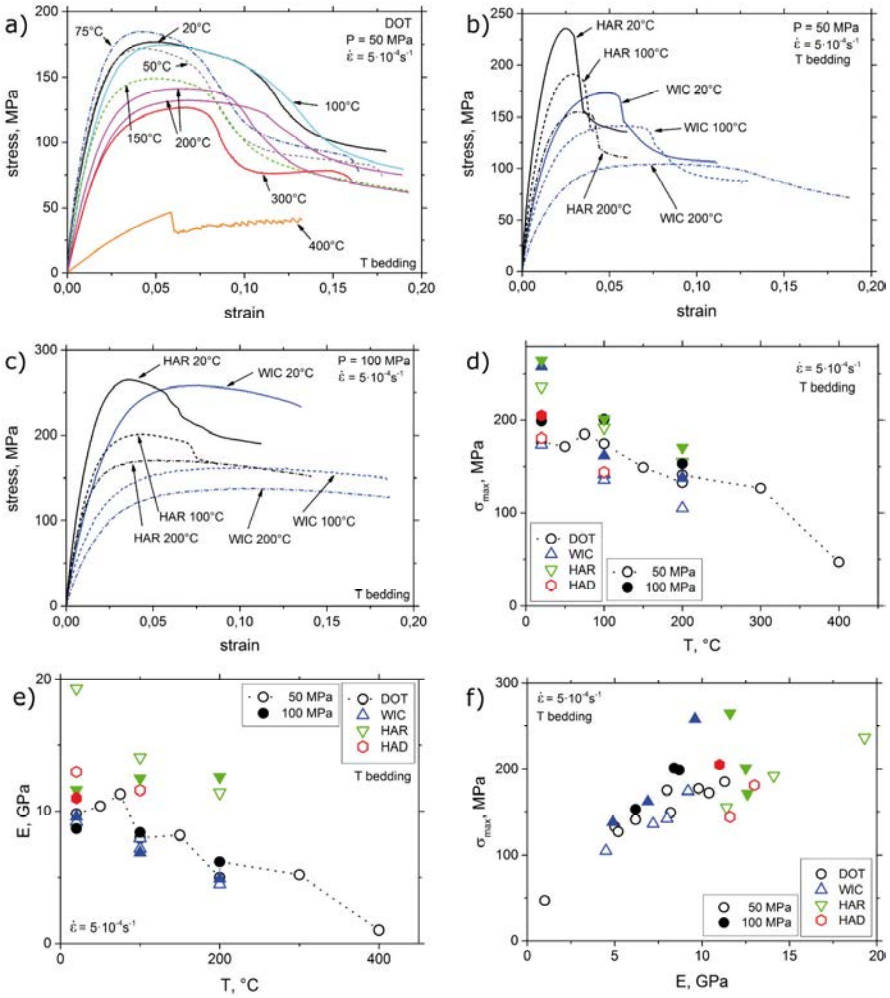

Figure 2.6 Influence of temperature on stress–strain behavior of Dotternhausen shale at P = 50 MPa (a) and Wickensen and Harderode shale at P = 50 MPa (b) and 100 MPa (c). Nearly linear correlations are evident between temperature and σ_{max} (d) as well as Young's modulus (e), and between peak strength and E (f). Open and solid symbols denote 50 MPa and 100 MPa confining pressure, respectively. Deformation conditions are indicated. DOT = Dotternhausen, WIC = Wickensen, HAR = Harderode, and HAD = Haddessen shale.

2.1.4.2.4 Influence of Strain Rate

The effect of strain rate on the mechanical behavior was evaluated for Wickensen and Dotternhausen samples at 50 MPa pressure and 100°C temperature (Table 2.4). With decreasing strain rate in the range of $5\cdot10^{-3}$–$5\cdot10^{-7}$ s^{-1} the strength of both shales decrease and the rate of post-failure weakening increases (Figure 2.7a). In semi-logarithmic scale, peak stress and Young's modulus decreases almost linearly with decreasing strain rate (Figure 2.7b and c). Similar to the behavior at different temperatures, the peak strength increases with increasing Young's modulus (Figure 2.7d).

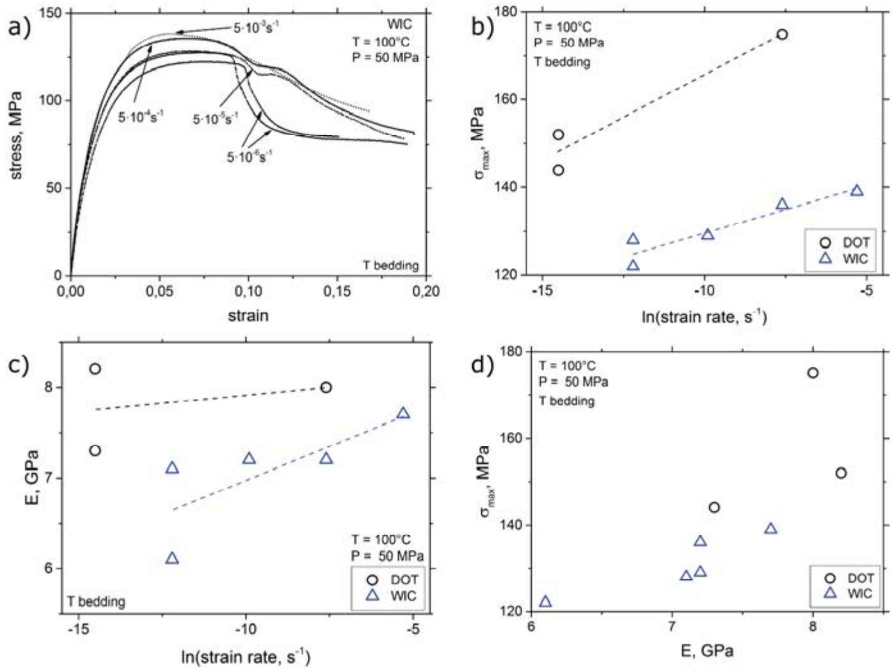

Figure 2.7 Influence of strain rate on stress–strain behavior (a), peak stress (b) and Young's modulus (c), and correlation between peak differential stress (σ_{max}) and E (d) of Wickensen and Dotternhausen samples. Deformation conditions are indicated. DOT = Dotternhausen, and WIC = Wickensen shale.

2.1.4.2.5 Influence of Water Content and Bedding Orientation

The influence of water saturation and bedding orientation on the mechanical behavior was investigated for Alum shale at P = 50 MPa, T = 100°C (Table 2.4). We deformed two fresh samples with as-is water content (3.6 wt% H_2O) parallel and normal to bedding. The peak strain is slightly higher and the post-failure weakening lower for the sample loaded perpendicular to bedding (Figure 2.8a). After drying in an oven for several days (≈ 0.01 wt% H_2O) the strength and Young's modulus increased, whereas the shale was weaker and also E decreased slightly after adding deionized water to almost water-saturated (≈ 3.8 wt% H_2O) conditions (Figure 2.8b and c). Note that the water saturation S_w (= wt% H_2O x ϱ_{rock}/Φ, ϱ_{rock} ≈ 2.45 g/ccm) shown in Figure 2.8 is determined with reference to the measured total connected porosity of 9.3%, measured by He-pycnometry, which is much higher than the porosity determined by mercury injection (≈ 1.3%) for Alum shale. At given orientation, the peak stress again increases with increasing Young's modulus for samples with different water contents (Figure 2.8d). All samples showed localized shear failure, independent of water saturation and orientation.

Table 2.4 Mechanical data at selected deformation conditions.

Sample	T °C	P MPa	$\dot{\varepsilon}$ s^{-1}	c_{H2O} w%	S_w %	σ_{max_n} MPa	E_n GPa	σ_{max_p} MPa	E_p GPa
DOT1	20	0.1	$5x10^{-4}$	as-is		80	5		
	20	50	$5x10^{-4}$	as-is		177	9.8		
	20	75	$5x10^{-4}$	as-is		178	8.3		
	20	100	$5x10^{-4}$	as-is		199	8.7		
	20	150	$5x10^{-4}$	as-is		241	9.8		
	20	200	$5x10^{-4}$	as-is		260	9.3		
	20	300	$5x10^{-4}$	as-is		318	8.0		
	20	400	$5x10^{-4}$	as-is		366	7.5		
DOT1	20	50	$5x10^{-4}$	as-is		177	9.8		
	50	50	$5x10^{-4}$	as-is		172	10.4		
	75	50	$5x10^{-4}$	as-is		185	11.3		
	100	50	$5x10^{-4}$	as-is		175	8.0		
	150	50	$5x10^{-4}$	as-is		149	8.2		
	200	50	$5x10^{-4}$	as-is		141	6.2		
	200	50	$5x10^{-4}$	as-is		133	5.0		
	300	50	$5x10^{-4}$	as-is		127	5.2		
	400	50	$5x10^{-4}$	as-is		47	1.0		
DOT1	100	50	$5x10^{-4}$	as-is		175	8.0		
	100	50	$5x10^{-7}$	as-is		152	7.3		
	100	50	$5x10^{-7}$	as-is		144	8.2		
WIC2	100	50	$5x10^{-3}$	as-is		139	7.7		
	100	50	$5x10^{-4}$	as-is		136	7.2		
	100	50	$5x10^{-5}$	as-is		129	7.2		
	100	50	$5x10^{-6}$	as-is		128	7.1		
	100	50	$5x10^{-6}$	as-is		122	6.1		
ALM1	100	50	$5x10^{-4}$	0.01	0.26			230	34.9
	100	50	$5x10^{-4}$	3.6	93	152	16.7	174	26.2
	100	50	$5x10^{-4}$	3.8	98			132	25.6

σ_{max}, E = peak strength and Young's modulus, respectively. Subscripts: n = normal, p = parallel to bedding. $\dot{\varepsilon}$ = strain rate, c_{H2O} = water content, S_w = water saturation. For abbreviations, see nomenclature.

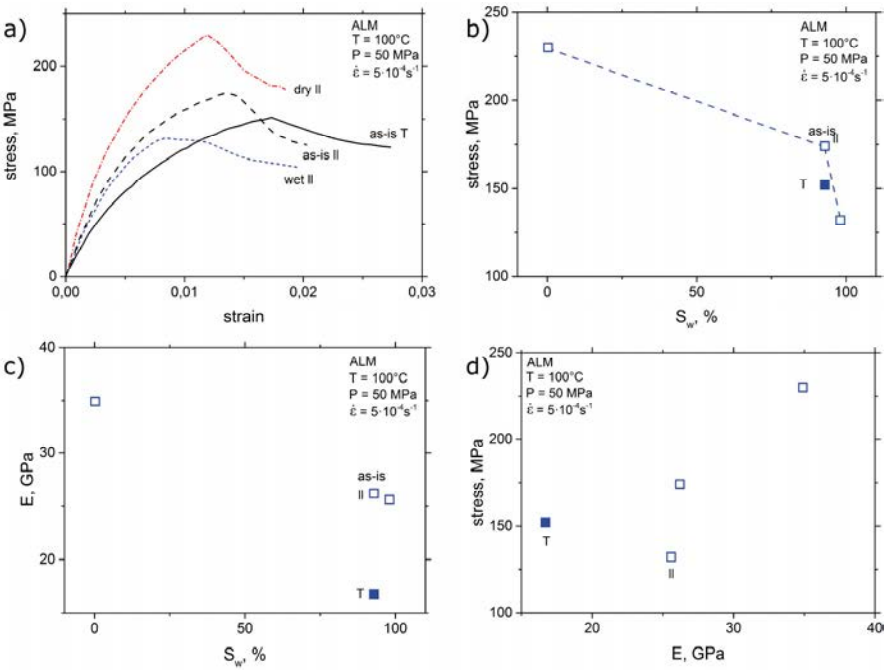

Figure 2.8 Influence of water saturation and bedding orientation on the stress–strain behavior (a), peak stress (b) and Young's modulus (c), and correlation between peak differential stress (σ_{max}) and E (d) of Alum (ALM) shale. Deformation conditions are indicated. Open and filled symbols represent deformation parallel and perpendicular to bedding, respectively.

2.1.4.3 Microstructures

Macroscopically, deformed shale samples showed single or multiple discrete fractures or distributed deformation and barreling, depending on composition and applied loading conditions. Semibrittle deformation is favored by high porosity, elevated temperatures and pressures. Samples showing non-localized deformation revealed a combination of brittle and plastic processes operating at the microscale. For example, the Dotternhausen specimen deformed at 20°C temperature and 300 MPa pressure at almost steady state stress (Figure 2.5a) shows evidence of pore collapse perpendicular to the applied loading direction, combined with a bending of carbonate skeletons (black arrow in Figure 2.1c). In addition, microcracking of strong particles (black arrows in Figure 2.1d) and occasionally indentation of stronger into weaker grains occurred (black arrow in Figure 2.1e).

Samples that deformed macroscopically brittle showed little evidence for pervasive microcracking. Instead, macrofractures often crosscut the sample along grain boundaries (black arrow in Figure 2.1f) and only minor intragranular deformation is visible. The Posidonia (HAD) sample shown in Figure 2.1f revealed macrofracturing and a sudden stress drop after constant strain rate deformation at P = 50 MPa and T = 100°C (Figure 2.4a).

2.1.5 Discussion

The mechanical behavior of shales at pressures between 0.1 and 100 MPa and temperatures of 20–400°C can be classified as brittle to semibrittle. The strength depends strongly on pressure (Figure 2.5), typical for brittle deformation, but also on temperature (Figure 2.6) and applied strain rate (Figure 2.7), which are both typical for plastic deformation processes. This is supported by microstructural observations that reveal microfracturing of strong particles, pore collapse, flow of organic materials (kerogene, bitumen) and relative movement of grains (granular flow). Also, water content and loading direction with respect to bedding orientation affect the strength and elastic properties (Figure 2.3 and Figure 2.8). A transition from brittle fracture to semibrittle flow with applied deformation conditions was also observed by Ibanez and Kronenberg (1993) in triaxial deformation experiments on clay-rich Wilcox shale at pressures up to 400 MPa, temperatures ≤ 200°C and strain rates between 2×10^{-7} s^{-1} and 2×10^{-4} s^{-1}.

The transition of brittle to (pressure-insensitive) plastic deformation is predicted by the empirical Goetze criterion (Evans and Kohlstedt, 1995) once the differential flow stress is lower than the applied confining pressure. For DOT samples this transition is predicted for 400 MPa pressure (i.e., the strength is below the broken line in Figure 2.5c). However, sample strength still increases with pressure considerably from 300 to 400 MPa. This suggests that at 20°C temperature significantly higher confining pressures than predicted by the Goetze criterion are required to obtain fully plastic deformation.

Interestingly, we did not observe a transition from brittle to ductile behavior at low strain rates (Figure 2.7) and the samples commonly developed a localized shear fracture rather than distributed deformation and barreling. This suggests that a low strain rate favors the coalescence of microcracks, probably associated with a transition from undrained to drained conditions. In the following, we discuss the observed changes of mechanical strength and elastic modulus with loading conditions and sample composition.

2.1.5.1 Effect of Pressure

The pressure-dependence of the shale strength can be described by a linear Mohr–Coulomb criterion only at elevated pressure, higher than ≈ 50–100 MPa. An example is given in Figure 2.9a for DOT samples deformed at 20°C, showing increasing axial peak stress σ_1 (= $\Delta\sigma + P$ with $\Delta\sigma = \sigma_{max}$ = peak (differential) stress) with increasing applied confining pressure P. Extrapolation of the fitted linear slope (broken line in Figure 2.9a) to atmospheric pressure would overestimate the measured uniaxial compressive strength. This deviation likely results from initial closure of pores and microcracks at low pressure, in particular for high-porosity shales. Other common failure criteria like the Drucker–Prager and Hoek–Brown criteria (e.g., Sheorey, 1997) yield similar nonlinear fits over the whole pressure range, whereas nonlinear criteria, for example the Griffith, Fairhurst or Murrell equations, show a better fit to the entire data set. It should be mentioned that the strength and deformation mode of clays and shales also depend on the intermediate principal stress under true triaxial stress states (Takahashi and Kiode, 1989; Hunsche et al., 2004; Popp and Salzer, 2007; Naumann et al., 2007). The linear Mohr–Coulomb failure criterion is given by

$$\tau = \tau_0 + \mu\sigma_n \text{ or } \sigma_1 = \sigma_c + mP \qquad 2.1$$

with τ = shear stress, σ_n = normal stress and τ_0 = cohesion. The coefficient of internal friction, μ, can be obtained from the slope m of the fitting line in σ_1–P coordinates using $\mu = (\mathrm{m} - 1)/(2\sqrt{m})$, e.g., Zoback (2007). For Dotternhausen shale, the fitted coefficient of internal friction is about 0.18, which is low compared to typical values (≈ 0.6–0.9) for hard rocks. The other Posidonia shales exhibit comparable internal friction coefficients in the range of 0.16– 0.31 at T = 20°C and P = 50–100 MPa. They appear to slightly decrease with increasing temperature from 20°C to 200°C, but the variation is mostly <0.1. It should be noted, however, that most of the μ data rely on just 2 or 3 measurements per rock type. Interestingly, the internal friction coefficient of Alum shale is higher (0.36–0.55) and that of Barnett shale is even 1.08, measured parallel to bedding. High internal friction coefficients of about 0.7–0.9 for Barnett shale were also measured by Sone and Zoback (2013a) at T = 20°C and P < 70 MPa. These authors also found a slight decrease of μ for an increase of clay + TOC content by about 40 vol%. For comparison, the internal friction coefficients of Eagle Ford and Haynesville shales are μ ≈ 0.3–0.5 at P < 70 MPa (Sone and Zoback, 2013a), μ ≈ 0.3–0.5 for Wilcox shale at P < 200 MPa, depending on bedding orientation (Ibanez and Kronenberg, 1993), and μ ≈ 0.25 for Opalinus clay at P < 400 MPa (Jordan and Nüesch, 1989). We found no clear correlation between μ and maturity, porosity or the amount of carbonates and weak (clay + TOC) components, but μ appears to increase with the fraction of strong (QFP) minerals at T = 20°C (Figure 2.9b). This suggests that a high fraction of strong minerals in shales start to develop a load-bearing framework, leading to high strength and strong pressure dependence.

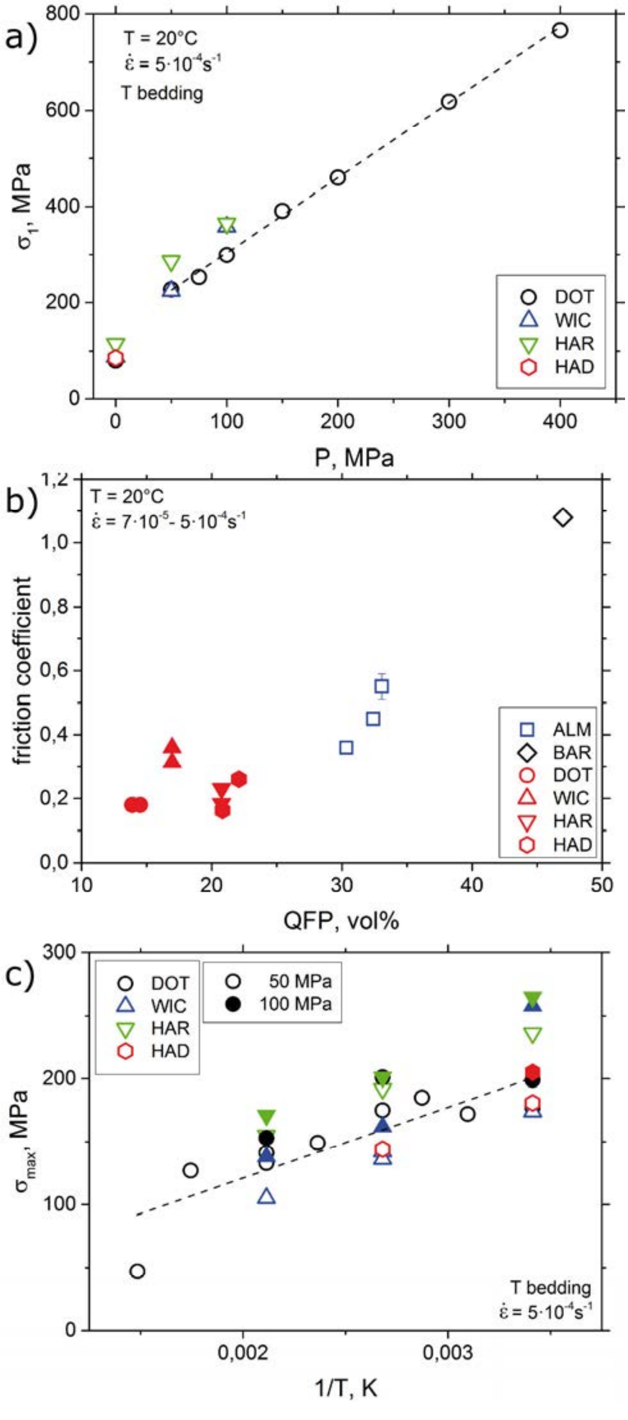

Figure 2.9 (a) Pressure dependence of axial peak strength σ_1, (b) variation of internal friction coefficient μ with fraction of hard (quartz+feldspar+pyrite) minerals and (c) change of peak differential stress σ_{max} with inverse absolute temperature. Deformation conditions are indicated. Open and filled symbols in (b) represent deformation parallel and perpendicular to bedding, respectively. ALM = Alum, BAR = Barnett, DOT = Dotternhausen, WIC = Wickensen, HAR = Harderode, and HAD = Haddessen shale.

We obtained a positive, shale type-dependent, correlation between uniaxial compressive strength and Young's modulus and P-wave velocity (Figure 2.3), which was also found for other shales (e.g., Horsrud et al., 1998, Chang et al., 2006). This correlation between strength and elastic properties holds for a broad range of temperatures, strain rates and water content (Figure 2.4c,

Figure 2.6f, Figure 2.7d, and Figure 2.8d). However, at elevated confining pressures, strength and elastic modulus do not show a clear correlation (Figure 2.5e) because the Young's modulus remains constant at pressures beyond 50–150 MPa (Figure 2.5d), but the peak strength increases monotonically with increasing *P* (Figure 2.5b). A non-linear increase of Young's modulus with increasing confinement was also found for Wilcox shale (Ibanez and Kronenberg, 1993) and clay-rich, high-porosity Tournemire shale (Niandou et al., 1997; Masri et al., 2014), revealing also different pressure sensitivities for different loading directions with respect to bedding. It should be mentioned that dynamic Young's moduli determined from ultrasonic velocities are usually higher (≈ 20–40%) than quasi-static moduli (e.g., Yale and Jamieson, 1994; Britt and Schoeffler, 2009, Sone and Zoback, 2013b) and that Young's moduli obtained at undrained conditions are higher than those measured under drained conditions (Islam and Skalle, 2013). However, Young's moduli determined from un- or reloading stress–strain curves fit well to dynamic moduli (Sone and Zoback, 2013b).

2.1.5.2 Effect of Strain Rate and Temperature

At the applied experimental conditions, changing the strain rate over 3–4 orders of magnitude has a relatively small impact on the peak strength (Figure 2.7a and b). For hard rocks, the strain rate sensitivity is commonly expressed in terms of a power law

$$\dot{\varepsilon} \propto \sigma^{n} \qquad 2.2$$

with a stress exponent *n* typically in the range of 25–50 in the brittle deformation regime (Lockner, 1995). For WIC and DOT samples deformed at P = 50 MPa and T = 100°C the corresponding *n*-values are ≈ 62 and ≈ 42, respectively, with a mean value of about 52. Alternatively, the strain rate sensitivity may be described by an exponential law.

$$\dot{\varepsilon} \propto \exp(\sigma / \sigma_0) \qquad 2.3$$

as sometimes used for shales (e.g., Chong et al., 1980; Swan et al., 1989; Kwon and Kronenberg, 1994). The associated constants σ_0, determined from the regression lines in Figure 2.7b, are 2.1 and 3.9 MPa for WIC and DOT shale, respectively, with similar regression coefficients for exponential and power law fitting ($r^2 \approx 0.85$). The average value is $\sigma_0 \approx 3.0$ MPa, similar to that measured for the strain rate sensitivity of Wilcox shale (Ibanez and Kronenberg, 1993; Kwon and Kronenberg, 1994). Assuming that the prevailing deformation processes do not change with strain rate, extrapolation of the stress–strain rate relationships (Equations 2.2 and 2.3) from relatively fast laboratory strain rate (5×10^{-4} s^{-1}) to long-term natural deformation rates (≈ 10^{-9}–10^{-14} s^{-1}) predicts a decrease of peak strength by about 23–45%. At the applied confining pressure of 50 MPa, also E decreases (almost linearly) with decreasing strain rate in semi-logarithmic scale (Figure 2.7c), consistent with observations on other shales (Chong and Boresi, 1990).

For shale, an increase of temperature promotes plastic deformation and a decrease of strength (Ibanez and Kronenberg, 1993; Masri et al., 2014). A similar behavior was observed for Posidonia shales with an almost linear decrease of peak strength with increasing T (Figure 2.6d). The fluctuation of peak strength of DOT samples at P = 50 MPa below about 100°C may be explained by dehydration and associated embrittlement of smectite into illite at temperatures between 60 and 100°C, as observed in natural shales (Horsrud et al., 1998; Peltonen et al., 2009). Similar to peak strength, for most samples Young's moduli decrease with increasing temperature (Figure 2.6e), which agrees with observations on Tournemire shale at T = 20–250°C and varying confining pressure (Masri et al., 2014). Conceivably, this decrease may be due to an increasing proportion of viscoplastic processes contributing to deformation with increasing temperature. Our estimates of E are based on the secant modulus at 50% of the peak stress, which is likely affected by non-reversible, temperature-dependent, deformation processes. The same explanation may hold for the strain-rate sensitivity of E (Figure 2.7c). It should be noted that also P and S-wave velocities of shales decrease considerably with increasing temperature (Johnston, 1987), suggesting that the dynamic Young's modulus is also sensitive to temperature variations.

Assuming that dislocation glide in clays is mainly responsible for the observed temperature sensitivity of strength, the corresponding constitutive relation is expressed as (Ibanez and Kronenberg, 1993):

$$\dot{\varepsilon} = A \cdot \exp\left(\sigma_{\max} / \sigma_0\right) \cdot \exp\left(-Q / \left(RT\right)\right) \qquad 2.4$$

where R is the gas constant, T is absolute temperature (in K), Q is the activation energy, and σ_0 and A are material constants. Strictly, the flow law is valid only at steady state creep conditions, but may be applied here as first order approximation with a pressure dependent constant $A = \mathrm{f}(P) = A_0 \cdot \exp(P/P_0)$. For our samples P_0 = -5.3 ± 1.5 MPa, obtained from Figure 2.5b. Applying Equation 2.4, the corresponding Arrhenius plot yields an average slope ($Q \cdot \sigma_0$) of ≈ 500 ± 160 (broken line in Figure 2.9c), resulting in an apparent activation energy of Q = 167 kJ/mol for σ_0 = 3.0 MPa. This value is comparable to activation energies of 87–181 kJ/mol calculated for dislocation glide of Wilcox shale samples, but higher than Q values (47–89 kJ/mol) for dislocation glide in biotite and muscovite (Ibanez and Kronenberg, 1993).

2.1.5.3 Effect of Fabric Anisotropy and Water Content

At ambient conditions, samples loaded parallel to bedding usually show slightly lower uniaxial compressive and tensile strength, but higher Young's moduli than deformed perpendicular to bedding (Table 2.2, Figure 2.3). The anisotropic strength may be explained by preferred initiation and propagation of axial cracks along the weak bedding planes if loaded parallel to bedding. In contrast, closing of bedding-parallel microcracks and easy deformation of the weak layers may explain low Young's moduli for bedding-normal deformation, close to the lower constant stress (Reuss) bound. Similar orientation-dependent properties were measured on other shales, often with a strength minimum for samples loaded 30–45° to bedding (Ibanez and Kronenberg, 1993; Niandou et al., 1997; Naumann et al., 2007; Islam and Skalle, 2013; Masri et al., 2014; Meier et al., 2013, 2015; Gholami and Rasouli, 2014).

The presence of water has a strong effect on strength and elasticity of Alum shale samples (Figure 2.8). Assuming a bilinear relation between strength and water content (broken lines in Figure 2.8b), the corresponding gradients of peak strength reduction with increasing water content are -210 MPa/wt% H_2O (or -8.1 MPa/S_w%) for hydration and -16 MPa/wt% H_2O (or -0.6 MPa/S_w%) for dehydration, respectively. A similar, but less pronounced, change in water sensitivity (hydration: -79 MPa/wt% H_2O, dehydration: -45 MPa/wt% H_2O) was noted by Ibanez and Kronenberg (1993) for Wilcox shale, deformed at ambient temperature and $P = 250$ MPa. The authors suggested that the water sensitivity for dried samples is related to presence of molecular water in clay interlayers, probably influencing dislocation glide and microcrack development. For water-added samples, the strong reduction of strength may be induced by low effective pressures due to increased pore pressure in undrained experiments. In addition to the above mentioned effects, the presence and amount of water may also lower the strength and elasticity of shales by physio-chemical processes, for example by osmotic swelling and capillary suction (Seedsman, 1987; Steiger, 1993; Schmitt et al., 1994; Van Oort, 2003; Thyagaraj and Rao, 2013).

2.1.5.4 Effect of Composition and Porosity

Finally, we attempt to correlate the fraction of weak phases (clay + kerogen), carbonates, and strong phases (quartz + feldspar + pyrite), as well as porosity with the measured strength (uniaxial compressive strength, tensile strength, triaxial peak strength) and Young's moduli. Treating these components individually, we mostly obtain poor correlations and almost no systematic correlation to maturity.

At ambient conditions, tensile strength is hardly influenced by porosity, except Posidonia shales, which appears to be slightly reduced with increasing porosity for bedding-parallel deformation (≈ -0.6 MPa/vol%$_{\Phi}$, Figure 2.10a). An increasing amount of the mechanically weak components (clay + TOC) appears to increase the tensile strength of Alum and Posidonia shales (≈ 0.3–0.7 MPa/vol%$_{clay+TOC}$, Figure 2.10b), in particular if loaded parallel to bedding. Conversely, σ_t of Posidonia shales decreases with an increasing amount of carbonates by about -(0.2–0.4) MPa/vol%$_{Cb}$ (Figure 2.10c) and increases with increasing fraction of hard components (≈ 0.2–0.4 MPa/vol%$_{QFP}$, Figure 2.10d). For Alum shale, σ_t appears to decrease with increasing strong mineral fraction (≈ -0.4 MPa/vol%$_{QFP}$).

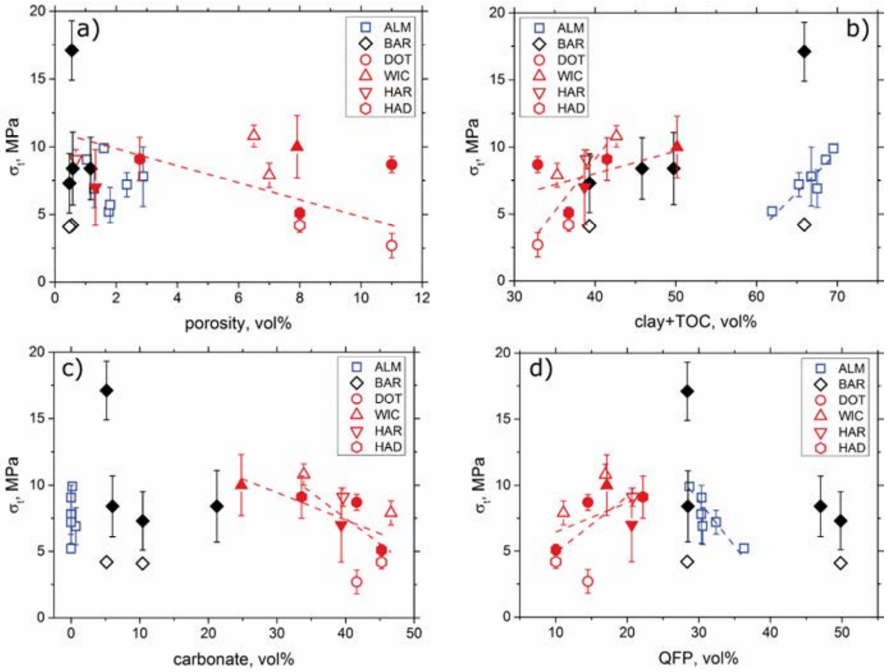

Figure 2.10 Variation of tensile strength σ_t with porosity (a), volumetric fraction of clay + TOC (b), carbonate (c), and QFP = quartz + feldspar + pyrite (d). All data were obtained at ambient temperature and pressure conditions. Open and filled symbols represent loading parallel and normal to bedding, respectively. Linear correlations are indicated by broken lines. ALM = Alum, BAR = Barnett, DOT = Dotternhausen, WIC = Wickensen, HAR = Harderode, and HAD = Haddessen shale.

The uniaxial compressive strength σ_c of Posidonia shales decreases with increasing porosity (≈-2.8 MPa/vol%$_{\Phi}$, Figure 2.11a) and increases slightly with the amount of weak components (≈ 0.7–3.0 MPa/vol%$_{clay+TOC}$, Figure 2.11b). The amount of carbonates present has little effect on strength with the exception of Posidonia shale loaded parallel to bedding (≈ -3 MPa/vol%$_{Cb}$, Figure 2.11c). Contrarily, an increasing strong-phase fraction strengthens Posidonia shale by about 4 MPa/vol%$_{QFP}$ (Figure 2.11d). For the two other shales σ_c is hardly influenced by composition and porosity.

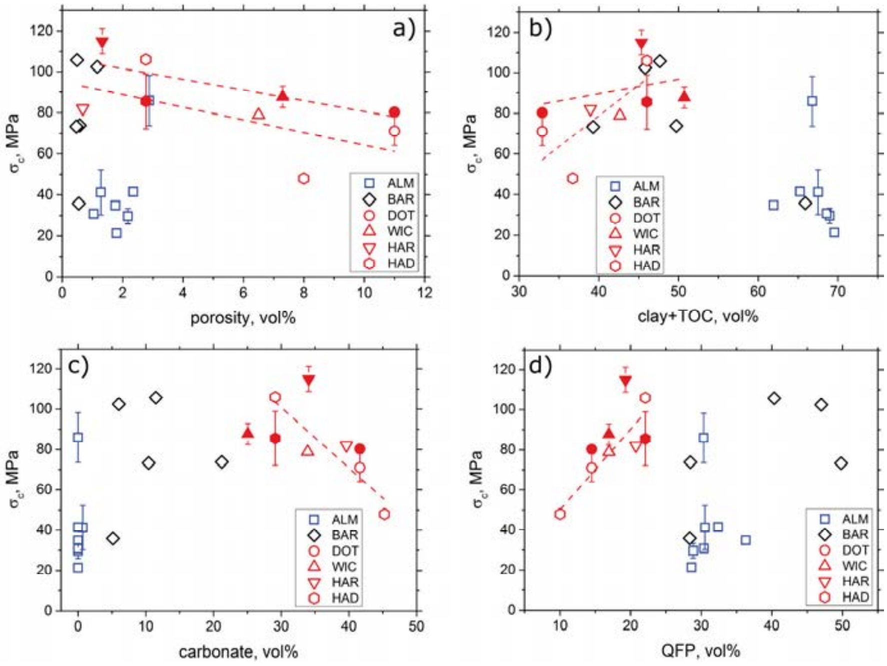

Figure 2.11 Variation of uniaxial compressive strength σ_c with porosity (a), volumetric fraction of clay + TOC (b), carbonate (c), and QFP = quartz + feldspar + pyrite (d). All data were obtained at ambient temperature and pressure conditions. Open and filled symbols represent measurements parallel and normal to bedding, respectively. Linear correlations are indicated by broken lines. ALM = Alum, BAR = Barnett, DOT = Dotternhausen, WIC = Wickensen, HAR = Harderode, and HAD = Haddessen shale.

As expected from the linear relationship between σ_c and E (Figure 2.3b), the Young's moduli determined at atmospheric conditions reveal quite similar trends (Figure 2.12). For Posidonia shale we measured a reduction of E with increasing porosity (≈ -0.6 GPa/vol%$_{\Phi}$, Figure 2.12a) and an increase of E with higher fraction of strong (QFP) phases (≈ 0.6 GPa/vol%$_{QFP}$, Figure 2.12d). If loaded parallel to bedding, increasing clay and kerogen fraction results in increasing Young's moduli of Posidonia shale (≈ 0.4 GPa/vol%$_{\text{clay+ TOC}}$, Figure 2.12b) and decreasing E values with the amount of carbonates by ≈ -0.3 GPa/vol%$_{\text{Cb}}$ (Figure 2.12c).

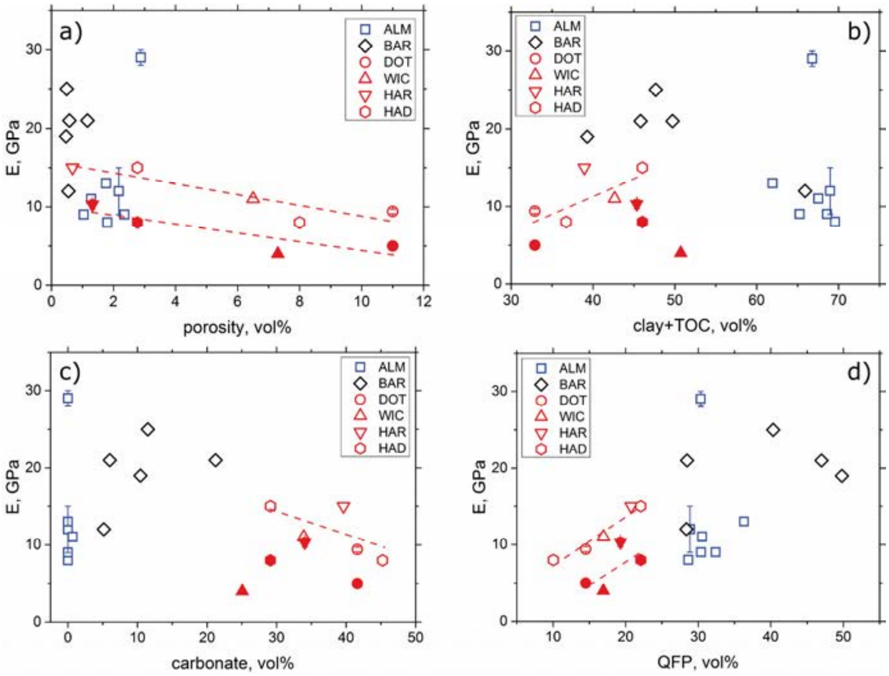

Figure 2.12 Variation of Young's modulus *E* with porosity (a), volumetric fraction of clay + TOC (b), carbonate (c), and QFP = quartz + feldspar + pyrite (d). All data were obtained at ambient temperature and pressure conditions. Open and filled symbols represent measurements parallel and normal to bedding, respectively. Linear correlations are indicated by broken lines. ALM = Alum, BAR = Barnett, DOT = Dotternhausen, WIC = Wickensen, HAR = Harderode, and HAD = Haddessen shale.

Bedding-normal deformation of Posidonia shale at 50 MPa pressure and temperatures of 20–200°C also reveals that a change of porosity affects the peak differential strength σ_{max} if deformed at 20°C by about -6 MPa/vol%$_{\Phi}$ and somewhat less (≈ -2 MPa/vol%$_{\Phi}$) at higher temperatures (Figure 2.13a). Similar to σ_c, the amount of strong phases increases the peak strength by ≈ 2– 6 MPa/vol%$_{QFP}$ (Figure 2.13d), but, in contrast to σ_c, σ_{max} slightly decreases with increasing fraction of weak components (≈ -(1–3) MPa/vol%$_{clay+\ TOC}$) and σ_{max} increases with increasing carbonate content (≈ 2–5 MPa/vol%$_{Cb}$, Figure 2.13b and c). For clarity, in Figure 2.13 and Figure 2.14 only fits for 50 MPa pressure are shown. At 100 MPa pressure the correlations are weaker.

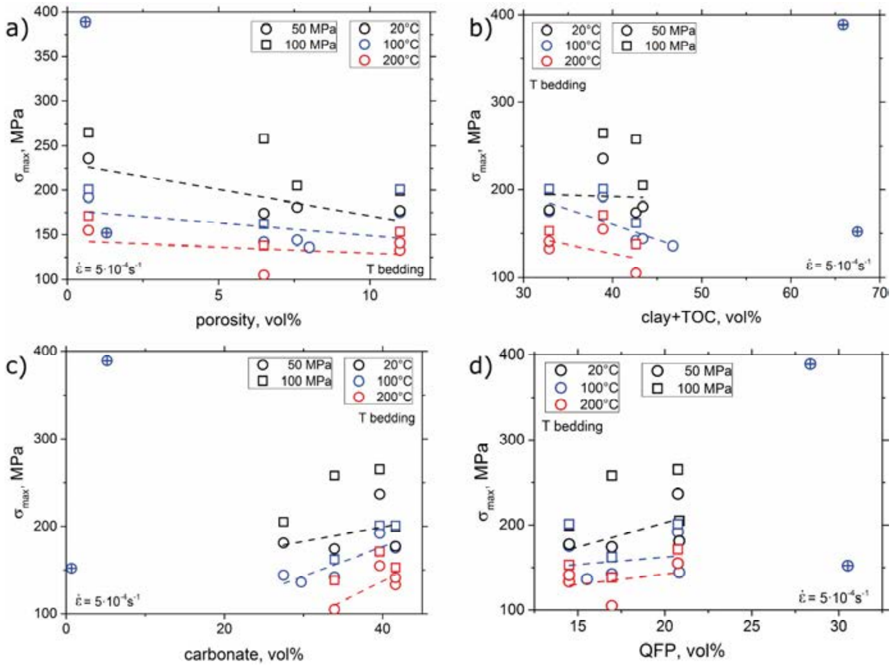

Figure 2.13 Influence of porosity (a), fraction of clay+TOC (b), carbonates (c), and QFP=quartz+feldspar+pyrite (d) on the peak differential strength of Posidonia shales at elevated pressure and temperature. Deformation conditions are indicated. Crossed symbols represent data of Alum (bottom) and Barnett (top) shale. Linear correlations at P = 50 MPa are indicated by broken lines.

The static Young's modulus measured in triaxial deformation consistently decreases with increasing porosity (≈ -0.6 GPa/vol%$_{\Phi}$), almost similar to the decrease measured at ambient conditions (Figure 2.14a). No correlation of E with a variation of carbonates or weak phases is evident (Figure 2.14 b and c), but E increases with increasing fraction of hard minerals by about 0.9 GPa/vol%$_{QFP}$ (Figure 2.14d).

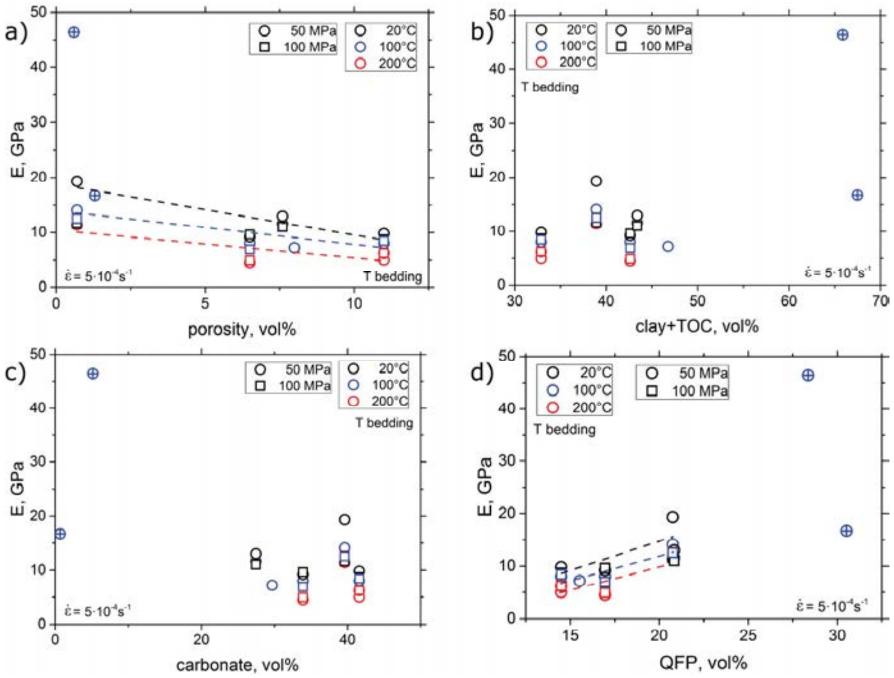

Figure 2.14 Influence of porosity (a), fraction of clay+TOC (b), carbonates (c), and QFP = quartz+feldspar+pyrite (d) on Young's modulus of Posidonia shales at elevated pressure and temperature. Deformation conditions are indicated. Crossed symbols represent data of Alum and Barnett shale. Linear correlations at P = 50 MPa are indicated by broken lines.

In summary, the tensile strength of individual shale formations appear to be most consistently affected by the fraction of weak components. Intuitively, this may be expected because of distributed stress concentration in the process zone in front of a tensile crack in the presence of relatively ductile components. For Posidonia shale, compressive strength and Young's modulus decrease with increasing porosity. This correlation seems to hold also for a comparison of all shales, if for Alum shale the total (He-) porosity is used, which is considerably (≈ 8%) higher than the MIP porosity. Presumably, potential correlations between parameters shown in Figure 2.10–Figure 2.14 are obscured by the combined effect of the various constituents and porosity on strength and elasticity. For example, for Posidonia shale deformed at ambient conditions, a positive correlation of strength with the strong mineral fraction often coincides with a negative correlation with carbonates or porosity. Similar observations exist for the peak strength of Opalinus clay depending on carbonate content, which shows different trends for the 'sandy' and 'shaly' facies (Kaufhold et al., 2013). In addition, the different strength of individual constituents at different *P*–*T* conditions likely yield different apparent correlations between bulk strength of composites and fraction of weak or hard phases and carbonates. Differences in the microstructure, cementation and water content are also expected to affect the correlations and may explain the relatively high strength of Barnett shale at elevated pressure and temperature.

2.1.5.5 Effective Composite Approximation

Irrespective of the potential microstructural and chemical influences on the mechanical behavior, we compare the measured parameters with continuum mechanics-based bounds, i.e., with the upper strength (Voigt) bound assuming isostrain rate in all phases and with the lower strength (Reuss) bound assuming isostress conditions for each phase of an multiphase shale compound (e.g., Mavko et al., 2009). These empirical bounds rely just on the volume fraction of the constituents and cannot capture chemical clay activity and structural or cementation effects, for example the effect of grain size on the strength of carbonates (Figure 2.4b) or the anisotropy of mechanical parameters with respect to loading direction relative to bedding orientation (Figure 2.3 and Figure 2.8). Furthermore, the bounds were initially introduced to describe the composition-dependent elastic behavior, but have been also applied to describe viscous deformation of two-phase materials (e.g., Rybacki et al., 2014). To interpret the data, we use the generalized mixture rule (GMR) proposed by Ji et al., (2004) and Ji (2004):

$$M_c^s = \sum_{i=1}^{N} \left(f_i M_i^s \right) \qquad 2.5$$

where M is the material property under consideration (strength, elastic modulus) and f is the volume fraction of phase i of a composite (index c) with N different phases $\left(\sum_{i=1}^{N} f_i = 1 \right)$. The empirical parameter s is usually restricted to the range between -1 and 1 and may account to a certain degree for microstructural effects. Simplifying the constituents of shales into weak (Cly + TOC), intermediate (Cb) and strong (Qtz + Fsp + Py) phases (cf., Figure 2.4), we yield the upper strength Voigt bound (USB) for $s = 1$:

$$M_c = f_{ClyTOC} M_{ClyTOC} + f_{Cb} M_{Cb} + f_{QFP} M_{QFP} \qquad 2.6$$

and the lower Reuss strength bound (LSB) for $s = -1$:

$$\frac{1}{M_c} = \frac{f_{ClyTOC}}{M_{ClyTOC}} + \frac{f_{Cb}}{M_{Cb}} + \frac{f_{QFP}}{M_{QFP}} \qquad 2.7$$

The influence of porosity Φ may be considered simply by:

$$M_{cp}^{sp} = \left(1 - \phi\right) M_{cnop}^{sp} + \phi M_{\phi}^{s} = \left(1 - \phi\right) M_{cnop}^{sp} \qquad 2.8$$

where the subscripts *cp* and *cnop* indicate the material properties of a porous and non-porous rock, respectively. The superscript *sp* is another empirical parameter related to porosity. In the elastic regime, it is predicted to be in the range of 0.25 for pores of random geometry and 0.5 for spherical pores (Ji et al., 2004). M_{Φ} equals zero because of the vanishing strength and elasticity of pore space. Here, we assume sp = 0.25 based on the complex geometry of pores (Figure 2.1), which yields:

$$M_{cnop} = M_{cp} \,/\, \left(1-\phi\right)^{4} \qquad 2.9$$

which may hold up to ≈ 20% porosity.

The measured data and calculated bounds are given in Table 2.5 for tests performed at P = 0.1 MPa, T = 20°C and in Table 2.6 for P = 50 MPa, T = 100 MPa, respectively. All data are corrected for the influence of porosity using Equation 2.9. For shales, most porosity corrected uniaxial compressive strength data and associated Young's moduli are within the calculated bounds (Figure 2.15a and b), whereas for the reference samples σ_c of sandstone and limestone are below the LSB (Table 2.5). The latter may be related to the effect of grain size d and can be corrected for assuming a Hall Petch relationship ($\sigma \sim \sigma_0 + k/\sqrt{d}$) that accounts for pile up of dislocations at grain boundaries. The measured tensile strength, however, is often above the USB for shales and below the LSB for the reference samples (Table 2.5), but it is still bounded by the tensile strength of the strongest and weakest minerals. Therefore, σ_t appears not to be related to the volumetric proportion of different minerals. Instead, the interaction of pores or preexisting microcracks may affect tensile cracking and the presence of pores and weak phases may control their propagation and interaction as indicated by correlations shown in Figure 2.10. A positive correlation between tensile strength and clay fraction of soils was also noted by Barzegar et al. (1995), who showed that σ_t depends on clay size and type and associated cation exchange capacity. For clays, the tensile strength can be also empirically related to the mode I fracture toughness (Wang et al., 2007).

Table 2.5 Calculated bounds and GMR data at ambient conditions ($P = 0.1$ MPa, $T = 20$ °C).

Sample	$\sigma^*_{c\_LSB}$ MPa	$\sigma^*_{c\_n}$ MPa	$\sigma^*_{c\_GMR}$ MPa	$\sigma^*_{c\_p}$ MPa	$\sigma^*_{c\_USB}$ MPa	$E^*_{\_LSB}$ GPa	$E^*_{\_n}$ GPa	$E^*_{\_GMR}$ GPa	$E^*_{\_p}$ GPa	$E^*_{\_USB}$ GPa	$\sigma^*_{t\_LSB}$ MPa	$\sigma^*_{t\_n}$ MPa	$\sigma^*_{t\_GMR}$ MPa	$\sigma^*_{t\_p}$ MPa	$\sigma^*_{t\_USB}$ MPa
ALM1	37.0	-	52.3	43.1	159	4.9	-	7.3	11.6	28.4	3.4	-	4.2	7.3	7.4
BAR1	37.9	-	53.9	36.7	157	5.0	-	7.7	12.3	29.1	3.5	17.5	4.3	4.3	7.4
DOT1	59.4	128.0	92.5	113.2	181	8.5	8.0	16.9	15.0	43.8	4.9	13.9	6.1	4.3	8.5
WIC1	50.8	114.8	77.7	103.1	169	7.0	5.2	13.2	14.4	39.1	4.4	13.1	5.4	14.1	8.0
HAR1	57.3	118.3	90.7	84.3	187	8.1	10.3	16.0	15.4	43.4	4.8	7.2	6.0	9.4	8.7
HAD2	49.4	95.8	76.1	118.8	175	6.8	9.0	12.5	16.8	38.7	4.3	10.2	5.4	4.7	8.2
NOV	451	451	451	451	451	83	83	83	83	83	18.2	18.2	18.2	18.2	18.2
FST	164	141	289	141	396	24.1	30.9	51	30.9	73.8	10.8	8.8	13.7	8.8	16.2
BST	336	131	414	131	442	55.6	74.5	75	74.5	81.3	16.1	6.0	17.2	6.0	17.9
LIM	208	208	208	208	208	62	62	62	62	62	9.9	9.9	9.9	9.9	9.9
MAR	208	101	208	101	208	62	49	62	49	62	9.9	7	9.9	7	9.9
COA	26	26	26	26	26	3.4	3.4	3.4	3.4	3.4	2.5	2.5	2.5	2.5	2.5
GRA	242	230	364	230	429	37.0	70	65	70	78.8	13.7	12	15.9	12	17.4

σ^*_c, E^*, σ^*_t = unconfined compressive strength, Young's modulus, and tensile strength, respectively, recalculated for porosity-free samples using Equation 2.9. Subscripts: n = normal, p = parallel to bedding, LSB = lower strength bound, USB = upper strength bound, GMR = general mixture rule calculation with $s = -0.25$ (cf. Equation 2.5). Input data for calculations are highlighted in bold. USB and LSB values given in italics do not bound the data. For abbreviations, see nomenclature.

Table 2.6 Calculated bounds and GMR data at P = 50 MPa, T = 100 °C.

Sample	$\sigma^*_{LSB\_Bio}$ MPa	σ^*_{LSB} MPa	$\sigma^*_{\_n}$ MPa	$\sigma^*_{GMR\_Bio}$ MPa	σ^*_{USB} MPa	$\sigma^*_{USB\_Bio}$ MPa	$E^*_{LSB\_Bio}$ GPa	E^*_{LSB} GPa	$E^*_{\_n}$ GPa	$E^*_{GMR\_Bio}$ GPa	E^*_{USB} GPa	$E^*_{USB\_Bio}$ GPa
ALM1	119	205	160	149	324	277	5.1	9.8	17.6	7.2	23.3	20.9
BAR1	121	206	399	151	319	273	5.3	10.1	47.5	7.5	24.0	21.7
DOT1	167	245	279	207	322	296	8.7	15.6	12.8	15.6	35.9	34.6
WIC1	149	231	186	186	314	282	7.3	13.4	10.5	12.4	32.3	30.7
WIC2	140	221	190	172	301	266	6.7	12.4	10.1	10.9	29.9	28.1
HAR1	164	246	198	207	335	308	8.3	15.0	14.5	14.8	35.3	33.9
HAD1	148	232	204	187	328	296	7.1	13.1	16.4	12.0	31.9	30.2
NOV	699	699	699	699	699	699	58.5	58.5	58.5	58.5	58.5	58.5
FST	390	494	446	512	626	619	22.6	33.3	49.7	39.1	52.8	52.5
BST	608	651	626	660	688	686	44.3	50.8	97.5	53.8	57.4	57.4
LIM	321	321	321	321	321	321	50.8	50.8	50.8	50.8	50.8	50.8
MAR	321	321	234	321	321	321	50.8	50.8	64	50.8	50.8	50.8
COA/Bio	86	155	155/86	86	155	86	3.6	7.1	7.1/3.6	3.6	7.1	3.6
GRA	507	589	731	606	670	667	32.4	42.3	64.9	47.5	55.8	55.6

σ^*, E^* = peak compressive strength and Young's modulus, respectively, recalculated for porosity-free samples using Equation 2.9. Subscripts: n = normal to bedding, LSB = lower strength bound, USB = upper strength bound, USB_Bio and LSB_Bio = bounds calculated with input data of biotite instead of coal, GMR_Bio = general mixture rule calculation with s = -0.25 (cf. Equation 2.5) and using biotite input data. Input data for calculations are highlighted in bold. USB, LSB values given in italics do not bound the data. For abbreviations, see nomenclature.

Under triaxial conditions, most peak stresses and E moduli of shales are below the LSB, except Barnett shale, which is above the *USB* (small symbols in Figure 2.15c and d). Also, the strength of sandstones and marble are below the LSB, whereas the strength of granite as well as Young's moduli of granite, marble and Bentheim sandstone are above the *USB* (Table 2.6). The bounds depend critically on the peak strength of the endmember phases. Here, we assumed 155 MPa measured on the coal sample as a weak endmember. If we use instead 86 MPa estimated from the flow laws of biotite provided by Kronenberg et al. (1990), almost all strength data are within the bounds (except Barnett shale and Westerly granite, Figure 2.15c, large symbols). Similarly, reduction of the measured Young's modulus of 7.1 GPa for coal by about half to 3.6 GPa shifts the LSB below all measured data (Figure 2.15d, Table 2.6). We therefore conclude that at elevated pressure and temperature the presence and strength of clay minerals instead of the organic matter may constrain the lower strength bound.

Ji et al. (2004) suggested that for a fraction of strong minerals $f_{strong} < 0.5$ the parameter s is close to -0.25 for composites with a weak-phase supported structure and for $f_{strong} > 0.7$ the parameter $s = +0.25$ for aggregates with a strong-phase supported structure. Since for the investigated shales $f_{QFP} < 0.3$ (Table 2.1), we determined the corresponding (GMR-) values for porosity-free samples using $s = -0.25$ and, under triaxial conditions, with the reduced strength (86 MPa) and Young's modulus (3.6 GPa) for the weak-phase. The resulting values may represent volumetrically weighted mechanical data of isotropic shales. However, most estimated data do not fit very well to the measured values (Figure 2.15, Table 2.5 and Table 2.6), even if we take the average of values measured parallel and perpendicular to bedding as first order approximation of isotropic data. For example, the calculated uniaxial compressive strength of shales is on average 23% lower than the measured mean data and the calculated Young's moduli are 26% higher. Under triaxial conditions, the fits between predicted values and those measured normal to bedding are better, except Barnett shale (Figure 2.15). Ignoring the latter, the estimated strength and Young's moduli are on average 7% lower than the data measured normal to bedding. As mentioned above, the deviation may be explained by the anisotropic nature of shales, chemical bonding or hydrogen effects and by local stress heterogeneities, which cannot be captured by the GMR model.

In addition, we applied a nonlinear least-square fitting (Levenberg–Marquardt) procedure to estimate the parameter s for the porosity-corrected (assuming $sp = 0.25$, cf. Equation 2.9) mechanical data measured normal and parallel to bedding. The resulting s-values vary substantially between -0.75 and +4.0 with no systematic trend (Table 2.7). Restricted to the uniaxial and triaxial strength, the best fit s-values range from 0.05 to 0.47 with a mean value of

0.23, which is close to the value of 0.25 estimated by Ji et al. (2004) for composites with a high fraction of strong phases (> 0.7), but which is far above the amount of f_{QFP} of our shales (< 0.3). It should be mentioned, however, that the number of data for fitting is rather limited. Also, the s-values proposed by Ji et al. (2004) were estimated from two-phase materials and may differ for multiphase compounds. Alternatively, we used a combination of Equations 2.5 and 2.8, yielding:

$$M_{\varphi} = (1-\phi)^{\frac{1}{sp}} \cdot \left(\sum_{i=1}^{N} \left(f_i M_i^s \right) \right)^{\frac{1}{s}} \tag{2.10}$$

for simultaneous fitting of *sp* and *s* directly on the measured (porous) shale data. The resulting *sp* values vary between 0.05 and 0.76 (Table 2.7) with an average value of 0.28, which is close to the suggested value of 0.25 for pores with random geometry. Again, no systematic trend can be observed for the associated *s* values and the corresponding misfit between measured and fitted data varies between 4% and 52%, with an average of about 27%. Note that the fit parameters on our limited dataset also depend on the applied algorithm. Using a orthogonal distance (between data and fitted curve) regression analysis instead of the standard Levenberg– Marquardt formulation would result in best fit *s* values close to zero, which represents the geometrical mean (Ji et al., 2004).

In summary, the effect of porosity and composition on the strength and elastic properties of shales estimated from their volumetric proportion can be described by a (generalized) mixture rule formulation as a first order approximation for shales of the same formation using *sp* = 0.25 and *s* = -0.25. For successful application, this approach requires the knowledge of the strength and elastic moduli of quartz, calcite and clay at all *P–T* conditions of interest. It may result in large errors if various formations with different cementation, fabric etc. are compared. For anisotropic rocks, other theories like shear lag models based on fiber-loading theory (e.g., Ji and Zhao, 1994, Covey-Crump et al., 2013) may give better results, although they are more complex than the GMR model and usually limited to two-phase composites.

Considering a black shale layer of about 100 m thickness, the effect of changing *P–T* conditions on the strength and Young's modulus is negligible compared to a small variations of porosity or composition. Within this depth interval, the *P–T*-related net increase of strength is ≈ 0.5 MPa/100 m, corresponding to an increase of ≈ 0.5 vol% strong minerals or ≈ 1 vol% carbonates, or to a decrease of ≈ 0.2 vol% weak phases or ≈ 0.1 vol% porosity. The same effect may be expected for a minor change (several thousandth to hundredth wt%) of H_2O content. On the other hand, for different shale deposits that vary in depth between about 1 and 10 km, the *P–*

T conditions have a pronounced influence on the magnitude of the mechanical data and the behavior can change from brittle to ductile, therefore affecting local deviatoric stresses and preexisting fracture networks that may control the prospectivity of gas shales. The issue of brittleness will be discussed in an accompanying second paper.

Table 2.7 GMR fitting of mechanical shale data.

Parameter	T, °C	20						100	
	P, MPa	0.1						50	
		σ_{c_n} MPa	σ_{c_p} MPa	E_n GPa	E_p GPa	σ_{t_n} MPa	σ_{t_p} MPa	σ_{max_n} MPa	E_n GPa
		Fit on porosity-corrected (pore-free) data							
sp		≡ 0.25							
s		0.18	0.05	-0.75	-0.11	4.00	0.91	0.47	0.21
		Fit on porosity-uncorrected data (Equation 2.10)							
sp		0.33	0.76	0.12	0.14	0.39	0.33	0.15	0.05
s		0.10	-0.24	-0.52	0.02	3.32	0.82	0.83	1.91

σ_c, σ_{max}, σ_t , E = unconfined compressive strength, peak strength, tensile strength and Young's modulus, respectively. Subscripts: *n* = normal, *p* = parallel to bedding, *s* and *sp* are GMR fit parameters (cf. Equation 2.5 and 2.10). For abbreviations, see nomenclature.

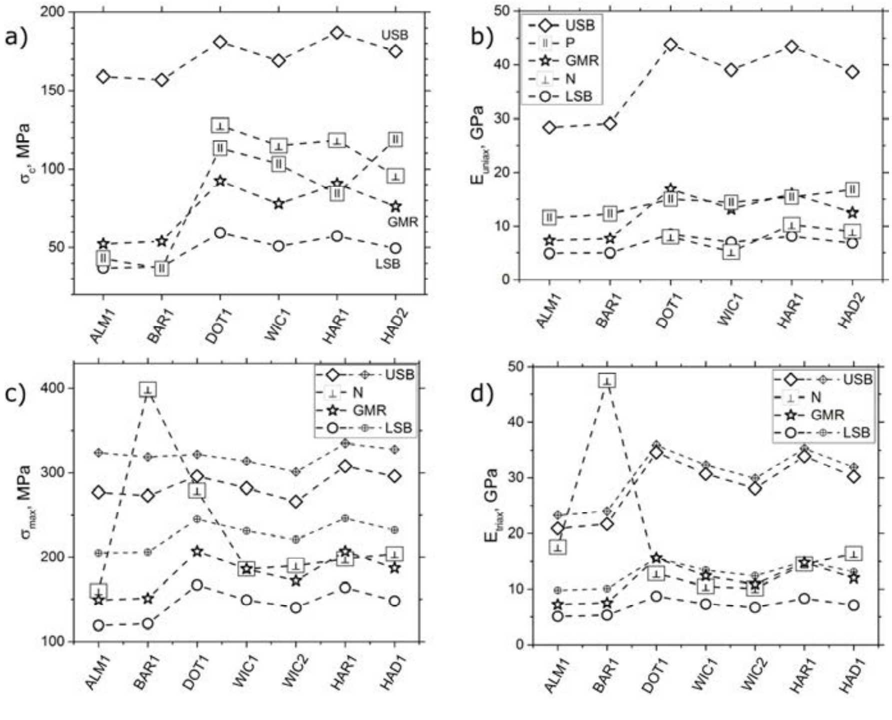

Figure 2.15 Peak stress and Young's modulus of shales obtained at P = 0.1 MPa, T = 20°C (a and b) and at P = 50 MPa, T = 100°C (c and d). LSB and USB indicate lower and upper strength bound, GMR is general mixture estimate using s = -0.25, ll and *T* are measured data parallel and normal to bedding, respectively. Under triaxial conditions, the calculations are based on the reduced strength and moduli estimated for biotite; those for coal as weak-phase are indicated by small crossed symbols (cf., Table 2.4). Note that all data refer to non-porous rocks. ALM = Alum, BAR = Barnett, DOT = Dotternhausen, WIC = Wickensen, HAR = Harderode, and HAD = Haddessen shale.

2.1.6 Conclusions

Laboratory experiments on anisotropic shale samples from different origins with varying mineralogy and maturity show brittle to semibrittle deformation behavior, depending on the applied pressure, temperature and strain rate, but also on porosity, mineral assemblage, water content and loading direction with respect to bedding orientation. In the predominantly brittle regime, compressive strength and static Young's modulus show in most cases a good, nearly linear, correlation at pressures below about 100 MPa.

The pressure dependence of mechanical strength is nonlinear at shallow depth (< 2–4 km, $P \lesssim 50$–100 MPa) and the internal friction coefficients of the investigated shales vary considerably between ≈ 0.2 and 1.1. Conversely, increasing temperature yields an almost linear decrease of strength, which may be partially attributed to dislocation glide of clay minerals. The influence of strain rate on peak stress can be described by a power-law or exponential law with parameters typical for hard rocks, if deformed in the brittle regime.

For a specific shale formation and at given P–T conditions, the effect of small fluctuations of porosity and composition on the compressive strength and Young's modulus may be roughly described by their volumetric fraction using a GMR approach with the suggested parameters $sp = 0.25$ for random pore geometry and $s = -0.25$ for a weak-phase supported structure. This approach does not capture the influence of anisotropy, water content and other physiochemical effects and absolute values may have a large bias (≲25%, depending on P–T conditions). The tensile strength, however, cannot be adequately predicted by the GMR approach.

ACKNOWLEDGMENTS

We thank the GASH and GeoEn sponsors and teams for financial support and sharing data with us, Stefan Gehrmann for sample and thin section preparation, Michael Naumann for assistance with deformation experiments in the Paterson apparatus, Marc Rück for some uniaxial compressive and tensile strength data of the reference rocks, Luiz Morales for FIB foil preparation, and Joyce Schmatz for BIB polishing of some shales. The manuscript benefitted from comments of two anonymous reviewers.

3 INFLUENCE OF BOREHOLE DIAMETER ON THE FORMATION OF BOREHOLE BREAKOUTS IN BLACK SHALE[2]

SUMMARY

We performed a series of borehole breakout tests on Posidonia shale to study the influence of borehole diameter on borehole stability in unconventional black shale. Thick-walled cylindrical samples (20–80 mm long, 10–50 mm in diameter) with varying borehole diameters of 1–19 mm drilled perpendicular to bedding were loaded under increasing hydrostatic pressures until formation of borehole breakouts. The critical hydrostatic pressure for breakout formation decreased significantly from about 275 MPa for samples with 1 mm borehole diameter, to 89 MPa for those containing a 19 mm borehole, approaching the uniaxial compressive strength of the material. The observed scale effect was fitted to various failure criteria predicting fracture initiation at a depth of about 0.15 mm around the borehole wall in the fine-grained shale.

3.1 Introduction

Deviated and horizontal drilling is common practice in the oil and gas as well as in the geothermal industry. This drilling technique allows access to far-reaching target horizons of limited thickness and enables enhanced reservoir stimulation campaigns by introducing artificial fracture networks which is needed to increase the productivity of geothermal wells and of low permeable oil and gas shale reservoirs (Allix et al., 2010; Boyer et al., 2006). Also, reduced above-ground ecological and economic footprints benefit from deviated drilling, which increasingly outbalance sub-surface drilling problems (Allen et al., 1997; Fuller, 2010). Therefore, the rock mass is penetrated in different orientations and with different drill bit sizes, inducing a complicated stress field in the circumference of the borehole. Usually, the mud pressure and the orientation of the borehole are adjusted to avoid stress-related borehole instabilities (Al-Ajmi and Zimmerman, 2009). Problems due to stress-induced borehole instabilities are vast, especially in shale formations (Grabielsen et al., 2010; Pasic et al., 2007). Instabilities can lead to mud loss, stuck pipe, reaming, and the necessity to side-track a lost hole as for example observed in high-angle wells drilled in an organic-rich shale formation in the North Sea (Økland and Cook, 1998).

---

[2] T. Meier, E. Rybacki, A. Reinicke, G. Dresen, Influence of borehole diameter on the formation of borehole breakouts in black shale, International Journal of Rock Mechanics and Mining Sciences, Volume 62, September 2013, Pages 74-85, ISSN 1365-1609, http://dx.doi.org/10.1016/j.ijrmms.2013.03.012.

Significant borehole enlargement due to formation of borehole breakouts and a subsequent lost hole was also observed in fractured Cretaceous shale (Ottesen, 2010).

A commonly neglected factor in reducing the risk of borehole instabilities is the influence of the borehole diameter. From laboratory experiments it is known that the hoop stress necessary to initiate borehole instabilities, i.e., borehole breakouts, increases with decreasing borehole diameter (Cuisiat and Haimson, 1992). Therefore, borehole instabilities are more likely to occur at large boreholes. Several authors analyzed this scale effect in different sandstones using hydrostatic loading experiments of thick-walled hollow cylinders (Cuss et al., 2003; Dresen et al., 2010; Papamichos et al., 2010; van den Hoek et al., 1992). In close vicinity to the central borehole stresses concentrate, forming a compressive stress field. In cylindrical coordinates, the tangential stress σ_Θ, vertical stress σ_v, and radial stress σ_r are related to the applied hydrostatic pressure, P_o, by:

$$\sigma_\theta = P_o \frac{b^2}{b^2 - a^2}\left(1 + \frac{a^2}{r^2}\right) \tag{3.1}$$

$$\sigma_r = P_o \frac{b^2}{b^2 - a^2}\left(1 - \frac{a^2}{r^2}\right) \tag{3.2}$$

$$\sigma_v = P_o \frac{b^2}{b^2 - a^2} \tag{3.3}$$

where *b* is the specimen radius, *a* is the borehole radius, and *r* is the point of interest (Hoskins, 1969; Jaeger et al., 2007). For tangential stress exceeding the strength of the rock, borehole breakouts develop under in-situ conditions (Barton et al., 1988). For sandstones tested under laboratory conditions, breakouts occur in small boreholes (≤10 mm diameter) at significantly increased pressures compared to large boreholes, where the critical stress for breakout formation appears to be independent of size (Dresen et al., 2010; van den Hoek et al., 1994).

Here, we present results from an experimental study of thick-walled cylinders with varying borehole diameter to study the observed scale effect and breakout mechanisms in black shales.

3.2 Test Material

Lower Jurassic Posidonia shale samples were collected from a quarry in the Southwest German Basin (labeled PS) and from cores of a ~20 years old well located in the Northwest German Basin (labeled PN). PS is a freshly blasted, laminated immature oil shale. Maximum burial depth is estimated to be 600–700 m (pers. comm. M. Jaeger, Holcim AG). For PN samples, maximum burial depth is ~1800 m (Jochum et al., 1995), associated with a high degree of compaction and maturity. Porosity and average pore radii were determined by mercury injection porosimetry (*MIP*, Macro- and Mesopore unit from Fisons Instruments) showing strongly reduced values for PN compared to PS (Table 3.1). Composition of PN and PS was measured by X-ray diffraction analysis (*XRD*, STOE STADI P diffractometer with Cu Kα radiation) combined with Rietveld-refinement analysis (Lutterotti et al., 2007). Main mineral components in both rock types are calcite, quartz, mainly illite within the clay content, and organic matter (Table 3.1). Accessory framboidal flakes of pyrite are oriented parallel to the lamination (Figure 3.1a). Microstructures were analyzed using optical microscopy of thin sections and with the help of the focused ion beam technique coupled with standard scanning electron microscopy (FIB, FEI Quanta 3D FEG dual beam machine). The lamination was identified as an alignment of grains, fossil fragments and stringers of organic matter (Figure 3.1c). The typical grain size of calcite, quartz, and pyrite is 3–4 mm. The grains are floating within stringers of organic matter or are trapped in the calcareous cement, inhibiting grain-to-grain contacts perpendicular to bedding. However, parallel to bedding, grain contacts between calcite, quartz or pyrite grains are frequently observed (Figure 3.1c). The water content was determined by drying of specimens at 105°C until weight remained constant. The water content is approximately 2 wt% for PS and 1 wt% for PN. Total organic carbon (*TOC*) was determined using a Leco SC-632 instrument. Maturity data (R_m) in Table 3.1 were taken from (Littke et al., 1991) for PN and estimated from T_{max} of Rock-Eval pyrolysis data (Peters et al., 2008) for PS.

Table 3.1 Petrophysical parameters of Posidonia Shale from the NW German Basin (PN) and the SW German Basin (PS).

	PS	PN
Maturity	immature	mature
Porosity [%]	10.4±0.6	1.1±0.3
Avg. pore radius [nm]	11.8±1.0	< 4.1
Calcite content [wt%]	55.6±0.6	47.3±0.5
Clay content [wt%]	23.2±1.5	27.8±1.6
Quartz content [wt%]	16.2±0.4	17.2±0.4
Pyrite [wt%]	4.9±0.2	5.3±0.2
Total organic carbon, TOC [wt%]	8.3±0.2	5.8±0.3
Water content [wt%]	~2	~1

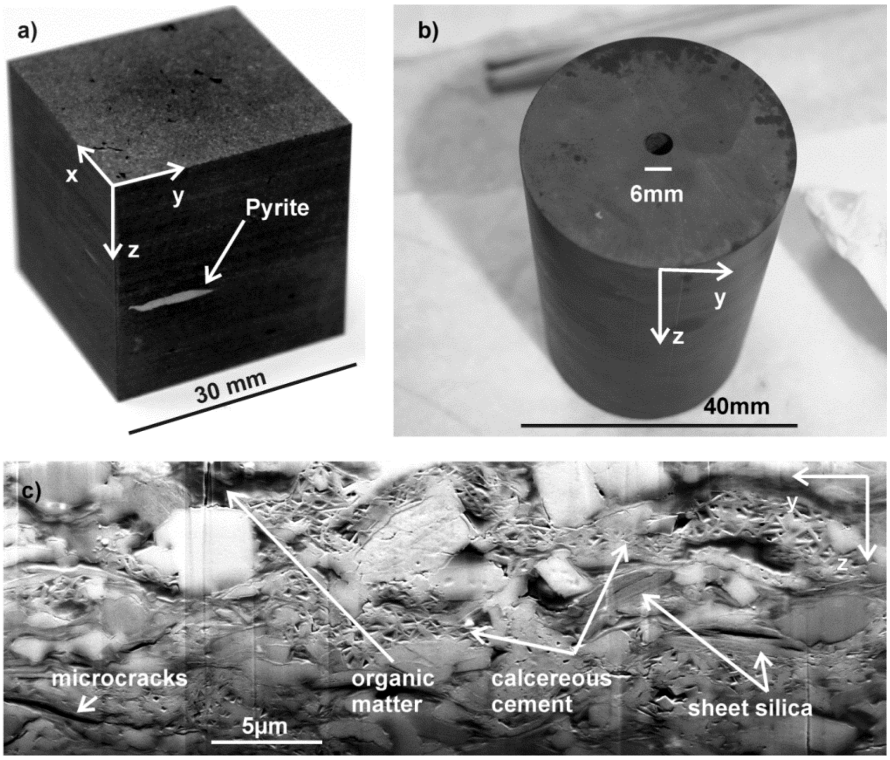

Figure 3.1 a) Cube of PS sample showing pyrite along bedding. x–y plane is parallel to bedding. b) Cylindrical specimen (40 x 80 mm) with a 6 mm borehole perpendicular to bedding planes. c) SEM image of a FIB section perpendicular to bedding of PS. Note pore space and organic matter.

3.3 Experimental Procedure

3.3.1 Specimen Preparation

For geomechanical characterization a total of 5 PN and 7 PS cylindrical specimens with 25 mm diameter and 50 mm length were prepared for uniaxial compression tests. For PS, three cylinders were oriented with the bedding plane parallel to the specimen axis and four cylinders were oriented with the bedding planes perpendicular to the specimen axis. For PN, two cylinders were cored parallel and three perpendicular to the bedding, respectively. Additionally, one solid cylinder of 40 mm diameter and 80 mm length with bedding planes perpendicular to the specimen axis was prepared from PS to study the compaction behavior under hydrostatic load.

For the analysis of borehole breakouts in Posidonia shale a total of six PS and two PN thick-walled cylinders were prepared perpendicular to the bedding. Special care was taken in specimen preparation to avoid the exposure of drilling fluids to the water sensitive Posidonia shale. Six specimens with 40 and 50 mm diameter and 80 mm length were drilled dry using compressed air as cooling medium for the diamond-studded core bit. The central borehole with diameters between 2.5 and 19 mm was also drilled dry with a solid carbide drill bit. Dust and small drill cuttings were immediately removed from the borehole by a high power vacuum cleaner. End surfaces were cut, grinded and ground parallel to each other within ±20 µm accuracy (e.g., Figure 3.1b). Two specimens with 10 mm diameter, 20 mm length, and 1 mm and 2.5 mm boreholes were fabricated dry using a digitally automated milling machine (CNC).

3.3.2 Mechanical Set-up

For determination of the uniaxial compressive strength (*UCS*) and Young's modulus (*E*) we used a 4600 kN servo-hydraulic loading frame (MTS 8600). Load was measured using an external load cell with an accuracy of ±1%. A series of uniaxial compressive tests on 12 solid specimens cored parallel and perpendicular to bedding was performed at a displacement rate of 0.2 mm/min in accordance with the ISRM Suggested Method for Determining the Uniaxial Compressive Strength and Deformability of Rock Material (Bieniawski and Bernede, 1979a; Bieniawski and Bernede, 1979b).

To induce breakouts in thick-walled cylinders we used two deformation apparatuses. For samples with borehole diameters ≥2.5 mm we equipped the MTS loading frame with an oil pressure vessel capable of applying 200 MPa confining pressure. A total of 6 specimens were jacketed using 2 mm thick rubber-sleeves to prevent penetration of the confining oil into the specimen. Each specimen was equipped with at least 12 sensors containing piezoceramic discs of 1 mm thickness and 5 mm diameter for measuring acoustic emissions (AE), ultrasonic velocities and amplitudes in radial and axial direction. The thickness and diameter-related resonant frequencies of the sensors are about 2 MHz. Transducer signals are amplified by 60 dB using Physical Acoustic Corporation (PAC) preamplifiers equipped with 100 kHz high-pass filters. AE waveforms and ultrasonic signals were stored in a 16 channel transient recording system (DAXBox, Prökel GmbH, Germany), with an amplitude resolution of 16 bit at 10 MHz sampling rate (Dresen et al., 2010). Sample strain in axial and circumferential direction was monitored by at least two pairs of orthogonally oriented strain-gages, glued on to the cylindrical surface of the rock with two component epoxy, and recorded with 2 Hz sampling rate in an 'HBM MGC Plus system' with an accuracy of ±3%. Hydrostatic pressure was increased at a rate of 1–2 MPa/min while the borehole was kept at atmospheric pressure. Unloading started 10–20 min after breakout initiation at a rate of 2–4 MPa/min.

For two smaller samples with boreholes ≤2.5 mm, potentially requiring high confining pressures in excess of those which could be applied by the MTS loading frame, a high-pressure gas apparatus (Paterson, 1970) capable of applying 500 MPa confining pressure was used. The specimens of 10 mm diameter and 20 mm length were isolated from the confining argon gas by copper jackets. The borehole was kept at atmospheric pressure. In these tests the onset of borehole breakouts was estimated by means of X-ray computer tomography (CT). Specimens were loaded in 25 MPa increments, unloaded and scanned at ambient conditions in an X-ray computer tomograph (GE Phoenix X-ray nanotom|s 180 NF). Acquisition parameters used were 100 kV, 40 mA and an exposure time of 250 ms allowing a fast scan of the specimen with a resolution of 22 µm per voxel. The loading rate in the high-pressure gas vessel is approximately 60 MPa/min up to 120–130 MPa, and 30 MPa/min at higher pressures. During this procedure, the specimen remains encapsulated in the copper jacket, allowing a non-destructive analysis of the breakout development in one and the same sample. To enhance the contrast between matrix and borehole, the borehole wall was coated with conductive silver paste.

3.3.3 Microstructural Analyses

Large samples with 40–50 mm diameter and borehole diameters ≥2.5 mm, were scanned in a CT after deformation with 130–140 kV, 40 mA using an exposure time of 500 ms. Depending on the sample diameter and magnification, the resolution varied between 11 and 32 µm per voxel. Based on CT observations thin-sections were prepared from each specimen perpendicular to the borehole axis. After optical inspection, the thin sections were additionally inspected and analyzed in a scanning electron microscope (Carl Zeiss SMT-Ultra 55 Plus) in backscattered and scanning electron mode. The thin sections were scanned automatically, using pre-defined functions and composed to large mosaics showing the complete borehole periphery.

3.4 Results

3.4.1 Uniaxial Compressive Strength and Young's Modulus

The uniaxial compressive strength and static Young's modulus, defined as the tangent of the stress–strain curve at 50% peak load, were measured in constant strain rate tests using the MTS loading frame (Table 3.2). Due to the low permeability (≈ 100 nD) of the tested shale and relatively high loading rates we expect undrained conditions also supported by optical inspection of samples after deformation. *UCS* is about 16–35% lower parallel than perpendicular to the lamination for PS and PN, respectively. *E* is almost twice higher parallel to bedding compared to bedding-normal direction. This is due to compaction of high aspect ratio voids and soft components like clays and organic matter when loaded perpendicular to the bedding. However, when loaded parallel to the bedding the stiff minerals, e.g., calcite, quartz or pyrite, form a load-bearing framework (Figure 3.1c). *E* and *UCS* of PS are much smaller than for PN for both orientations. This may likely be due to a significantly larger porosity of PS (Table 3.1). The results of the uniaxial compression experiments indicate that Posidonia shale has a high strength and elastic deformation anisotropy. The strength and deformation parameters are assumed to be similar parallel to the bedding (x–y direction) but to differ across them (z direction) as frequently observed in oil shale (Chong and Smith, 1984). Hence, we assume transverse isotropic material behavior for the tested Posidonia shale.

Table 3.2 Young's moduli and uniaxial compressive strength data for PN and PS.

Property	PS	PN
E_z [GPa]	5±0.5	10.4±0.3
E_{xy} [GPa]	9.4±0.9	17.3±4.0
UCS_z [MPa]	80±8	114±6
UCS_{xy} [MPa]	67±7	75±10

3.4.2 Compaction Behavior of a Solid Cylinder

One solid specimen (PS8) was loaded hydrostatically up to 195 MPa in order to compare the elastic parameters of intact samples to thick-walled cylinders and to study the compaction behavior of PS at elevated hydrostatic pressures.

At 2 MPa hydrostatic pressure ultrasonic velocities range from v_z =2.71±0.1 km s^{-1} perpendicular to bedding to v_r = 4.54±0.07 km s^{-1} parallel to bedding. During loading the velocities increase by 25% perpendicular and by 13% parallel to the bedding at 195 MPa, respectively (Figure 3.2a). The initial increase of v_z is likely due to non-linear axial compaction (e_z, Figure 3.2b), related to the closing of voids and compaction of clays and organic matter particles. Circumferential compaction, e_{circ}, is less than e_z and almost linear during loading (Figure 3.2b). The velocity anisotropy, v_a, may be expressed as

$$v_a = \left(\frac{v_r - v_z}{v_r} \right) \qquad 3.4$$

The velocity anisotropy versus hydrostatic pressure is plotted in Figure 3.2a. According to Schon (2004), v_a can be differentiated into crack and texture related anisotropy. It is suggested, that the crack related anisotropy is overcome as the ultrasonic anisotropy curve is changing from an exponential to a linear decay with increasing confinement. At this pressure, the majority of high aspect ratio pores and microcracks are assumed to be closed. For PS8 this is achieved at a crack closure pressure, $P_{closure}$, of approximately 130 MPa (Figure 3.2a). The remaining velocity anisotropy at pressures exceeding $P_{closure}$ in shales is mainly caused by orientation distribution of minerals and kerogen content (Dewhurst and Siggins, 2006; Johnston and Christensen, 1995; Vernik et al., 1997; Wenk et al., 2008).

The bulk modulus (C_{bulk}) is given by

$$C_{bulk} = \frac{\Delta P}{\Delta e_z + 2\Delta e_{circ}} \tag{3.5}$$

where ΔP is the change in confining pressure, and Δe_z and Δe_{circ} are the change in axial and circumferential strain, respectively. C_{bulk} yields a minimum of ~7 GPa at approximately 40 MPa and a constant value of 8.8 ± 0.1 GPa at pressures exceeding 130 MPa ($P_{closure}$) (Figure 3.2b). Beyond $P_{closure}$ PS shows a linear compaction behavior.

The bulk modulus was also estimated using mercury injection porosimetry (MIP). Assuming that at $P_{closure}$ all microcracks and pores are closed and the sample deforms homogeneously the injected volume of mercury indicates the volumetric compaction of the specimen. The mercury intrusion curve then allows estimating a bulk modulus, C_{MIP}, at pressures exceeding $P_{closure}$ (linear slope in Figure 3.2c). C_{MIP} is given by

$$C_{MIP} = V \frac{\Delta P}{\Delta V_{Hg}} \tag{3.6}$$

where V is the volume of the rock given by the sample mass divided by the apparent density, ΔP is the change in pressure and ΔV_{Hg} is the injected volume of mercury. C_{MIP} for PS at pressure >130 MPa yields 8.4 ± 0.4 GPa and is in good agreement with C_{bulk}. Estimating C_{MIP} for PN specimens yields 11.6 ± 0.5 GPa.

Up to a confining pressure of 195 MPa the solid specimen did not show a distinct reduction in volume or a surge of AE activity typical for grain crushing or pore collapse in sandstones (Cuss et al., 2003; Klein et al., 2001; Zhang et al., 1990). This suggests that large-aspect ratio pores in Posidonia shale are progressively closed with increasing confining pressure.

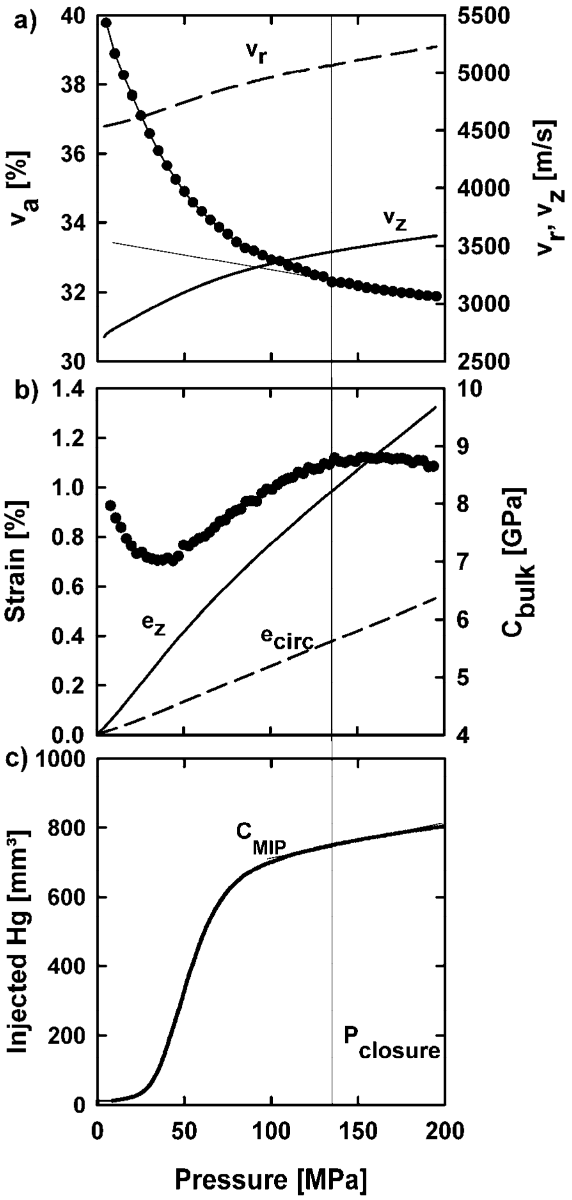

Figure 3.2 Compaction behavior of PS sample under increasing hydrostatic pressure. a) Velocity parallel (v_r) and perpendicular (v_z) to bedding increases non-linearly with increase of pressure, resulting in a decreasing velocity anisotropy (v_a). b) Variation of circumferential (e_{circ}) strain, axial (e_z) strain and associated compression bulk modulus (C_{bulk}) with pressure. c) Mercury injection curve, allowing to derive a bulk modulus (C_{MIP}) for the linear part at $P > P_{closure}$.

3.4.3 Borehole Breakouts in Thick-Walled Cylinders

A total of six PS and two PN thick-walled cylinders have been tested under hydrostatic compression (Table 3.3). The following sections describe how we determined the onset of borehole breakout initiation by means of strain, AE activity, nondestructive CT analysis, P-wave velocities and amplitudes.

Table 3.3 Sample dimensions and critical confining pressure *P**.

Sample Name	l [mm]	b [mm]	a [mm]	b/a [1]	P^*_{strain} [MPa]	P^*_{Cbulk} [MPa]	P^*_{vp} [MPa]	P^*_{amp} [MPa]	P^*_{AE} [MPa]	P^*_{CT} [MPa]	P^*_{avg} [MPa]	σ_{Θ}/UCS_z [1]
PS1*	20	10	1	10	-	-	-	-	-	275 -25	275 -25	6.94
PS3*	20	10	2.5	4	-	-	-	-	-	175 -25	175 -25	4.67
PS4	80	50	2.5	20	169.0	169.5	-	163.5	-	-	167.3 ±5.2	4.19
PS5	80	50	8	6.25	122.1	116.0	-	-	125	-	121.0 ±6.3	3.10
PS6	80	50	10	5	115.3	115.3	114.5	118.1	121	-	115.6 ±9.5	3.01
PS7	80	50	19	2.63	88.4	87.31	88.8	92.3	87	-	88.8 ±3.0	2.59
PS8	80	40	0	-	-	-	-	-	-	-	-	--
PN1	80	40	6	6.67	159.0	158.0	159.7	170.4	138	-	157.0 ±10.0	2.82
PN2	80	50	10	5	144.7	142.5	144.1	-	130	-	140.3 ±3.4	2.56

* Samples tested in high pressure gas apparatus. '–' could not be measured. l is length, b is specimen diameter, a is borehole diameter.

3.4.3.1 Circumferential Strain and Breakout Nucleation

Similar to the compaction behavior of a solid sample, thick-walled cylinders are most compressible normal to bedding. Axial strain, e_z, is significantly larger than circumferential strain, e_{circ}, as shown in

Figure 3.3a and b, respectively. However, circumferential strain indicates the onset of breakout development (Dresen et al., 2010). Hence, we derive the hydrostatic pressure with respect to the circumferential strain by $\Delta P/\Delta e_{circ}$. The deduced values are plotted versus confining pressure in

Figure 3.3c. The graphs are expected to depend on the ratio of the outer to inner diameter, b/a, and on confining pressure P_o and are expected to coincide for constant b/a before failure (Papamichos, 2010; Papamichos and van den Hoek, 1995). With a decreasing ratio of b/a, the response of the thick-walled cylinder softens whereas for increasing b/a, it converges to the response of a solid cylinder.

With increasing hydrostatic confining pressure the ratio $\Delta P/\ \Delta e_{circ}$ first decreases due to non-linear compaction and settlement of the strain gages. Afterwards, it approaches a nearly constant value, indicating linear elastic behavior, that suddenly decreases above a critical pressure *P**, indicating non-linear deformation of the thick-walled cylinder. We assume that this critical pressure denotes the onset of borehole breakout formation.

The post breakout behavior is dominated by a continuously decreasing ratio $\Delta P/\Delta e_{circ}$ with increasing pressure, related to the growth of breakouts.

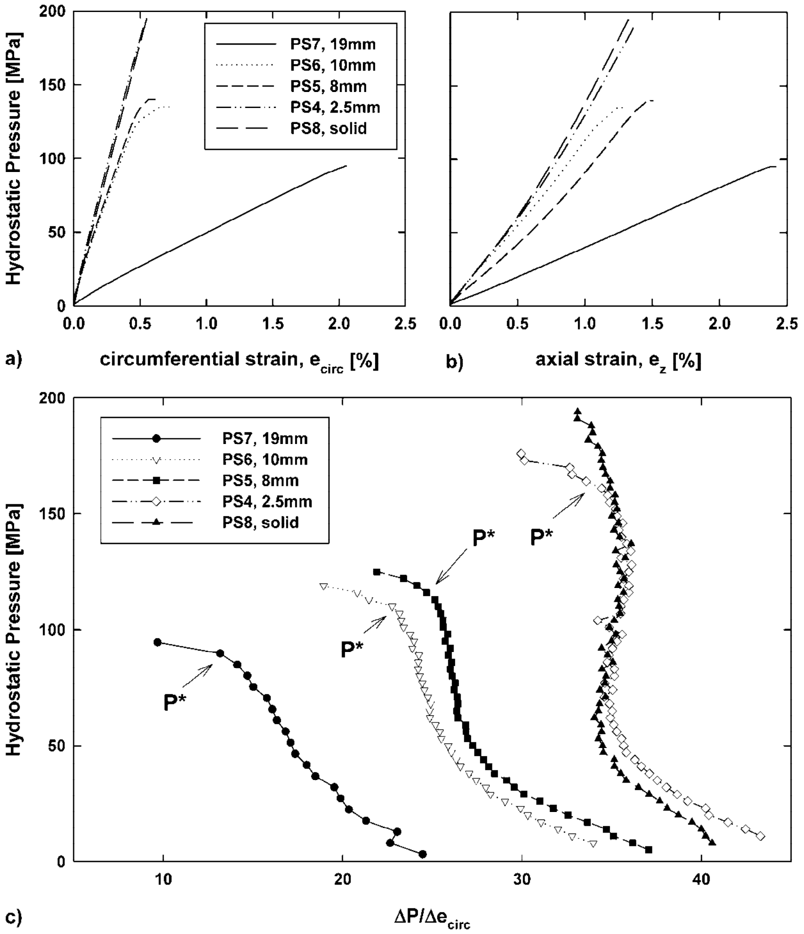

Figure 3.3 a), b) show circumferential and axial strain versus hydrostatic pressure. c) Derivative of the hydrostatic pressure with respect to the circumferential strain plotted against increasing hydrostatic pressure for PS specimens with different borehole diameters. The critical breakout pressure *P** coincides with distinct reduction of the circumferential modulus (marked by arrows).

3.4.3.2 Ultrasonic P-wave Velocities and Amplitudes

Ultrasonic P-wave velocities and amplitudes increase during loading of the samples as shown for PS6 in Figure 3.4. Prior to the onset of borehole breakout formation at pressure *P**, the P-wave velocities and amplitudes measured in radial direction reach a maximum. Typically, P-wave velocities and amplitudes along traces across the middle part of the sample are first affected by crack damage associated with breakout nucleation (z = 40 mm, Figure 3.4). Breakouts progressively grow in radial and z-direction toward both ends of the specimens with increasing pressure successively affecting different ray traces (z = 10/65 mm).

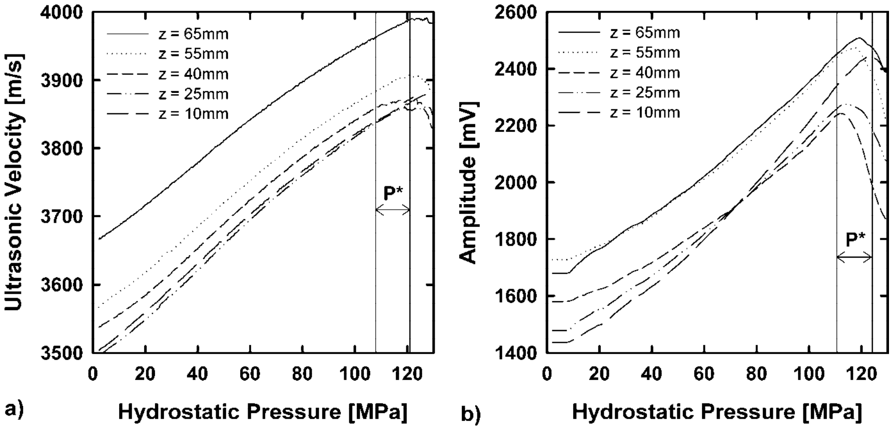

Figure 3.4 a) Change of radial ultrasonic velocities and b) amplitudes with increasing pressure, measured at different heights *z* along the sample axis of PS6. The expected range of breakout formation pressures *P** is indicated by vertical lines.

3.4.3.3 AE Activity and Localization

AE activity indicates damage of the specimen by microcracking under load. Generally, the number of AE events increases with increasing pressure in the tested Posidonia shale samples. For specimens with similar borehole diameter the AE activity is higher in PN compared to PS samples, although the number of recorded AE events is relatively low compared to more brittle rocks like for example sandstone (Dresen et al., 2010; Papamichos et al., 2010).

Acoustic emissions are located around the borehole, but are too few to precisely identify breakout orientation or growth. For example,

Figure 3.5 displays all located AEs throughout the complete loading of PS6. The localization error is probably greater than ±2 mm for the transverse isotropic Posidonia shale, since we used an isotropic velocity model. However, a distinct increase or jump in AE activity could still be monitored and was used to determine the onset of breakout nucleation. The value of *P** determined by AE activity yields values in agreement to the values determined by strain measurements, ultrasonic velocities or amplitudes.

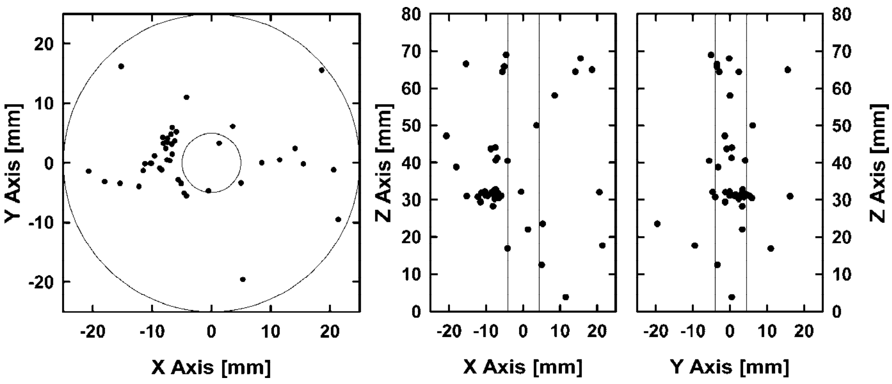

Figure 3.5 Acoustic emission (AE) hypocenters (black dots) are located mainly close to the borehole in specimen PS6. Borehole diameter is 10 mm. Location error is estimated to be > ±2 mm.

3.4.3.4 X-ray CT Observations

Non-destructive X-ray CT scanning of specimens loaded to failure in 25 MPa steps was used to monitor the deformation of samples with boreholes ≤2.5 mm, allowing to bracket the critical pressure for the onset of breakout formation. Figure 3.6 depicts breakout evolution in sample PS3 with a 2.5 mm borehole loaded in 25 MPa steps to a maximum pressure of 250 MPa. Each scan was performed at ambient pressure conditions. Damage first occurs near the top end of the hole at 150 MPa, probably due to end cap friction effects or buckling of the conductive silver paste as the specimen shortens. The pressure *P** at the onset of breakout formation is about 175 MPa, verified by the development of cracks in the circumference of the bore. As pressure increases the damage becomes more pervasive along the entire borehole axis. In top view (A–A' in Figure 3.6) the development of symmetric spiral-shaped cracks is revealed. One single spiral crack can surround almost half the borehole periphery. The number of spiral cracks increases with increasing confining pressure. Fragments rotate toward the free surface and reduce the effective bore diameter until the borehole is nearly collapsed at maximum applied pressure of 250 MPa.

Note that the geometrical resolution of the X-ray CT scans is 22 μm in this example. Hence, it is not possible to see potential cracks below this resolution and the breakout initiation may have occurred at slightly lower pressures. Furthermore, loading rate varied significantly from larger specimens and continuous loading-unloading cycles close to failure may affect the results. However, comparison of *P** based on strain, ultrasonic and AE measurements (PS4) and *P** determined by CT (PS3) shows excellent agreement within approximately 5%.

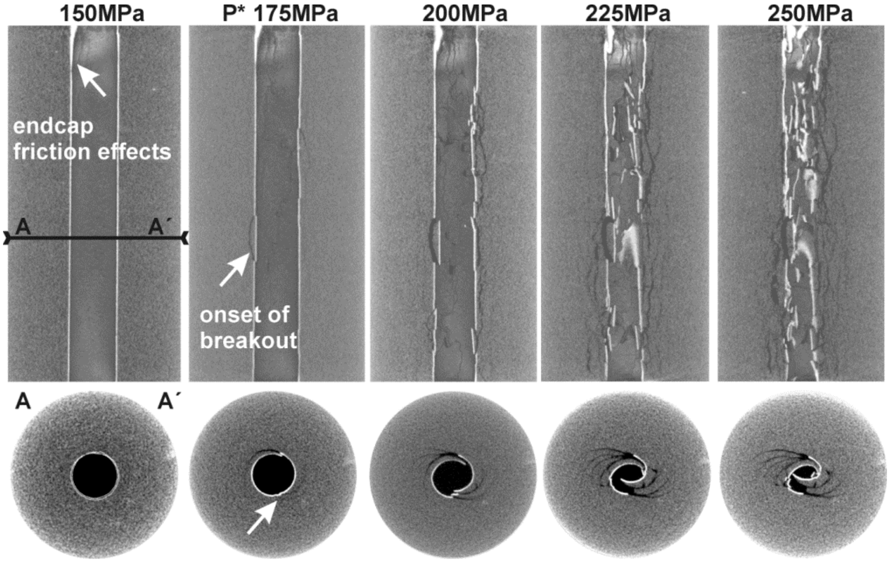

Figure 3.6 X-ray CT scans of sample PS3 loaded step wise from 150 MPa (left) to 250 MPa (right) hydrostastic pressure. Sample is viewed across the borehole axis (top) and in top view along A–A' (bottom). The critical pressure at the onset of breakout formation, *P**, is about 175 MPa. The bright color at the borehole wall results from lubrication with conductive silver paste.

3.4.3.5 Microstructural Analysis

Thin sections of each specimen were prepared perpendicular to the borehole axis and analyzed using SEM (Figure 3.7). The borehole breakouts are characterized by the development of shear dominated fracture sets. Fractures initiated at several points along the borehole wall (Figure 3.7a) and propagated mainly in the calcareous cement and along weak clays bypassing rigid quartz or large calcite grains, sometimes detaching the grains from the cement without damaging them (Figure 3.7b). As the fractures propagate, they span an angle of approximately 35±5° between fracture trace and the borehole wall. This angle continuously decreases with increasing distance from the borehole until the fracture turns into an almost borehole tangential direction (±15°) at approximately twice (1.7–2.5) the borehole radius. Most of the fractures showed a significant sliding as the fragments are pushed toward the empty borehole. Especially small boreholes are strongly distorted on the sides where the fractures initiated (Figure 3.7c).

Once a shear fracture formed on one side of the borehole, it caused another fracture to appear on the opposed side, leaving pronounced symmetry of conjugated shear fractures with regard to the borehole axis. This symmetry affects breakout depths, number of fractures, and their orientation and is more pronounced in small boreholes. As the borehole diameter increases the fracture patterns are less symmetric (compare Figure 3.7a and c).

With increasing hydrostatic pressure the already broken segments between the fractures rotated toward the borehole, occasionally forming tensile cracks at the end of the shear fracture pointing toward the borehole (Figure 3.7a). Due to the very fine grain size and slip along the crack planes (Figure 3.7d), the surface of the crescent-shaped fragments is smooth.

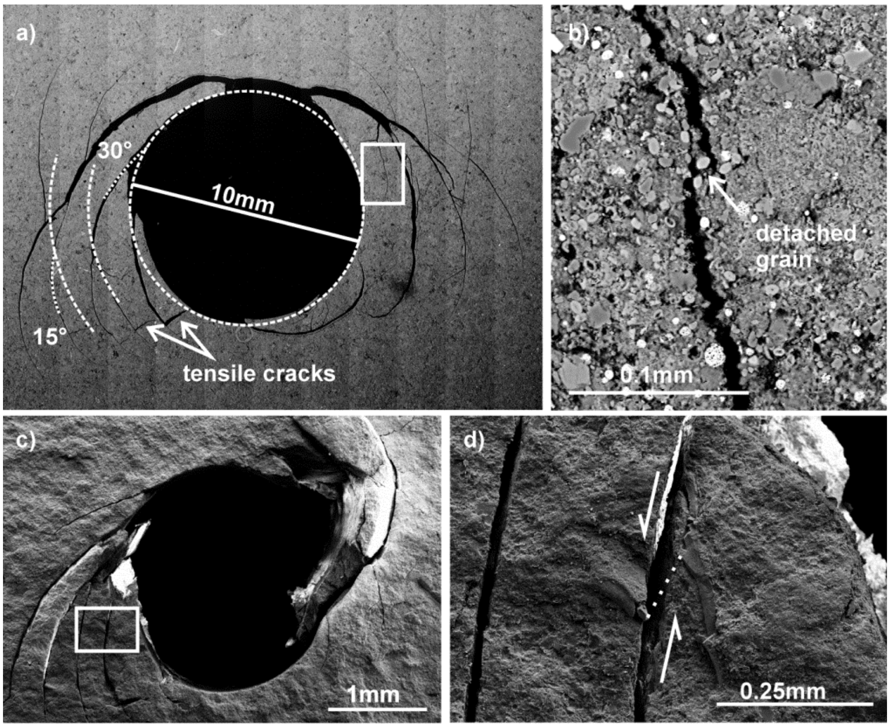

Figure 3.7 SEM images showing shear dominated breakout fracture pattern. a) Breakouts in sample PS6 with a 10 mm borehole show several fracture initiation points along the borehole wall. b) Detail of secondary crack propagation (magnified area marked by the rectangle in a). c) Point-symmetric breakout pattern around a 2.5 mm borehole (sample PS3). d) Slip along a crack plane indicated by the offset of adjacent grains (magnified area marked by the rectangle in c)).

3.4.3.6 Influence of Borehole Diameter on Breakout Pressures

We determined the onset of borehole breakout development for samples in the MTS loading frame using strain measurements, ultrasonic velocities and amplitudes, and AE activity as described above. The critical pressure *P** at breakout nucleation (Table 3.3) represents an average value from these measurements. For samples PS1 and PS3 tested in the high-pressure gas apparatus, an upper limit of *P** was estimated from non-destructive X-ray CT. It was found that *P** increases significantly with decreasing borehole diameter for PS and PN samples (Figure 3.8). Typically, PN samples require higher critical hydrostatic confining pressures to initiate breakouts at similar borehole diameters compared to PS samples, possibly related to a higher strength of the material (compare *UCS* in Table 3.2).

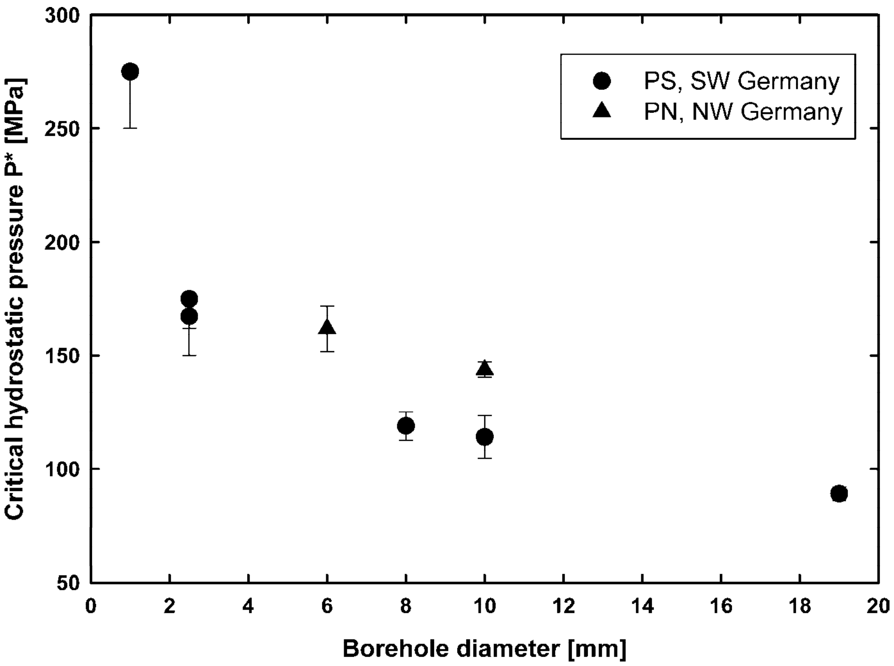

Figure 3.8 Reduction of the critical hydrostatic pressure *P** for borehole breakout initiation with increasing borehole diameter of PS and PN samples.

3.5 Discussion

3.5.1 Comparison to Sandstone Data and Application of Failure Criteria

The critical pressure *P** for borehole breakout initiation in Posidonia shale decreases asymptotically from 275 MPa for specimens with a 1 mm borehole to ~89 MPa for samples containing a 19 mm borehole (Figure 3.8). The values of *P**, converted to a critical tangential stress at the borehole wall based on Equation 3.1, and normalized with the uniaxial compressive strength (UCS_z), are plotted versus the borehole diameter in Figure 3.9. The experimental results for PS and PN show a similar trend of decreasing *P** with increasing borehole diameter. A similar trend is observed for various sandstones with different porosity and mineralogical composition. For large borehole diameters (4-10 mm) the normalized critical stress approximates a ratio of 2, whereas for small borehole diameters it seems to approach the grain crushing/pore collapse pressure reported for sandstones (rectangle indicated in Figure 3.9; (Cuss et al., 2003; Klein et al., 2001; Zhang et al., 1990).

Figure 3.9 includes data from scaled (constant *b/a*) and non-scaled specimens. Ideally, the specimen geometry should have a constant *b/a* ratio to study the scale-effect (van den Hoek et al., 1992; van den Hoek et al., 1994; Papamichos and van den Hoek, 1995) as it might be expected that the observed scale effect depends not only on borehole diameter *a*, but also on the ratio *b/a*. However, the figure indicates that the scale-effect was observed for scaled and non-scaled geometries. In addition, our measurements do not show a dependence of P^* on the b/a ratio. For example, samples PS3 and PS4 with b/a=4 and 20, respectively, failed at almost similar pressures of 170–175 MPa (Table 3.3). Furthermore, assuming that P^* depends linearly on b/a, extrapolation of the data obtained for large diameter samples (b=50 mm) predicts P^* = 291 MPa for a 1 mm borehole in a large sample (b/a=50), which is in good agreement with P^* of 275 MPa determined for (b/a=10), i.e., a 1 mm borehole in a 10 mm diameter specimen. It can be concluded, in agreement with bifurcation theory (Papamichos, 2010; Papamichos and van den Hoek, 1995; Papanastasiou and Vardoulakis, 1992), that the observed scale-effect is not a primary result of scaled or non-scaled specimens but of the hole diameter. Assuming that breakouts nucleate at the borehole wall or at some distance Δr= $(r - a)$, we apply four different failure criteria to model breakout formation in Posidonia shale. Here, we replace the stresses S_1, S_2 and S_3 with the borehole relevant stresses σ_Θ, σ_v and σ_r, respectively (see Equation 3.1 and 3.3), and solve for the critical hydrostatic pressure, P^*.

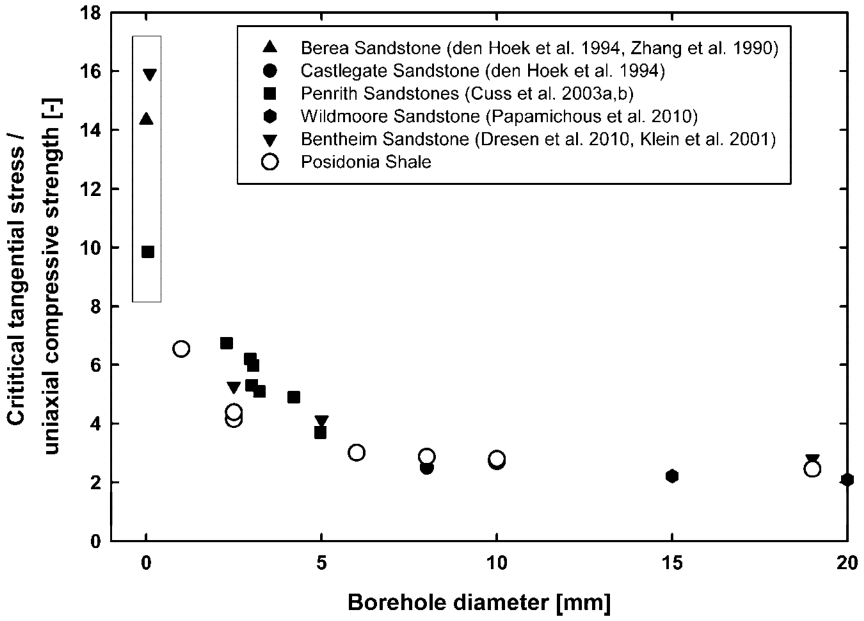

Figure 3.9 UCS-normalized critical tangential stress at the borehole wall for breakout nucleation versus borehole diameter, showing a strong non-linear increase for small boreholes independent of rock type.

The Mohr–Coulomb criterion (Zoback, 2007), expressed in principal stresses is given by

$$S_1 = UCS + S_3\left(\sqrt{(1+\mu^2)}+\mu\right)^2 \qquad 3.7$$

where μ is the friction coefficient and UCS is the uniaxial compressive strength of the material. Replacing S_1 and S_3 by σ_Θ, and σ_r, respectively, and solving for P^*, yields

$$P^{*} = \frac{UCS}{\frac{b^2}{b^2-a^2}\left(1+\frac{a^2}{r^2}-\left(\sqrt{(1+\mu^2)}-\mu\right)^2+\left(\sqrt{(1+\mu^2)}+\mu\right)^2\frac{a^2}{r^2}\right)} \qquad 3.8$$

Best fit to the data using UCS = 80 MPa (Table 3.1) and $\mu \approx 0.4$ (pers. comm. M. Makasi) is achieved for a fixed distance $\Delta r = (r{-}a)$ of 150–200 μm from the borehole wall. However, P^* is largely underestimated by a factor of about 2 (Figure 3.10, short dashed line).

Similar to the Mohr–Coulomb criterion, the failure model of McClintock and Walsh (1962) underestimates the strength of the thick-walled cylinder by the same amount (dotted line in Figure 3.10). This criterion is given by Jaeger et al. (2007)

$$S_1\left(\sqrt{(1+\mu^2)}-\mu\right)^2 - S_3\left(\sqrt{(1+\mu^2)}+\mu\right)^2 = 4S_t\left(\sqrt{\frac{1+P_{closure}}{S_t}}-2\mu_i P_{closure}\right) \qquad 3.9$$

where S_t is the tensile strength of the material and μ_i is the friction coefficient of closed cracks at pressure exceeding $P_{closure}$. Substitution yields

$$P^{*} = \frac{4S_t\left(\sqrt{\frac{1+P_{closure}}{S_t}}-2\mu_i P_{closure}\right)}{\frac{b^2}{b^2-a^2}\left(\left(1+\frac{a^2}{r^2}\right)\left(\sqrt{(1+\mu^2)}-\mu\right)^2-\left(1-\frac{a^2}{r^2}\right)\left(\sqrt{(1+\mu^2)}+\mu\right)^2\right)} \qquad 3.10$$

For the calculation we assumed a tensile strength $S_t \approx 8$ MPa (1/10 of UCS) and $\mu = 0.4$. $P_{closure}$ is estimated from the hydrostat measured on the solid cylinder to be about 130 MPa. A best fit to the experimental data is found for Δr of 150–200 μm. A third failure criterion based on the Griffith criterion, which takes into account the influence of the intermediate (vertical) stress, σ_v, is the Griffith–Murrell criterion (Hoskins, 1969; Fjaer et al., 2008, p. 71), given by

$$\left(S_1-S_2\right)^2+\left(S_2-S_3\right)^2+\left(S_3-S_2\right)^2=24S_t\left(S_1+S_2+S_3\right) \qquad 3.11$$

This criterion predicts a critical hydrostatic pressure of

$$P^{*} = \frac{72S_t}{\left(\frac{b^2}{b^2-a^2}\left(1+\frac{a^2}{r^2}\right)-1\right)^2+\left(1+\frac{b^2}{b^2-a^2}\left(1+\frac{a^2}{r^2}\right)\right)^2+4\frac{b^2}{b^2-a^2}\frac{a^2}{r^2}} \qquad 3.12$$

The Griffith–Murrell criterion predicts failure in good agreement with the data (Figure 3.10, solid line), again for Δr = 150 μm. This suggests that the intermediate stress affects the formation of breakouts in thick-walled Posidonia shale cylinders as opposed to previous studies (Addis and Wu, 1993; Addis et al., 1990; Charles, 1997).

Dresen et al. (2010) proposed a model, based on a linear fracture initiation criterion suggested by Ashby and Hallam (1986), to predict the critical pressure for breakout formation observed in porous Bentheim sandstone. For a cylindrical sample, the critical pressure P^* is given as

$$P^* = \frac{\frac{\sqrt{3}}{(1+\mu^2)^{1/2}-\mu}\frac{K_{IC}}{\sqrt{\pi c}}}{\frac{b^2}{b^2-a^2}\left(1+\frac{a^2}{r^2}\right)-\frac{b^2}{b^2-a^2}\left(1-\frac{a^2}{r^2}\right)\frac{(1+\mu^2)^{1/2}+\mu}{(1+\mu^2)^{1/2}-\mu}} \qquad 3.13$$

where c is half the initial defect size, μ is the internal friction coefficient and K_{IC} is the mode I fracture toughness. Fracture toughness of PS samples was measured yielding $K_{IC} \approx 1.14$ MPa√m. We assume that the largest pore radius of ≈ 50–100 μm measured by MIP represents the typical initial defect size (dashed-dotted line in Figure 3.10). It should be noted, however, that the estimation of the initial defect (pores or microcracks) size of shales is difficult with a possible large bias (Keller et al., 2011). The best fit to the experimental data suggests a half crack length, c, of 45 μm, which represents the largest pore diameter measured by MIP (Figure 3.10, full triangles). The data shows a best fit for Δr =150 μm.

Interestingly, all applied models require a depth (Δr) of about 150 μm to best fit the trend of the critical hydrostatic pressure, P^*, versus borehole radius given in Figure 3.10. We interpret this depth to represent the width of a process zone around the borehole, which is likely associated with compaction and redistribution of soft particles, pore collapse, grain boundary sliding and most probably the initiation of microcracks. However, it is conceivable that collapse of submicron pores or possibly redistribution of organic matter remain undetected in SEM possibly related to the preparation of polished thin-sections. Also, breakout growth will obscure initial damage related to breakout formation.

Plasticity would shift the maximum of the tangential stress concentration from the borehole wall into the rock. Hence, crack initiation would occur at some distance Δr away from the borehole wall as for example observed in Gebdykes dolomite (Santarelli and Brown, 1989). Calculation of the extend of such plastic regions based on different failure criteria (e.g., Tresca (Charles, 1997), Mohr–Coulomb (Hoek, 1999) or Hoek–Brown (Carranza-Torres and Fairhust, 1999)) around the borehole scale with the borehole radius r but significantly exceed Δr =150 μm. It is interesting to note that for high porous Bentheim sandstone (Dresen et al., 2010) showed that their model is in good agreement to their experimental data for Δr between 100–300 μm. Even though, Bentheim sandstone and Posidonia shale vary significantly in composition as well as pore and grain size, the range of depth Δr is very close. For Posidonia shale we were not able to determine the thickness of a process zone for the reasons mentioned previously. SEM images indicate that due to the laminated structure of the material larger features, i.e., stringers of organic matter or elongated calcareous minerals, of the length $\Delta r > 100$ µm exist in Posidonia shale (see Figure 3.1c).

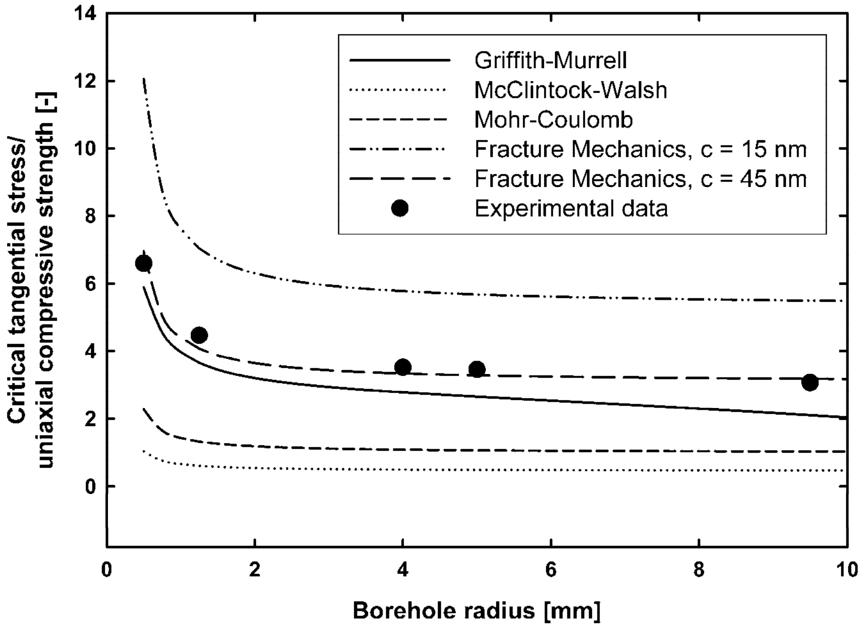

Figure 3.10 Modeling of scale-effect by application of different failure criteria. Model parameters are given in the text. Note, that the critical hydrostatic pressure is calculated at $\Delta r = 150$ µm.

3.5.2 Shear Fracture Propagation

Shear fractures form at an initial stage of breakout development and control the breakout shape in Posidonia shale. An analytical model for fracture propagation around a hydrostatically loaded borehole was proposed in Fjaer et al. (2008). Assuming Mohr–Coulomb failure Fjaer et al. (2008) derived the relation:

$$r = C_1 \exp\left(\left(\sqrt{\mu^2 + 1} - \mu\right)\theta\right) \tag{3.14}$$

where C_1 is a constant, r is the distance from borehole axis, and Θ is the azimuth angle. Due to the symmetric loading conditions the calculated failure plane can be placed all around the borehole. Figure 3.11a shows the influence of the friction coefficient on the predicted failure planes. The breakout pattern around a borehole with 1 mm diameter is compared to a predicted fracture trace using $\mu = 0.4$ (Figure 3.11b). Close to the borehole where the shear fractures initiated we observe a good agreement. With increasing distance from the borehole, there is some misfit between the experimentally observed fracture trace and the predicted failure planes (dashed-dotted lines in Figure 3.11b). The misfit is likely caused by relative slip and rotation of broken segments, disturbing the local stress field (Figure 3.7). The dotted circle in Figure 3.11b is drawn at a distance of 2*a*, i.e., twice the borehole diameter. At this distance, the fractures seem to be in an unfavorable position for further growth at the applied critical hydrostatic pressure, *P**.

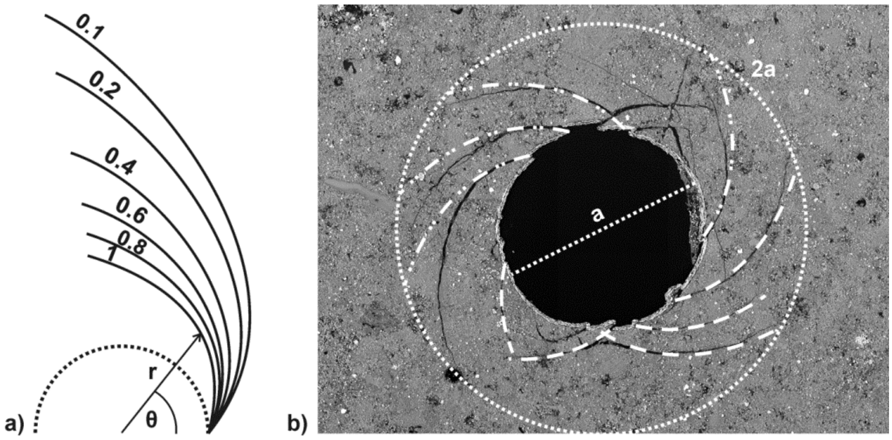

Figure 3.11 Comparison between calculated potential shear planes and experimental observations around a hydrostatically loaded sample with 1 mm borehole. a) Influence of the friction coefficient, $\mu = 0.1-1$, on the shape of shear planes. b) For $\mu = 0.4$ short fractures agree well with calculated shape (dashed lines). Long fractures with larger displacements at the borehole wall show a considerable misfit at large distance from the borehole wall (dashed-dotted lines). Dotted circle indicates maximum extend of fractures.

3.5.3 Breakout Development

Irrespective of different material and failure characteristics for different porous rocks a similar decrease in critical pressure for breakout initiation with increasing borehole diameter is observed. In Posidonia shale the applied stresses distribute between soft cements and stiff minerals. Local defects at the borehole wall presumably induce initiation of multiple shear fractures (Figure 3.7 and Figure 3.11). In contrast, in porous, well-cemented sandstones, where the stresses are mainly transferred at grain-to-grain contacts, intragranular cracks accumulate at the initial stage of breakout development forming slot-like breakouts (Dresen et al., 2010; van den Hoek et al., 1994). However, borehole breakout development in weakly cemented sandstone and limestone also occurs predominantly by shear failure propagation (Cuss, 2003; Papamichos et al., 2010; van den Hoek et al., 1992; Hoskins, 1969). This behavior is similar to that of black shale, where intergranular, shear-dominated cracking in the weak matrix prevails (Figure 3.7b). The spiral-like breakout patterns in Posidonia shale resemble closely that observed in a limestone tested by Guenot (1989) and partly those observed in Cordova Cream limestone (Haimson and Song, 1993) and Gebdykes dolomite (Santarelli and Brown, 1989). For the tested Posidonia shale, the breakout shape is symmetric with regard to the borehole axis, in particular in samples with small boreholes as indicated by Maury and Sauzay (1987) for isotropic loading conditions and zero borehole pressures. Breakout depth equals approximately the borehole radius close to *P** (Figure 3.11b), implying an increasing breakout depth with increasing borehole diameter. This explains the collapse of sample PS7 with a 19 mm diameter borehole at pressures beyond *P**, where just a few mm of intact material remained between the breakout tip and the circumferential surface. The assumed borehole breakout development is shown schematically in Figure 3.12. Initially, due to specimen preparation some microcracks at maximum depth of 50 μm are present (Figure 3.12a). The orientation of these microcracks is sub-parallel to the borehole wall. This drilling induced damage is homogeneously spread along the complete borehole. Upon reaching *P**, shear dominated fractures initiate close to the borehole wall from a process zone of about 150 μm width and propagate into the rock (Figure 3.12b). In case conjugated fractures intersect, cross vault structures of fractures form at elevated pressure, inducing partial borehole enlargement (Figure 3.12c). The associated disturbance of the local stress field initiates new shear fractures in front of the breakout tip. Rotation of broken fragments toward the borehole wall initiates tensile cracks (Figure 3.12d), which limit the breakout width. Finally, dog-ear type breakouts form by continuous intersection of shear fractures extending the breakout to a depth approximately similar to the initial borehole radius (Figure 3.12e).

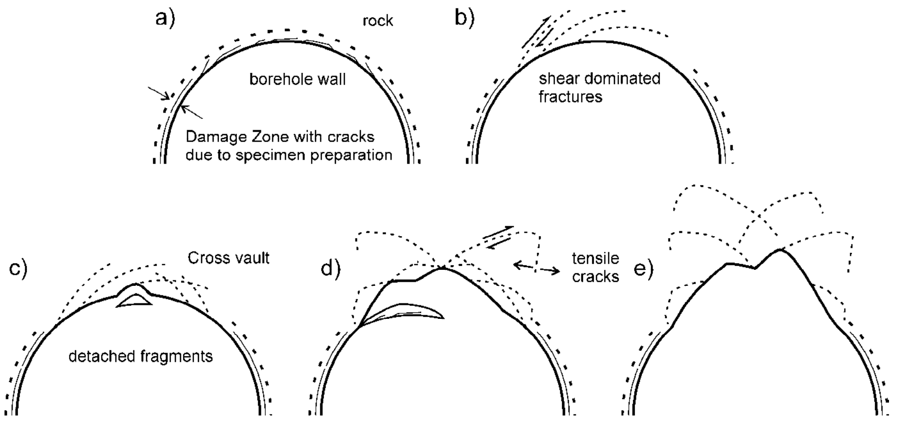

Figure 3.12 Sketch showing the development of borehole breakouts in Posidonia shale with increasing confining pressure a) Initial stage with sub-parallel cracks in the circumference of the borehole induced by specimen preparation. b) Shear fractures initiate at *P** and propagate into the rock. The shape is determined by the internal friction coefficient. c) Cross vaults form by intersection of conjugated fractures. d), e) Breakout growth by rotation of broken fragments that initiate tensile cracks limiting the final breakout width.

3.6 Conclusions

In this experimental study on thick-walled Posidonia shale samples we showed that failure around hydrostatically loaded boreholes is shear-dominated with a well-developed point-symmetry in particular for small boreholes. The observed breakout patterns are similar to limestone (Guenot, 1989; Haimson and Song, 1993). The shape of failure planes can be predicted assuming Mohr–Coulomb failure behavior as long as no displacement along the fractures occurs.

The critical pressure for initiation of borehole breakout reduces strongly with decreasing borehole diameter below about 10 mm. The tested Posidonia shale shows a similar scale effect as sandstone, when normalized to the *UCS*. Assuming a depth (Δr) of ≈ 150 μm for fracture initiation, the application of common failure criteria may explain the observed scale effect. The best fit in accordance with measured mechanical properties is predicted by either the Griffith–Murrell criterion highlighting the influence of the intermediate stress or the fracture mechanics model proposed by Dresen et al. (2010).

ACKNOWLEDGMENTS

We would like to thank an anonymous reviewer and the editor for their helpful comments on an earlier version of this manuscript. Furthermore, we would like to thank Stefan Gehrmann and Matthias Kreplin for their excellent work in specimen and thin section preparation, Michael Naumann for the support and handling of the high-pressure gas apparatus, and Manfred Jaeger from Holcim AG for supply of sample material. Additional thanks to Ilona Shäpan for running the SEM and Luiz Morales for the FIB analysis. Masline Makasi is acknowledged for fruitful discussions and provision of triaxial strength data. This research was supported by the GeoEn Project of the Federal Ministry of Education and Research in Germany.

4 INFLUENCE OF BEDDING ANGLE ON BOREHOLE STABILITY: A LABORATORY INVESTIGATION OF TRANSVERSE ISOTROPIC OIL SHALE[3]

SUMMARY

The stability of wells drilled into bedded formations, e.g., shales, depends on the orientation between the bedding and the borehole axis. If the borehole is drilled sub-parallel to bedding, the risk of borehole instabilities increases significantly. In this study, we examined the formation of stress-induced borehole breakouts in Posidonia shale by performing a series of thick-walled hollow cylinder experiments with varying orientations of the bedding plane with respect to the borehole axis. The thick-walled hollow cylinders (40 mm in diameter and 80 mm in length containing an 8 mm diameter borehole) were loaded isostatically until formation of breakouts. The onset of borehole breakout development was determined by means of acoustic emission activity, strain measurements, ultrasonic velocities and amplitudes. The critical pressure for breakout initiation decreased from 151 MPa by approximately 65% as the bedding plane inclination changed from normal to parallel to the borehole axis. The finely bedded structure in the shale resulted in an anisotropy in elasticity and strength from which the variation in strength dominated the integrity of the thick-walled hollow cylinders.

4.1 Introduction

An increasing number of wells are being drilled into shale formations because 75 % of all sedimentary basins worldwide contain shale formations (Pei, 2008), where shales form the cap rock of conventional oil- and gas reservoirs or in stratigraphic units used for CO_2 sequestration. More recently, exploitation of shale formations is strongly growing since they are important unconventional oil and gas reservoirs (e.g., Allix et al., 2006; Boyer et al., 2006). Furthermore, shale formations are also potential host rocks for nuclear waste storage, e.g., in Opalinus Clay (Martin and Lanyon, 2003) or Boom Clay (Labiouse et al., 2014). However, a number of instability problems are encountered while drilling or excavating shale formations; especially with decreasing angle β between the bedding planes and the borehole axis (Figure 4.1), often referred to as 'angle of attack' (Atkinson and Bradford, 2002; Gallant et al., 2007; Gazaniol et al., 1995;

---

[3] T. Meier, E. Rybacki, T. Backers, G. Dresen, Influence of Bedding Angle on Borehole Stability: A Laboratory Investigation of Transverse Isotropic Oil Shale, Rock Mechanics and Rock Engineering, Volume 48, Issue 4, July 2015, Pages 1535-1546, ISSN 0723-2632, http://dx.doi.org/10.1007/s00603-014-0654-1.

Khan et al., 2011; Martin and Lanyon, 2003; Ottesen, 2010; Økland and Cook, 1998; Zoback, 2010).

The structural heterogeneity of shale is attributed to the orientation distribution of minerals and organic matter, typically resulting in the formation of weak bedding planes (e.g., Chenevert and Gatlin, 1965; Gallant et al., 2007) and a pronounced elastic transverse isotropy (TVI) (Dewhurst and Siggins, 2006; Johnston and Christensen, 1995; Vernik and Liu, 1997; Wenk et al., 2008), meaning that properties, e.g., elastic constants and strength properties, parallel to the bedding are isotropic but vary across them (Chong and Smith, 1984).

TVI results in an inhomogeneous stress distribution around boreholes that depends on borehole orientation and the orientation of the deviatory stress fields with respect to bedding (Lekhnitskii, 1968; Amadei, 1983). Several analytical solutions and modeling results exist that predict the stress distribution and borehole collapse or fracture initiation pressures around deviated boreholes in TVI rocks (Aadnoy, 1989; Ong and Roegiers, 1993, 1996; Gupta and Zaman, 1999; Pei, 2008). The differences between isotropic and TVI rocks are negligible if the borehole axis is oriented normal to bedding. In this case, the stress field close to the borehole can be calculated from the stress concentration around a hole in an infinite, linear elastic, and isotropic plate (e.g., Zoback, 2010). However, neglecting the anisotropy for any other orientation, as commonly done in drilling applications (Gaede et al., 2012; Khan et al., 2011; Birchwood and Noeth, 2012), may result in significant errors of stress estimates (Blümling, 1986).

In anisotropic rocks bedding plane slip may have a significant effect on borehole and casing stability (Addis et al., 1993; Dusseault et al., 2001; Gazaniol et al., 1995; Økland and Cook, 1998; Russell et al., 2003; Skelton et al., 1995; Willson et al., 1999) and has been estimated previously (e.g., Daemen, 1983; Gallant et al., 2007; Lee et al., 2012; Vernik and Zoback, 1990). However, the considerable effect of elastic anisotropy has been ignored so far in these analyses.

Experimental studies on shale have been done mainly on samples with boreholes drilled either parallel or perpendicular to the bedding (e.g., Aoki, 1993; Labiouse and Vietor, 2014; Labiouse et al., 2014; Meier et al., 2013). In tests on thick-walled hollow cylinders (TWHC) with bedding planes parallel to the borehole axis Labiouse and Vietor (2014) and Labiouse et al. (2014) observed that breakouts typically initiate at four positions around the borehole wall, leading to a four-lobed breakout pattern in the initial phase of loading. At higher loads, successive buckling failure may occur in direction normal to the bedding (Økland and Cook, 1998; Blümling et al., 2007; Labiouse and Vietor, 2014). Under isostatic stress conditions and with bedding planes normal to the borehole axis Meier et al. (2013) showed that breakouts in shales initiated without any preferred orientation. Just a few studies investigated borehole stability of shales with inclined bedding plane orientations. For instance, Økland and Cook (1998) performed TWHC experiments on organic rich Draupne shale from the North Sea and from an outcrop reference shale (J2) to investigate borehole instabilities encountered in highly inclined wells (β < 10°) drilled in the North Sea. The tests were performed with bedding inclinations of 0°, 10°, 45° and 90°. Experiments conducted on samples with bedding planes parallel to the borehole axis (β = 0°) resulted in unstable failure at low pressures, whereas tests with β > 80° required high pressure to initiate borehole instabilities. Based on these experimental observations, the encountered borehole instability problems in the field were reduced by increasing the 'angle of attack' to >30°, indicating the necessity to study the influence of bedding planes on borehole stability in shales.

Here, we present a series of TWHC experiments on Posidonia shale with varying 'attack' angles between bedding plane and borehole orientation. The laboratory investigations simulated a drill path which deviates from vertical to horizontal through finely bedded shale to study potential changes in failure processes involved in the formation of borehole breakouts. The TWHC experiments are also simulated in a finite element modeling to account for the stress field in the TVI shale.

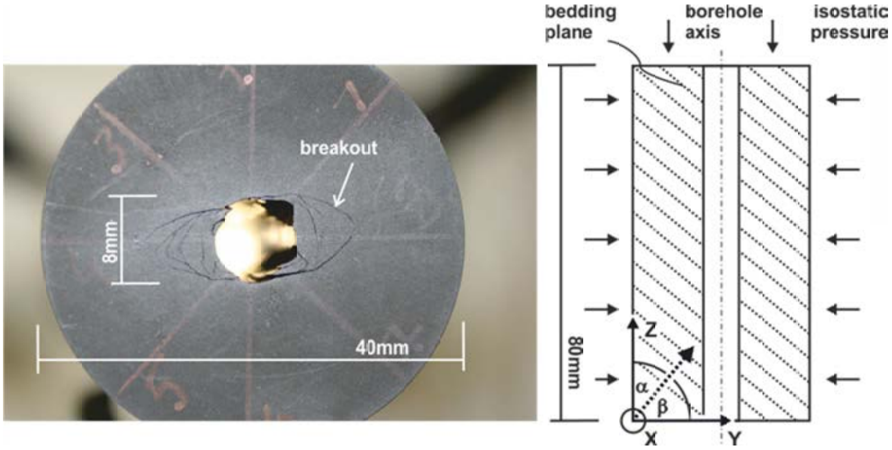

Figure 4.1 a) Top view of a deformed thick-walled hollow cylinder (PN3) with borehole oriented almost parallel to the bedding planes showing borehole breakouts. b) Schematic cross-section of the thick-walled hollow cylinder geometry. α is the angle between the normal to the bedding plane and the borehole/ specimen axis (Z) and β is referred to as the dip angle. The strike of the bedding planes is oriented parallel to the x-axis direction.

4.2 Experimental

4.2.1 Test Material

Samples were prepared from Posidonia shale cores of the Hills syncline in the Lower Saxony Basin, NW Germany. This Lower Jurassic shale was buried to depths of up to ~ 1,800 m before being uplifted to the sub-surface (Mann et al., 1990). The cores, retrieved from a depth interval of

41-51 m, represent a carbonate rich, mature oil shale with a vitrinite reflectance R_o of 0.88% (Littke et al., 1988). The porosity measured by mercury porosimetry is about 1%. The dark gray to black samples show fine bedding, defined by calcareous bands of maximum 1 mm thickness and layered organic matter with embedded sub-parallel framboidal pyrite flakes.

Table 4.1 Petrophysical parameters of tested Posidonia shale (Meier et al., 2013).

Maturity 0.88	0.88
Porosity (%)	1.1 ± 0.3
Avg. pore throat (nm)	<4.1
Calcite content (wt%)	47.3 ± 0.5
Clay content (wt%)	27.8 ± 1.6
Quartz content (wt%)	17.2 ± 0.4
Pyrite (wt%)	5.3 ± 0.2
Total organic carbon, TOC (wt%)	5.8 ± 0.3
Water content (wt%)	~1

The unconfined compressive strength (UCS) parallel to the bedding (index *xy*) is (35%) lower than perpendicular to bedding (index *z*) and distinctly (48%) lower diagonal to bedding (index *45*). Young's moduli are also anisotropic with $E_{xy}/E_z = n \approx 1.7$. Poisson's ratios were found to be $v_{zy} = n - v_{yz}$, where v_{yz} is the Poisson's ratio in opposite loading direction to v_{zy}, being a pre-requisite for transverse isotropic elasticity. The shear modulus normal to bedding can be estimated for oil shales by (Chong and Smith, 1984) $G_z = E_{xy}/\ (1 + n + 2nv_{zy})$ and the shear modulus parallel to the bedding, i.e., in the plane of symmetry, is given by $G_{xy} = E_{xy}/\ (2 + 2v_{xy})$. Measured petrophysical and geomechanical parameters are given in Table 4.1 and Table 4.2, respectively.

Table 4.2 Uniaxial compressive strength (*UCS*) and elastic properties (Young's modulus *E*, Poisson's ratio *v*, shear modulus *G*) of transverse isotropic Posidonia shale.

E_{xy}[a]	17.3 GPa	Ez[a]	10.4 GPa
ν_{xy}	0.18	ν_z	0.30
G_{xy}	8.9 GPa	G_z	5.5 GPa
UCS_{xy}	75 ± 7 MPa	UCS_z	115 ± 7MPa
UCS_{45}	60 ± 10 MPa		
n	1.66	ν_{yz}	0.17

Values marked with [a] are taken from Meier et al. (2013). Indices *xy* and *z* denote parallel and perpendicular to bedding, respectively

4.2.2 Specimen Preparation

Cylindrical specimens were drilled out of the core material under dry conditions with bedding plane orientations *a* (90° - *β*) between 30° and 86° (Figure 4.1). The samples were ground to 40 mm diameter and 80 mm length with parallel end surfaces with an accuracy <20 µm. Finally, a central borehole of 8 mm diameter was drilled dry into the sample using a solid carbon drill bit. During preparation of the thick-walled hollow cylinder, dust and drill cuttings were removed by a high-power vacuum cleaner. Specimen dimensions are given in Table 4.3.

4.2.3 Experimental Techniques

Each sample was equipped with two pairs of strain gauges and jacketed using 2 mm thin rubber sleeves. Strain gauge signals in circumferential (ε_{circ}) and axial (ε_{ax}) direction were stored with a sampling rate of 2 Hz (HBM MGCplus) with an accuracy of ±3 % at positions parallel and normal to bedding. In addition, twelve acoustic emission (AE) sensors were glued directly onto the sample surface and sealed with epoxy resin. The sensors with a resonant frequency of about 2 MHz were used to record AE and to measure elastic p-wave velocities, (v_p), and elastic p-wave amplitudes in axial and radial direction. Transducer signals were amplified by 60 dB using a pre-amplifier equipped with a 100 kHz high-pass filter (Physical Acoustic Corporation). AE's and ultrasonic waveforms were stored using a 16 channel transient recording system (DaxBox, Prökel GmbH) with an amplitude resolution of 16 bit at 10 MHz sampling rate. All experiments have been performed in a stiff, servo-controlled loading frame (MTS), equipped with a 200 MPa confining pressure vessel. For non-destructive visualization of fractures within deformed samples, we used an X-ray computer tomography system (X-ray CT, Phoenix X-Ray nanotom 180NF) with an operation voltage of ≈ 150 kV under ambient pressure conditions. Resolution of the scans varied between 22 and 40 µm per voxel.

Subsequently, the microstructures were analyzed on thin sections prepared normal to the borehole axis using a scanning electron microscope (SEM, Carl Zeiss SMT- Ultra 55 Plus) in normal and backscattered scanning electron mode.

4.2.4 Experimental Procedure

A total of six thick-walled hollow cylinders with $30° < a < 86°$ were loaded by increasing the isostatic pressure at a rate of 1-2 MPa/min until formation of borehole breakouts. The borehole was kept at atmospheric pressure. For each sample, axial and radial strain, AE activity, ultrasonic p-wave velocity and amplitudes were recorded to detect breakout initiation. Unloading of samples was performed at a rate of 2-4 MPa/min.

4.3 Results

4.3.1 Borehole Breakout Initiation Pressures

4.3.1.1 Ultrasonic Velocities, Amplitudes and Acoustic Emission Measurements

Generally, the measured v_p of the specimens increased with increasing confining pressure. Differences of v_p are related to the bedding plane orientation. Measurements parallel to bedding exhibited the highest velocities (4.0 ± 0.3 km/s at 0.1 MPa pressure), whereas the lowest velocities (3.4 ± 0.2 km/s at 0.1 MPa pressure) were recorded normal to bedding. Intermediate velocities were measured along traces inclined 45° to the bedding (Figure 4.2a).

Measurements non-parallel to the bedding planes showed a distinct drop of v_p upon reaching a certain pressure, which is interpreted as the onset of breakout formation, P_{vp}. Measured ultrasonic amplitudes followed the same behavior as the measured v_p but difference in magnitude could not be related to the bedding plane orientation. However, at a certain pressure, P_{amp}, we observed a marked drop in amplitudes, which sets the onset of borehole breakouts.

Due to the low amount of strong minerals (quartz, pyrite) in the investigated shales, AE's were rarely observed during loading, in contrast to sandstones loaded under similar conditions (e.g., Dresen et al., 2010; Papamichos et al., 2010). If present, the AE hypocenters were located close to the borehole with an estimated location error of ±3 mm. A distinct onset or increase in AE activity, indicating breakout nucleation at pressure P_{AE}, was observed only in two experiments (see Table 4.3).

4.3.1.2 Strain Measurements

Figure 2b shows the development of $\Delta P/\Delta\varepsilon_{circ}$ versus P. $\Delta\varepsilon_{circ}$ was measured parallel to the strike of the bedding except sample PN5, where $\Delta\varepsilon_{circ}$ was measured normal to the strike of the bedding. The curves depict initially a continuous, almost linear decrease with increasing pressure. At elevated pressures the samples showed a non-linear compaction behavior, probably due to the formation of inelastic crack damage at the borehole indicating the formation of borehole breakouts at a critical pressure, P_ε, which depends on the bedding orientation. Beyond P_ε the curve dropped significantly during sample compaction, indicating further inelastic deformation of the borehole.

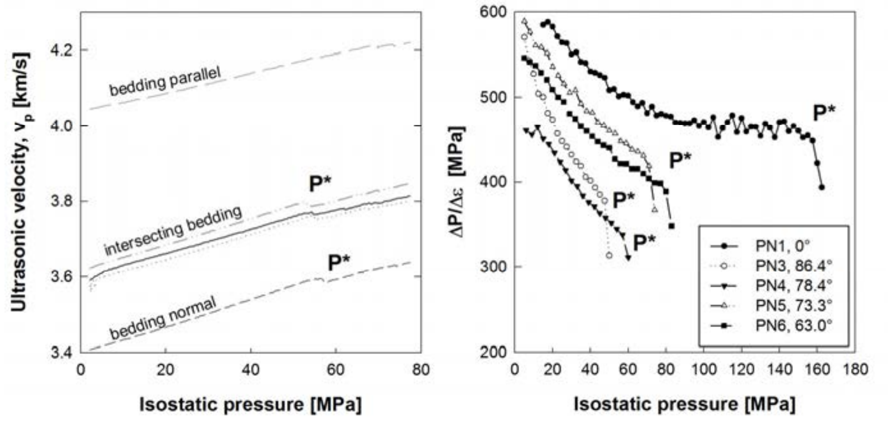

Figure 4.2 a) Radial ultrasonic velocities versus isostatic pressure measured for specimen PN3. P_{vp} in the curves indicate the onset of borehole breakouts. b) Derivative of isostatic pressure changes with change of the associated circumferential strain versus isostatic pressure. P_ε marks the onset of breakout development.

4.3.1.3 Critical Borehole Breakout Initiation Pressures

The average critical isostatic pressure required for breakout nucleation, *P**, is given in Table 4.3, based on strain, AE activity, and ultrasonic p-wave data. For sample PN8, only AE activity was recorded during loading up to 133 MPa pressure. Here, we used additional X-ray CT scans of the deformed specimen after unloading, which showed initial breakout formation. The critical pressure at breakout initiation depends on borehole orientation with respect to bedding as shown in Figure 4.3. *P** decreased almost linearly by 65 % from ~ 151 MPa at α = 0° (normal to bedding) to ~ 52 MPa at α = 86.4° (almost parallel to bedding). Note that the borehole diameters of samples PN1 and PN2 were 6 and 10 mm, respectively. Interpolation of *P** between PN1 and PN2 gave *P** = 151 MPa for a borehole diameter of 8 mm for α = 0° (PN1 and PN2 taken from Meier et al., 2013). The decrease of *P** for thick-walled hollow Posidonia shale cylinders with increasing angle *a* can be approximated by a linear equation of the form *P** [MPa] = 163.1 [MPa] - 1.34α [°] (R^2 = 0.98).

Table 4.3 Specimen geometry, loading rate and critical isostatic confining pressures for borehole breakout formation estimated from the onset of AE activity (P_{AE}), ultrasonic amplitude (P_{amp}), ultrasonic velocity (P_{vp}), and circumferential strain (P_ε).

Sample Name	b (mm)	l (mm)	a (mm)	α (°)	Rate (MPa/min)	P_{AE} (MPa)	P_{amp} (MPa)	P_{vp} (MPa)	P_ε (MPa)	P* (MPa)
PN1	40	80	6	0	1	138	170	160	159	157 ±10
PN2	50	80	10	0	0.5	130	-	144	144	140 ±4
PN*	50	80	8	0	-	-	-	-	-	151 ±5
PN3	40	80	8	86.4 ±0.4	0.5	49	53	54	52	52 ±2
PN4	40	80	8	78.4 ±0.9	2	-	62	61	59	61 ±2
PN5	40	80	8	73.3 ±2.8	1	-	62	62	53	59 ±8
PN6	40	80	8	63.0 ±0.5	1	-	82	79	76	79 ±3

Sample Name	b (mm)	l (mm)	a (mm)	α (°)	Rate (MPa/min)	P_{AE} (MPa)	P_{amp} (MPa)	P_{vp} (MPa)	P_{ε} (MPa)	P* (MPa)
PN7	40	80	8	53.6 ±1.1	1	-	88	88	86	87 ±5
PN8	40	80	8	30 ±2.0	1	126	-	-	-	126 -10

b is specimen diameter, *l* specimen height, *a* borehole diameter, and *a* is dipping angle, PN* is interpolated between PN1 and PN2 using the data from Meier et al. (2013)

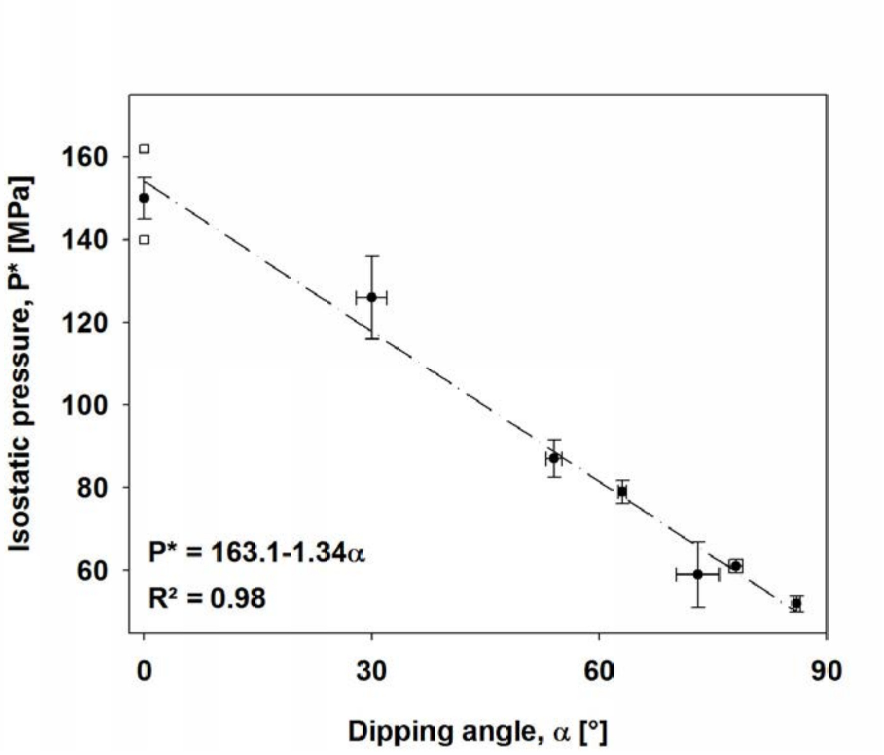

Figure 4.3 Decrease of the critical pressure *P** for borehole breakout initiation with increasing dip angle *a*. Note that specimens PN1 and PN2 (*a* = 0°, open squares) have different borehole diameters (6, 10 mm) compared to the remaining samples (8 mm).

4.3.2 Microstructural Observations

Based on microstructural investigations, initial failure seemed to be always related to slip on bedding planes, leading to a four-lobed breakout pattern. Further loading beyond breakout initiation triggered shear or buckling failure depending on the bedding plane dip (Figure 4.4).

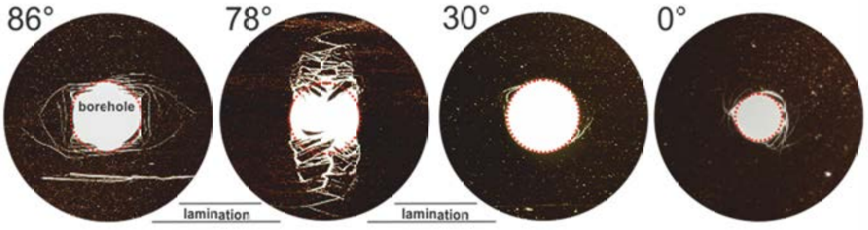

Figure 4.4 Images of breakout pattern for different bedding plane dip angles. The strike of the bedding planes is horizontal in all images.

4.3.2.1 Breakout Formation in Boreholes Oriented Sub-Parallel to Bedding

For specimens with bedding planes intersecting the borehole axis at angles of 63° < *a* < 86°, failure initiated at the borehole wall where the bedding planes are expected to be favorably orientated for shear failure, i.e., 20°-45° to the strike of the bedding (Figure 4.4, Figure 4.5). During loading beyond *P**, small, crescent-shaped fragments were ejected into the borehole resulting in nearly rectangular cross sections as also observed in soft clays (e.g., Labiouse and Vietor, 2014).

Sample PN4 was loaded 25 MPa beyond the breakout initiation pressure causing intense crack damage (Figure 4.4). The X-ray CT images (Figure 4.5) indicate that the progressive crack damage occurred by separation of the rock material into blocky fragments of 0.5-3 mm thickness normal to bedding. These are subjected to bending and increasing tangential stress eventually leading to buckling failure. Breakout propagation appears to be normal to the strike of the bedding planes.

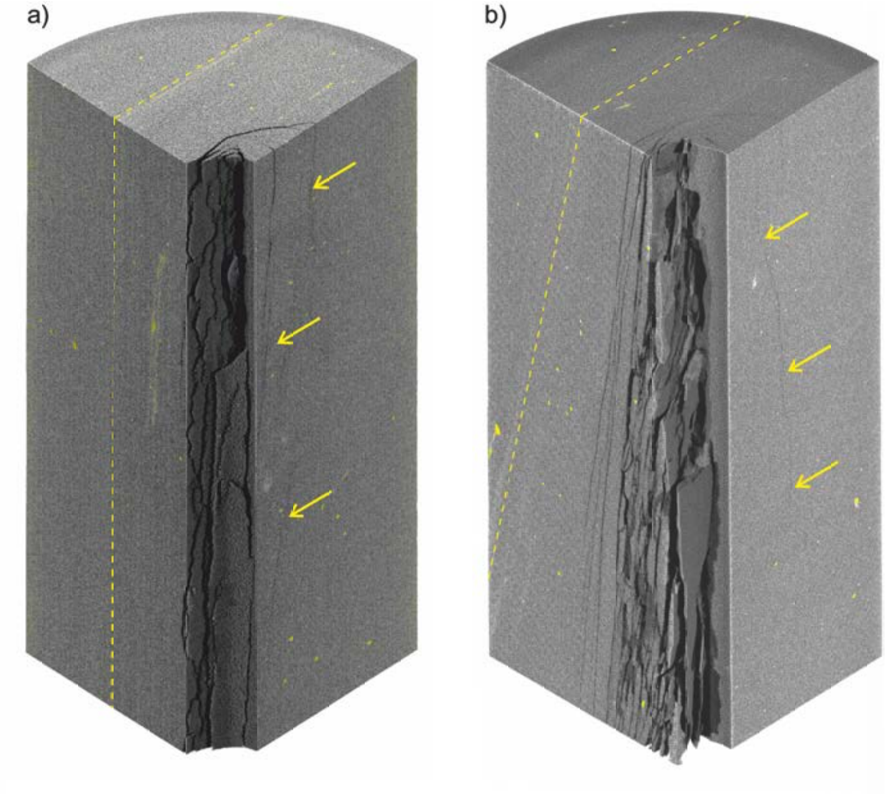

Figure 4.5 X-ray CT scans showing one quarter of deformed specimens a) PN3 and b) PN4 with *a* = 86° and 78°, respectively. The bedding plane orientation is highlighted by a dashed yellow line. Arrows indicate fractures initiated parallel to the bedding.

4.3.2.2 Wellbore Damage in Boreholes Oriented Normal to Bedding

For samples with bedding planes oriented normal to the borehole axis, i.e., *a* = 0°, spiral-shaped shear fractures developed around the borehole. This fracture pattern in Posidonia Shale can be successfully modeled using the Mohr-Coulomb failure criterion (Meier et al., 2013). The observed breakout depth varied along the borehole axis, possibly related to material heterogeneities such as different clay content, clastic minerals and porosity.

For 30° < a < 63°, fractures initiated at about 45° to the strike of the bedding. The fractures propagated along the bedding planes but reoriented into a borehole tangential direction at some distance from the borehole, revealing a double-lobed breakout pattern. Along the borehole wall the fractures followed the bedding planes (Figure 4.6).

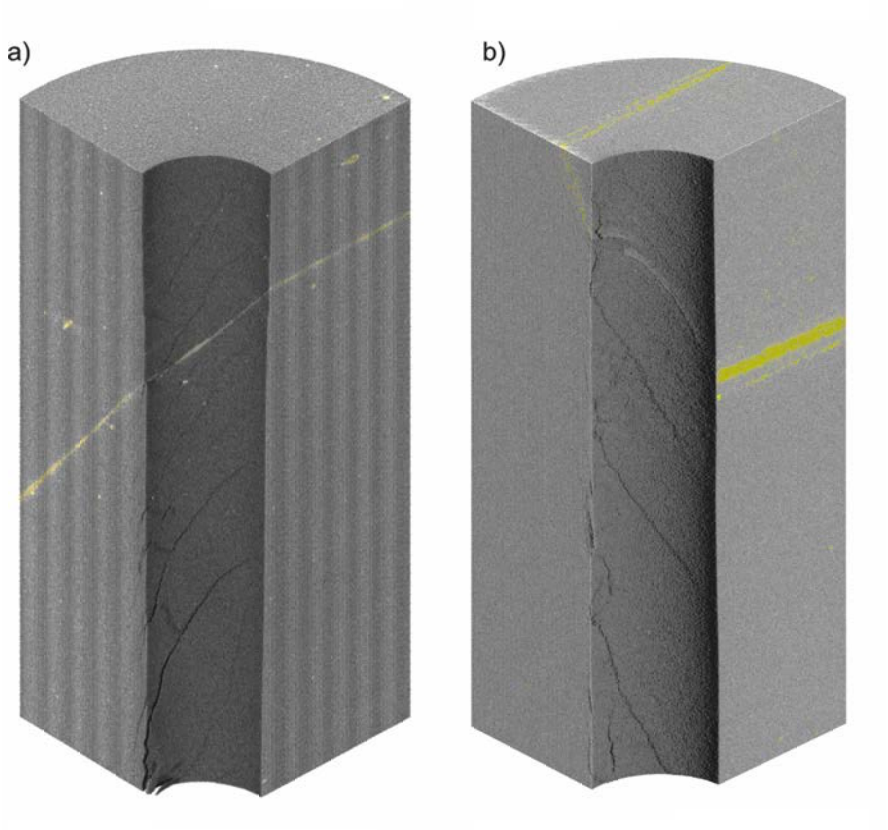

Figure 4.6 X-ray CT scans showing one quarter of specimens a) PN7 and b) PN6 with a = 53° and 63° respectively. The bedding plane orientation is highlighted by yellow lines. Note that dip angles of the bedding are different, producing different breakout patterns.

4.4 Discussion

To explain the influence of the dip angle on stress-induced borehole breakouts in shales, we consider the contributions of elastic and strength anisotropy. The elastic anisotropy is caused mainly by the variations of porosity, organic material and mineral composition between layers of the shale matrix. In contrast, the anisotropy of strength parameters is mainly associated with the existence of weak bedding planes. In the following, we use finite element modeling to analyze the effect of elastic anisotropy on the stress field in a transverse isotropic TWHC with varying bedding plane orientation subjected to isostatic loading.

The determined stress field is then used to evaluate the stresses operating on the bedding planes. From this analysis, the width of potential failure regions around the borehole wall is estimated for different bedding plane orientations and compared to models based on isotropic material behavior.

4.4.1 Stress Field in a Transverse Thick-walled Hollow Cylinder

One quarter of the cylindrical specimens of 40 mm diameter and 80 mm height were meshed using a commercial finite element (FE) code (COMSOL Multiphysics). The mesh size was fourfold refined by an arithmetic sequence toward the 8 mm borehole (Figure 4.7a). The borehole perimeter was divided into 12 radial segments and 80 segments along its height. In total, the mesh consisted of 11,520 hexahedra.

To model the stress distribution prior to failure, we assumed a linear elastic material behavior using the parameters listed in Table 4.2. The isostatic load was applied to the mantle and top surface of the cylinder, whereas the bottom surface was fixed with zero displacement in vertical direction (along the z-axis) and without kinematic constraints in the XY-plane. The borehole wall was defined as a pressure-free boundary.

In the simulation, the coordinate system of the applied isostatic stress field coincided with the coordinate system of the TWHC (*X*, *Y*, *Z*). In contrast, the coordinate system of the material properties was rotated around the x-axis by different angles *a* in order to simulate the varying dip of the bedding planes with respect to the borehole axis. Hence, the strike of the lamination was always in *X*-direction. For each point in the FE model, the full stress tensor was obtained in the *X*, *Y*, *Z* coordinate system from which the tangential $\sigma_{\Theta\Theta}$, radial σ_{rr}, and vertical stress σ_{zz} are determined by

$$\sigma_{\theta\theta} = \frac{1}{2}(\sigma_{XX} + \sigma_{YY}) - \frac{1}{2}(\sigma_{XX} - \sigma_{YY})\cos 2\theta - \sigma_{XY}\sin 2\theta \qquad 4.1$$

$$\sigma_{rr} = \frac{1}{2}(\sigma_{XX} + \sigma_{YY}) + \frac{1}{2}(\sigma_{XX} - \sigma_{YY})\cos 2\theta + \sigma_{XY}\sin 2\theta \qquad 4.2$$

$$\sigma_{zz} = \sigma_{ZZ} \qquad 4.3$$

where Θ is the positive angle measured counterclockwise from the x-axis toward the y-axis (see Figure 4.7a).

Figure 4.7b and c shows the tangential and vertical stress distributions versus Θ at the borehole wall, normalized to the critical isostatic pressure P^* for breakout initiation for the bedding dip angles measured in our experiments. At the borehole wall the radial stresses are equal to zero due to the pressure-free borehole and are not shown.

In case of bedding planes orientated normal to the borehole axis ($a = 0°$), a radial symmetric stress distribution is achieved due to isotropic material properties in radial direction. This result is consistent with analytical solutions for TWHCs based on linear elastic and isotropic material behavior (e.g., Jaeger et al., 2007).

In case of bedding planes inclined to the borehole axis ($a \neq 0°$) the model predicts two local tangential stress maxima and one minimum, which progressively increase in magnitude with increasing bedding plane inclination (Figure 4.7b). These stress distributions are in agreement with analytical solutions for linear elastic and transverse isotropic material behavior (e.g., Aadnoy, 1989). At a dip angle of $a = 86°$ (PN3), the ratio $\sigma_{\Theta\Theta}/P^*$ varies from 2.01 ($\Theta = 45°$) to 2.18 ($\Theta = 90°$), which corresponds to a maximum change of about 4.6 % in tangential stress compared to isotropic material ($\sigma_{\Theta\Theta}/P^* = 2.08$). It is interesting to note that the vertical stress changes with dipping angle as shown in Figure 4.7c. However, compared to the experimental data the change in tangential and vertical stress is too small to explain the observed decrease in the breakout initiation pressure of the shale samples of about 65% with increasing dip angle.

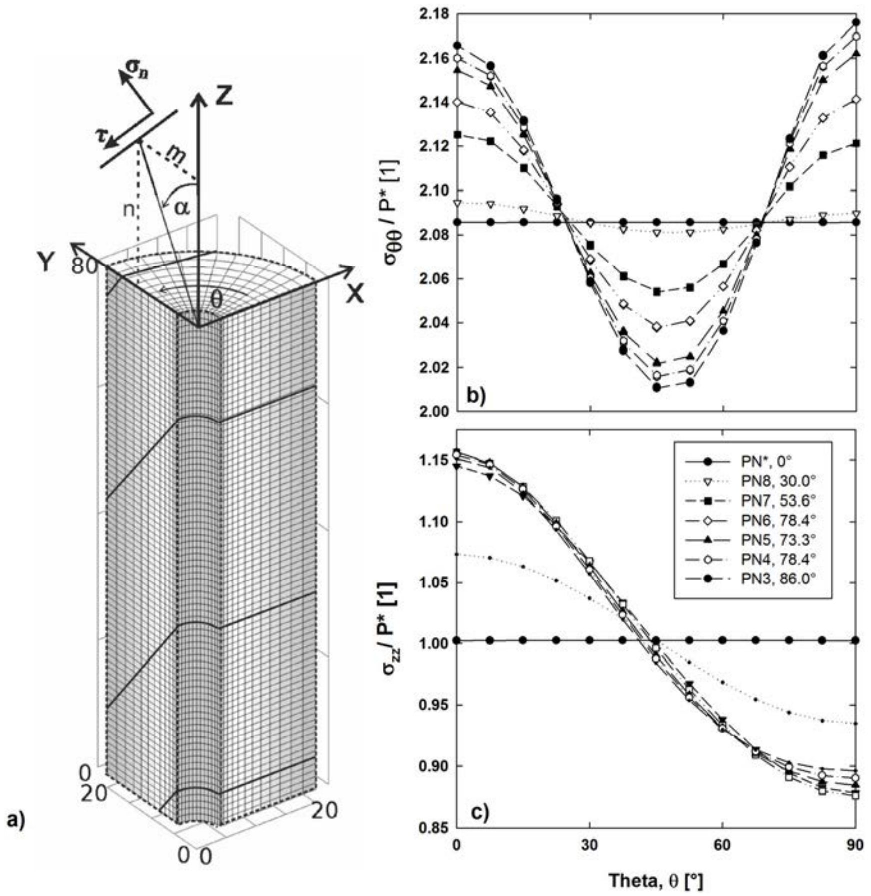

Figure 4.7 a) FEM mesh consisting of 11,520 hexahedra with bedding plane orientation represented by thick black lines. b) Normalized tangential stress and c) vertical stress at the borehole wall for different bedding plane orientations *a* versus azimuth angle *Θ* between strike of bedding planes and stress direction.

4.4.2 Stress Acting on Inclined Bedding Planes

Microstructural observations suggest that for $a \neq 0°$ failure at the borehole wall is localized at the bedding planes acting as planar weak zones. Therefore, we assume that the nucleation of borehole breakouts occurs if the shear stress parallel to bedding exceeds a critical value that initiates local slip.

Shear stress, τ, and normal stress, σ_n, operating on bedding planes with varying orientation can be expressed by (Jaeger et al., 2007)

$$\sigma_n = \sigma_{XX} l^2 + \sigma_{YY} m^2 + \sigma_{ZZ} n^2 + 2(\sigma_{XY} lm + \sigma_{YZ} mn + \sigma_{XZ} nl) \qquad 4.4$$

$$\tau = \sqrt{(\sigma_{XX} l + \sigma_{XY} m + \sigma_{XZ} n)^2 + (\sigma_{XY} l + \sigma_{YY} m + \sigma_{YZ} n)^2 + (\sigma_{XZ} l + \sigma_{YZ} m + \sigma_{ZZ} n)^2 - \sigma_n^2} \qquad 4.5$$

where l, m, n are the direction cosines of the normal to the plane. For a TWHC with the strike of the bedding parallel to the x-axis (see Figure 4.7a), the direction cosines between the axis of the borehole and the normal to the bedding plane are given by

$$\begin{aligned} l &= \sqrt{1 - \cos(90° - \alpha)^2 - \cos(\alpha)^2} = 0, \\ m &= \cos(90° - \alpha), \\ n &= \cos(\alpha) \end{aligned}$$

Inserting l, m, n into Equations 4.4 and 4.5 yields

$$\sigma_n = \sigma_{YY} m^2 + \sigma_{ZZ} n^2 + 2\sigma_{YZ} mn \qquad 4.6$$

$$\tau = \sqrt{(\sigma_{XY} m + \sigma_{XZ} n)^2 + (\sigma_{YY} m + \sigma_{YZ} n)^2 + (\sigma_{YZ} m + \sigma_{ZZ} n)^2 - \sigma_n^2} \qquad 4.7$$

Based on these relationships and accounting for the stress field of the transverse isotropic shale cylinder, we calculated the shear and normal stress acting on the weak bedding planes. As shown in Figure 4.8a and b, the shear stress reaches a maximum at an angle of Θ = 45° whereas the normal stress decreases monotonically with increasing Θ. The shear and normal stress for a TWHC with bedding planes normal to the borehole axis (e.g., PN1 in Figure 4.8a and b) yields zero and the vertical stress, respectively.

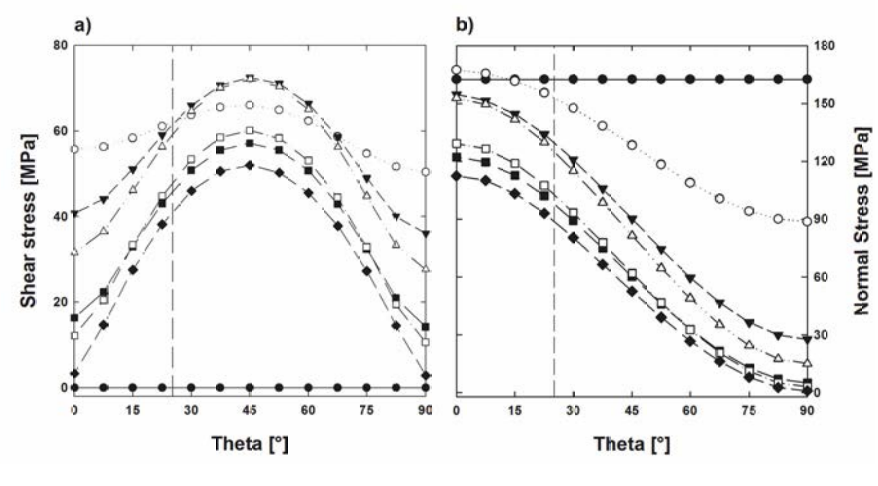

Figure 4.8 a) Shear stress, and b) normal stress along the borehole periphery. Dashed lines indicate Θ = 25°.

In most experiments performed on specimens with bedding inclined to the borehole axis, initial failure occurred at Θ between 20° to 30° (PN3 to PN5). Assuming that failure along bedding planes occurred for most tests at an average $\Theta = 25° \pm 5°$ we can estimate the cohesion and friction coefficient by applying a linear Mohr-Coulomb failure criterion. Using the calculated shear and normal stresses at $\Theta = 25°$ (vertical lines in Figure 4.8a, b), the estimated friction coefficient μ_w is 0.37 (friction angle 20.3°) and the cohesion C_w is 9.6 MPa for bedding plane slip in Posidonia shale. Note, that samples with $a = 0°$ are not taken into account here since bedding plane slip is not possible. The estimated friction coefficient and cohesion for the weak bedding planes are distinctly lower than the cohesion and friction coefficient determined for triaxial compression of intact Posidonia shale specimens cored normal to bedding, i.e., $a = 0°$ (pers. comm. M. Makasi, Figure 4.9).

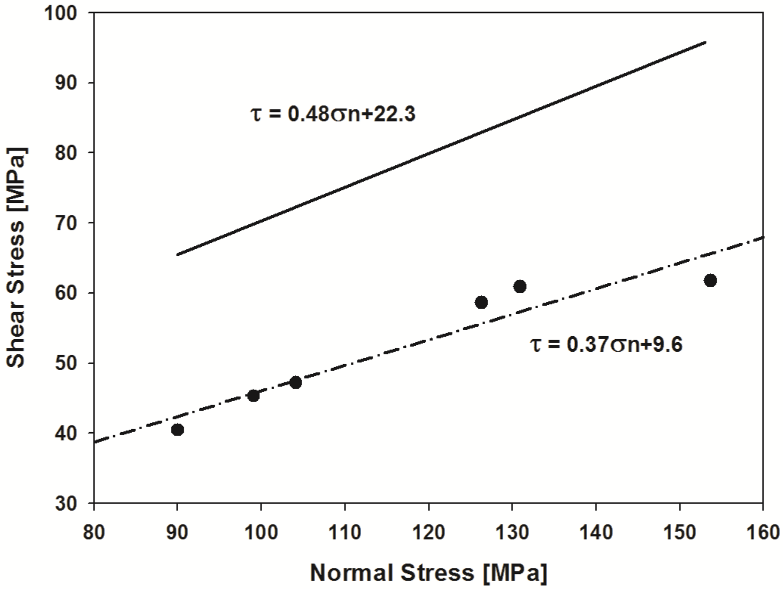

Figure 4.9 Modeled shear versus normal stress for breakout initiation of samples PN3 to PN8. Solid line represents the Mohr–Coulomb failure criterion of intact Posidonia shale tested normal to bedding (pers. comm. M. Makasi).

The effect of weak bedding planes on potential failure regions around the borehole is illustrated in Figure 4.10 using the results of the numerical simulations and accounting for the difference between isotropic and TVI material. For low inclination angles broad to double-lobed failure regions form whereas distinct four-lobbed breakouts develop for high bedding plane inclinations. Variations in failure patterns between isotropic and TVI material are negligible as expected from the relatively small differences in tangential and vertical stress between isotropic and TVI material behavior (see Figure 4.7b, c). However, the modeled slip zones are in good agreement with the observed initial failure patterns, in particular at large dip angles.

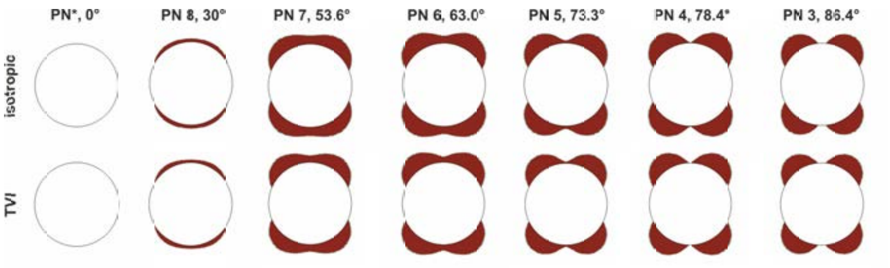

Figure 4.10 Modeled breakout pattern around the borehole for different bedding plane inclination angles in isotropic rock (top) and TVI rock (bottom).

4.4.3 Comparison to Another Approach for Predicting Failure of Rocks Containing Weak Bedding Planes

Vernik and Zoback (1990) proposed a model to predict borehole breakouts in isotropic rocks containing weak bedding planes with different dipping angles. Using the Mohr-Coulomb failure criterion the strength of those rocks can be described by

$$S_1 = S_3 + \frac{2(S_w + \mu_w S_3)}{(1-\mu_w \cot\theta)\sin 2\theta} \qquad 4.8$$

where Θ is the angle between the maximum principle stress S_1 and the normal to the bedding plane and S_w is the intrinsic shear strength, which is given by

$$S_w = 2C_w\left(\sqrt{\mu_w^2+1}+\mu_w\right) \qquad 4.9$$

For a pressure-free borehole with $S_3 = \sigma_{rr} = 0$ and $S_1 = \sigma_{\Theta\Theta}$ Equation 4.8 and

$$\sigma_{\theta\theta,f} = \frac{4C_w\left(\sqrt{\mu_w^2+1}+\mu_w\right)}{(1-\mu_w \cot\theta)\sin 2\theta} \qquad 4.10$$

can be re-written as

$$\sigma_{\theta\theta,f} = \frac{4C_w\left(\sqrt{\mu_w^2+1}+\mu_w\right)}{(1-\mu_w \cot\theta)\sin 2\theta} \qquad 4.10$$

which yields the maximum tangential stress the bedding planes can sustain and borehole failure along bedding planes is anticipated in case $\sigma_{\Theta\Theta} > \sigma_{\Theta\Theta,f}$. If the strength of the intact rock is lower than $\sigma_{\Theta\Theta,f}$ for some arbitrary Θ, failure for the intact rock is anticipated in case $\sigma_{\Theta\Theta} > UCS$. This failure criterion is of a shoulder-type form predicting equal strength parallel and normal to the bedding and a reduced strength in between, which may be applicable for some isotropic rocks containing weak bedding planes (Donath, 1961), but does not seem to fit TVI rocks (Pei, 2008), where the strength normal to bedding is larger than parallel to bedding. We, therefore, adjusted the criterion to fit the strength of Posidonia shale based on the measured *UCS* (Table 4.2) using UCS_z for the strength normal to bedding (small Θ) and UCS_{xy} for the strength parallel to the bedding (large Θ). Figure 4.11 shows the predicted strength of Posidonia shale around the borehole for different cohesions values. For a slightly reduced C_w of 7 MPa compared to 9.6 MPa as obtained from the TWHC test, the measured *UCS* at 45° can be adequately fitted. Failure patterns predicted by this failure criterion for the TWHC experiment (PN3) with bedding plane sub-parallel to the borehole axis are shown in Figure 4.11 (inset), being in good agreement to the observed failure patterns.

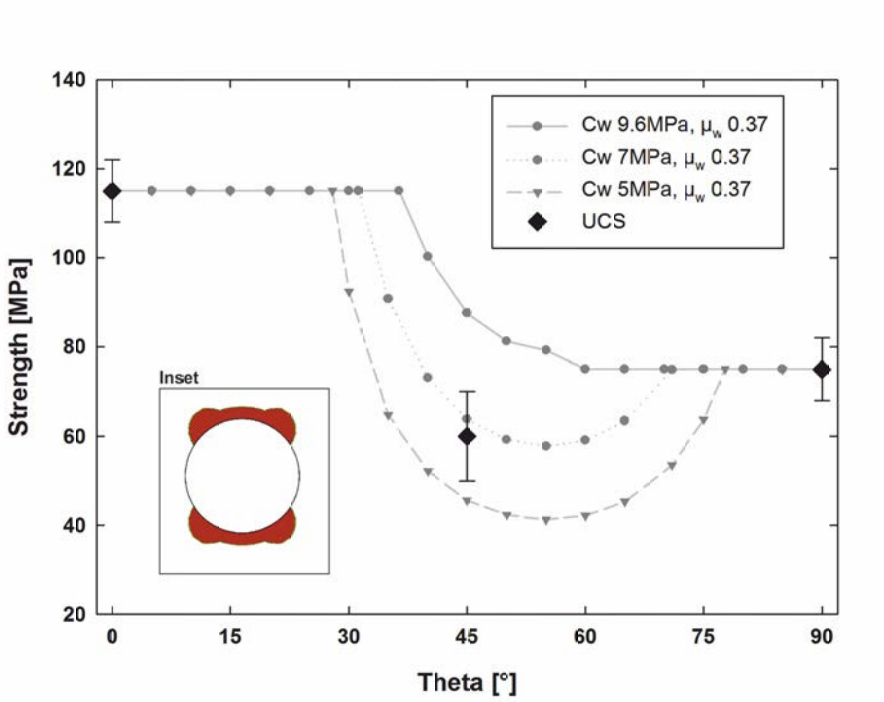

Figure 4.11 Strength around one quarter of a borehole and predicted breakout pattern based on a modified failure criterion proposed by Vernik and Zoback (1990). Bedding plane strike is at $\Theta = 0°$.

4.5 Conclusions

The observed initial failure was due to slip along bedding planes. This initial failure being a starting point for more severe breakouts forming either as shear or buckling failure. The latter failure process occurred particularly in boreholes sub- to parallel to the bedding planes, which needed the lowest stresses to induce borehole breakouts. This is in close agreement with documentations of borehole instabilities drilled in bedded formations.

Numerical modeling of the stress field in the thick-walled hollow cylinder showed that, depending on the bedding plane inclination, the stress field varies up to 4.6% from isotropic solutions. This stress anisotropy induced by the anisotropy of the elastic constants is minor and negligible in comparison to the strength anisotropy of the rock. Borehole integrity in the tested Posidonia shale is, hence, depending on the strength of bedding planes.

The strength of the weak bedding planes, in terms of cohesion and friction coefficient, could be determined by resolving the shear and normal stress on the weak bedding planes at the onset of breakout initiation. The determined strength parameters were then used to successfully predict the observed breakout patterns at the beginning of breakout development. Furthermore, the model of Vernik and Zoback (1990) was modified and applied successfully on shales.

ACKNOWLEDGMENTS

We are cordially thankful for the funding by the GeoEn project of the Federal Ministry of Education and Research in Germany and the co-operation with the GASH project. We would like to thank an anonymous reviewer and the editor for their helpful comments on an earlier version of this manuscript. Furthermore, we would like to thank Stefan Gehrmann and Matthias Kreplin for their excellent work in specimen and thin section preparation. Masline Makasi is also acknowledged for provision of triaxial strength data.

5 BOREHOLE BREAKOUTS IN ISOTROPIC SANDSTONE AND TRANSVERSELY ISOTROPIC SHALES SUBJECTED TO TRUE TRIAXIAL STRESSES[4]

SUMMARY

We investigated experimentally borehole breakouts under true triaxial stress conditions ($\sigma_1 \geq \sigma_2 \geq \sigma_3$) in transversely isotropic Posidonia shale and nearly isotropic Bentheim sandstone. The experimental results are compared with borehole breakout experiments performed under conventional ($\sigma_1 > \sigma_2 = \sigma_3$) triaxial loading conditions. Breakout pattern in Posidonia shale feature shear failure at the onset of breakout development superposed by buckling failure at higher loads if the bedding is parallel to the borehole axis and to the maximum horizontal stress, similar to breakouts observed under conventional loading conditions. Bentheim sandstone shows slot-like breakouts under true- and conventional triaxial loading conditions. Independent of loading condition and rock type, the breakout initiation stress scales with borehole diameter and can be adequately described with a fracture mechanics based failure criterion, which can be extended to accommodate the influence of bedding planes.

5.1 Introduction

Deviated and horizontal drilling is nowadays common practice in the oil and gas industry as aboveground economic and ecologic benefits (e.g., Allen et al., 1997) outbalance sub-surface drilling problems (e.g., Bennetzen et al., 2010). Furthermore, the stimulation and exploitation of low permeable oil and gas shales requires horizontal drilling for effective production. During drilling the rock mass is penetrated at different orientations with respect to the bedding of shales, resulting in a complicated stress field at the circumference of the borehole. The altered stress field around the borehole may enhance the formation of tensile and compressive failure and can lead to borehole instabilities and incomplete cementation, increasing the risk for leakage of geo-fluids from producing to overlying formations, as summarized by Davies et al. (2014).

Geomechanical research on black shales has kicked off with the unconventional oil and gas boom in North America. The research focused on characterizing the rock strength at different temperature and pressure conditions (e.g., Eseme et al., 2006; Sone and Zoback, 2013a, 2013b;

---

[4] Manuscript in preparation.

Rybacki et al., 2015, 2016). However, experimental studies of borehole stability in black shales are few. A couple of studies not related to black shales dealt with borehole instability problems encountered when drilling through soft shales (Økland and Cook, 1998) or shale formations considered for potential radioactive waste disposals (e.g., Labiouse and Vietor, 2013; Labiouse et al., 2014). All of the tested shales disintegrated into slabs during breakout formation, which subsequently buckled and rotated into the borehole if the maximum principle stress around the borehole was parallel to bedding. The thickness of the thereby created slabs seems to depend on the spacing of the bedding planes. Similarly, narrowly spaced joints or fractures can separate the rock mass into slabs that detach from the surface of underground constructions (e.g., Blümling et al., 2007; Brady and Brown, 2006). In true triaxial tests on coal specimens, Kaiser et al. (1985) found „mirror-symmetric rupture zones with rotated fragments". Ottensen (2010, and references therein) observed a similar failure pattern in microtunnels drilled through claystone, described as „buckling and failure along bedding or other planes of weakness". These observations indicate an anisotropic strength of the material related to the planes of weakness that significantly affects the failure mode.

In isotropic sandstone, randomly distributed defects scaling with average grain size were observed to dominate borehole failure (Dresen et al., 2010). Since, those defects are significantly smaller than the borehole diameter, the shape of the breakout is hence not related to depend strength anisotropies but rather on cementation and porosity. For example, low porosity sandstones tend to develop cusp-shaped breakouts while in high-porosity, weakly cemented sandstones cusp-shaped breakouts turn into long, slot-like breakouts (e.g., Cuss et al., 2003a, 2003b; Haimson, 2001, 2003).

This paper presents results of borehole breakout experiments performed on finely bedded Posidonia shale and homogeneous Bentheim sandstone under true triaxial stress conditions, where the magnitudes of all three principal stresses are different ($\sigma_1 > \sigma_2 > \sigma_3$). The results are compared with thick-walled hollow cylinder experiments performed under conventional triaxial loading conditions on shales (Meier et al., 2013, 2015) and sandstone (Dresen et al., 2010), respectively, where the magnitudes of two principal stresses are equal ($\sigma_1 > \sigma_2 = \sigma_3$). Initial breakout size and breakout stress are calculated by means of a fracture mechanics based failure criterion for isotropic rocks (Dresen et al., 2010), which is extended to true triaxial loading conditions and varying bedding plane orientations.

5.2 Rock Tested and Their Mechanical Properties

For true triaxial experiments, 4 specimens have been prepared from Bentheim sandstone (BE) and 5 specimens from Posidonia shale (PS). BE is a homogeneous, highly porous (21.6±0.9%, Reinicke, 2009) sandstone of Lower Cretaceous age from the Gildehaus quarry in NW Germany. It is composed of 96.5% quartz, 2% feldspar and 1.5% clay (Klein et al., 2001). The quartz grains are typically subrounded with sutured grain contacts and silica cement overgrowth (Dresen et al., 2010). The rock does not show bedding planes or other kinds of anisotropy.

PS is a freshly blasted, finely bedded and porous (10.4±0.6%) oil shale of Lower Toarcian age. Samples have been collected from a quarry located in the SW German Basin. The depositional history of PS at the quarry site is described by Röhl and Schmid-Röhl (2005). The shale is composed of 55.6±0.6% calcite, 23.2±1.5% clay, 16.2±0.4% quartz and 4.9±0.2% pyrite (Meier et al., 2013). PS samples show a high total organic carbon content of 8.3±0.2% (Meier et al., 2013) of low maturity with vitrinite reflectance of Ro = 0.5% (Röhl et al., 2001; Eseme et al., 2006), probably due to relatively low burial depths of max. 700 m (pers. comm. Jäger). Due to its bedded structure, PS is transverse isotropic (TVI, Meier et al., 2015).

BE and PS are regarded here as representatives for conventional and unconventional reservoir rocks, respectively. Their geomechanical parameters are given in Table 5.1.

Table 5.1 Mechanical parameters of BE and PS. ν is the Poisson's ratio, E is the Young's modulus, K_{IC} is the Mode I fracture toughness, UCS is the uniaxial compressive strength, and μ is the internal friction coefficient. Δr and c are the distance from the borehole wall and the initial defect half-length.

Parameter	BE*	PS$_{xy}$**	PS$_{z}$**
ν [1]	0.2	0.14	0.38
E [GPa]	25±2	9.4±0.9	5±0.5
KIC [MPa√m]	0.93±0.5	0.49±0.1	1.14±0.4
UCS [MPa]	49	71±7	80±8
μ [1]	0.65	0.4	
Δr [m]	185e-6	150e-6	
c [m]	180e-6	45e-6	

* Dresen et al., 2010. ** Meier et al., 2013; 2014. Subscripts z and xy denote loading directions perpendicular and parallel to the bedding planes (see Figure 5.1).

5.3 Experimental Procedure

Cuboids of 178 mm height, 127 mm width and 127 mm depth were tested under true triaxial loading conditions at the University of Wisconsin-Madison (USA). The specimens were placed into a biaxial loading apparatus, which can apply two independent principal horizontal stresses through loading pistons with loading capacities of 3.8 MN. Friction between the loading pistons and the specimens was reduced by inserting cooper shims with a mixture of stearic acid and petroleum jelly. The vertical stress was applied by a hydraulic ram with a loading capacity of 1.3 MN at the base of the loading frame (Lee, 2005). Three independent servo-control units were used to increase the pressure in each of the three loading directions. An electric drill rig mounted above the specimen allowed drilling of a 23 mm diameter borehole along the long specimen axis while keeping the true triaxial stress constant. During drilling, the borehole was flushed with tap water. Further details on the experimental facilities can be found in Haimson and Lee (2004) or Lee (2005).

After drilling, the stress state was kept constant for 10 to 20 minutes to allow the circulating tap wash to flush out all ejected particles or slabs out of the borehole. Deformed specimens were dried and impregnated with epoxy. After curing of epoxy, the specimens were cut to dimensions suitable for X-ray computer-tomography (X-ray CT) scans. X-ray CT-scans were performed at the Helmholtz Centre Potsdam (GFZ) German Research Centre for Geoscience. We used a high resolution X-ray CT system (Phoenix X-ray nanotom 180NF) allowing non-destructive analysis of the sample with a resolution of 22 μm per voxel. Breakout length (l) and breakout width (ω) were measured 8 times along the borehole axis in equidistant steps (see Figure 5.2a for the geometric entities l and ω). In addition, thick- and thin sections were prepared perpendicular to the borehole and investigated with a binocular microscope.

Figure 5.1 shows schematic views of the loading configuration of the tested specimens under true triaxial conditions from the top (a) and in cross section (b). The angle θ is measured counter-clockwise from the direction of maximum horizontal stress S_H and γ is the angle measured counter-clockwise from the X- axis. In all shale experiments the bedding plane orientation was parallel to the XZ-plane. The maximum horizontal stress was oriented either parallel ($\gamma = 0°$) or normal ($\gamma = 90°$) to the X- axis/bedding plane. Note, that the coordinate system (X, Y, Z) does not correspond to the coordinate system of the bedding planes (x, y, z), with the x-y axes being parallel to bedding.

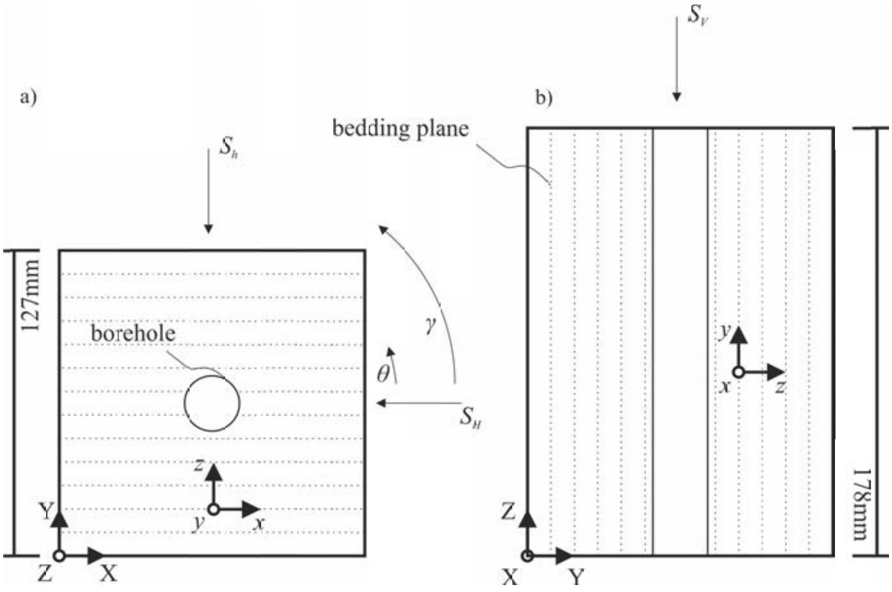

Figure 5.1 Schematic view of specimen geometry and loading configuration in (a) top view and (b) cross section. The orientation of the bedding planes (dashed lines) is fixed with respect to the global coordinate system (X, Y, Z). The coordinate system x, y, z corresponds to the bedding plane orientation.

5.4 Results

The loading conditions were chosen to induce breakouts based on experiments conducted beforehand under conventional triaxial conditions on BE (Dresen et al., 2010) and PS (Meier et al., 2013). The maximum and minimum horizontal stresses ranged from 50 MPa to 75 MPa and from 15 MPa to 45 MPa, respectively. The vertical stress varied between 27 MPa to 50 MPa. Table 5.2 and Table 5.3 summarize the loading conditions for isotropic BE and TVI PS, respectively.

Table 5.2 Experimental conditions for BE. Maximum horizontal stress S_H, vertical stress S_v, minimum horizontal stress S_h, breakout length l, breakout width ω, and maximum tangential stress $\sigma_{\theta,\max}$.

Sample Name	S_H [MPa]	S_v [MPa]	S_h [MPa]	l [mm]	ω [°]	$\sigma_{\theta,\max}$ [MPa]	$\sigma_{\theta,\max}$/UCS [-]
BE1	60	27	45	3.42±0.58	45.8±7.0	142-7	2.90
BE2	60	50	30	-	-	161-6	3.29
BE3	60	50	15	3.74±0.32	24.1±3.3	179-6	3.50
BE4	70	50	15	6.62±0.98	34.2±5.0	212-6	4.10

Table 5.3 Experimental conditions for PS. Maximum horizontal stress S_H, vertical stress S_v, minimum horizontal stress S_h, orientation of S_H with respect to the X-axis, average breakout length l, average breakout width ω, and calculated maximum tangential stress $\sigma_{\theta,max}$.

Sample Name	S_H [MPa]	S_v [MPa]	S_h [MPa]	γ [°]	l [mm]	ω [°]	$\sigma_{\theta,max}$ [MPa]	$\sigma_{\theta,max}$/UCS [-]
PS8	50	40	20	90	0	0	138-8	1.73*
PS9	75	50	20	90	5.50±2.5	141.5±6.0	216-11	2.70*
PS10	50	40	20	0	4.31±0.22	73.8±8.2	155-25	2.18**
PS11	65	50	20	0	5.97±0.86	79.8±5.4	211-36	2.97**
PS12	57.5	50	20	0	9.13±0.86	79.1±6.2	183-30.5	2.58**

* normalized with *UCSz*, ** normalized with *UCSxy*.

5.4.1 Bentheim Sandstone

Borehole breakouts in BE occurred at positions normal to the maximum horizontal stress. At low differential stresses ($S_H - S_h$) of <15 MPa the specimens developed cusp-like breakouts (Figure 5.2), indicated by large breakout widths and short breakout lengths. The cusp-shaped breakout showed in Figure 5.2a reveals different microcrack mechanisms: along the breakout wall in form of intergranular cracks (Figure 5.2b) and intragranular crack damage at the breakout tip (Figure 5.2c). The intergranular damage forms long breakout parallel spalls, which are ejected into the borehole forming broad, triangular breakouts.

At elevated true triaxial stresses breakouts narrowed forming elongated slot-like breakouts (Figure 5.3). The right flanks of the upper and lower breakout in Figure 5.3 are considerably wider than the left flanks, presumably resulting from the initial (cusp-shaped) breakout. Along the borehole axis the breakout formed a narrow zone of ejected material. Only a few intergranular cracks forming at the tip of the breakout are evident (Figure 5.3c), while grains adjacent to the breakout are almost free of microcracks (Figure 5.3b). The crack damage is significantly reduced compared to the cusp-shaped breakout.

Breakout development in high porous sandstones is shown in a conceptual model in Figure 5.3d-f. At tangential stresses exceeding the strength of the rock the breakout initiates (Figure 5.3d). Due to a high stress concentration at the breakout tip grains crush and water circulating in the borehole removed the crushed fragments (Figure 5.3e). Finally, with increasing length of the breakout the crushed grains within the narrow slot form a band of compacted material once removal of the debris by water has stopped (Figure 5.3f).

Reported breakout width and breakout length were measured from X-ray CT scans (see Figure 5.2a) and are summarized in Figure 5.4. The data is plotted versus the normalized borehole length as the borehole length varied between 84.2 and 106.2 mm. The scatter in the breakout length is largest for the longest slot-like breakouts (BE4). Width of breakouts is between 24.1 and 45.8°. The scatter in breakout width seems to be independent of the breakout type in Bentheim Sandstone.

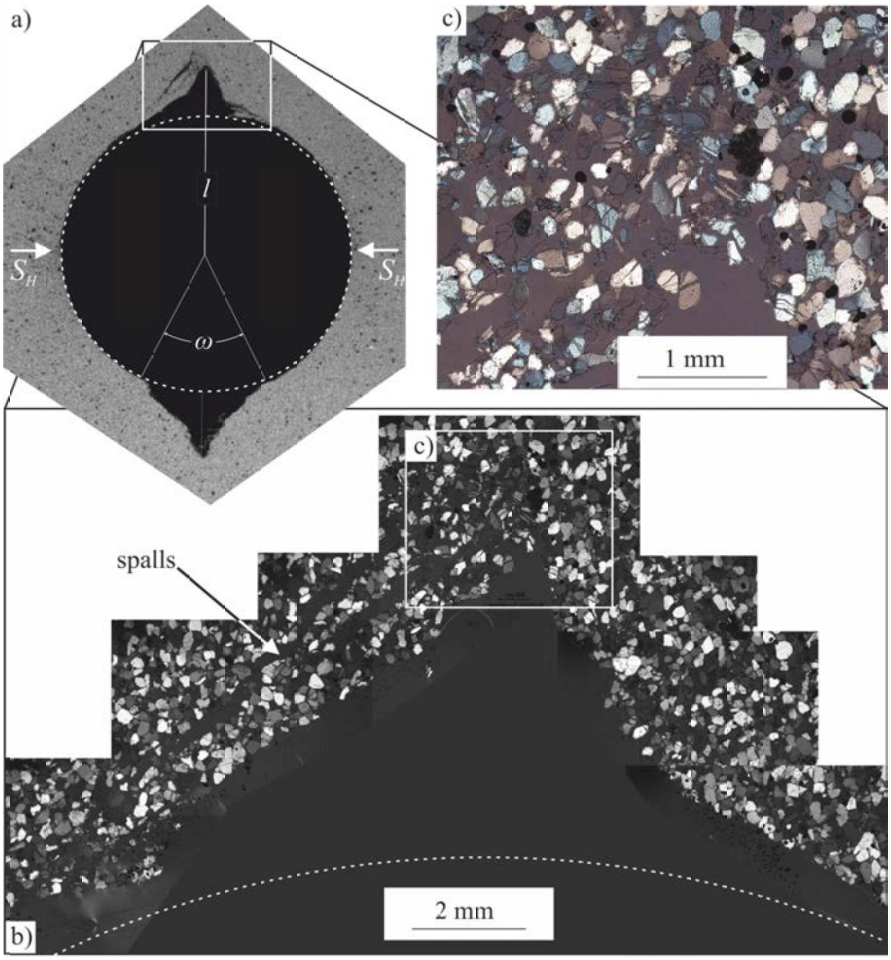

Figure 5.2 Images of sample BE1 showing cusp-shaped breakouts in a cross-section obtained from a X-ray CT slice in the middle of the specimen (a). The inset in (a) is enlarged in micrograph (b), showing breakout parallel spalls and intense microcracking at the breakout tip (c).

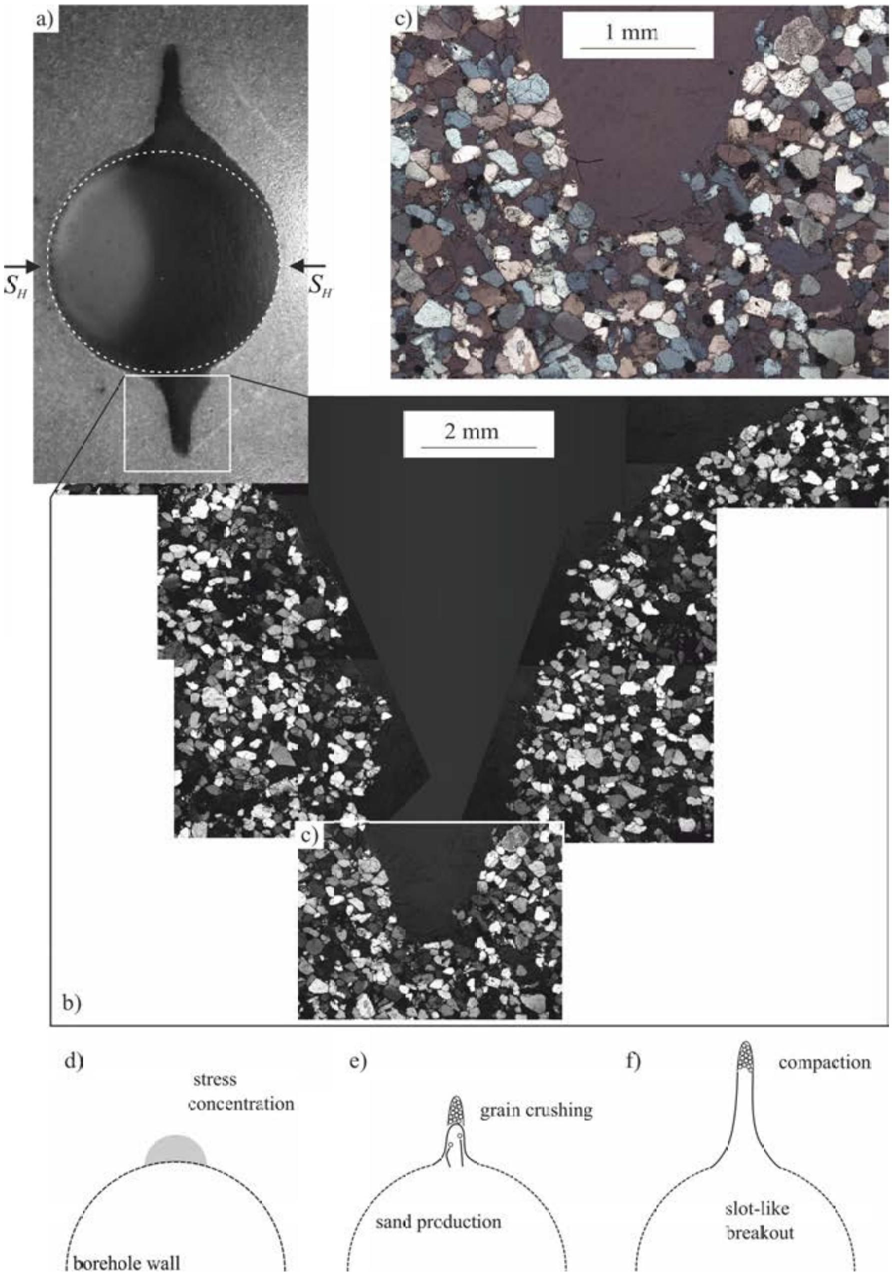

Figure 5.3 Micrographs of specimen BE4. (a) Thick-slab from the middle of the specimen, showing elongated and narrow breakouts normal to S_H. Micrographs reveal only minor crack damage at the flanks (b) and breakout tip (c). (d)-(f) Sketch of breakout development (see text for details).

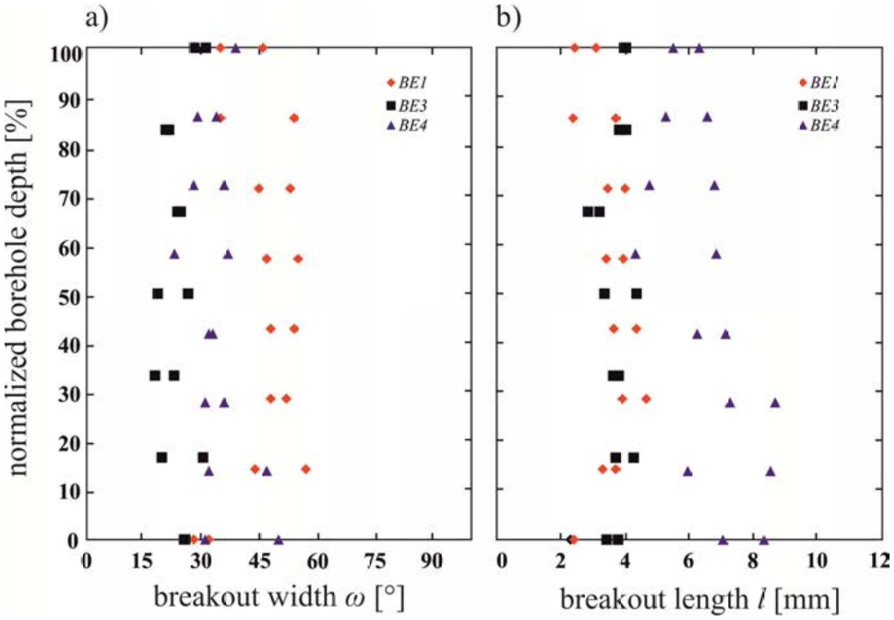

Figure 5.4 Breakout width *ω* (a) and breakout length *l* (b) obtained along the borehole from X-ray CT slices normal to the specimen axis for Bentheim sandstone.

Sample BE2 was excluded from the analysis of breakout length and width presented in Figure 5.4 because a post-deformation X-ray CT scan revealed a soft inclusion close to the borehole, which significantly affected the breakout geometry (Figure 5.5). The soft inclusion is of irregular size and consisted of brownish, very fine grained material which was flushed away during the preparation of thin-sections. With decreasing distance between the borehole axis and the soft inclusion the breakout tips shorten. The upper breakout tip deflects from its initial orientation above and below the soft inclusion, pointing towards the soft inclusion. The resulting breakout geometry would bias the measurements of breakout length and width and is not considered in the further analysis.

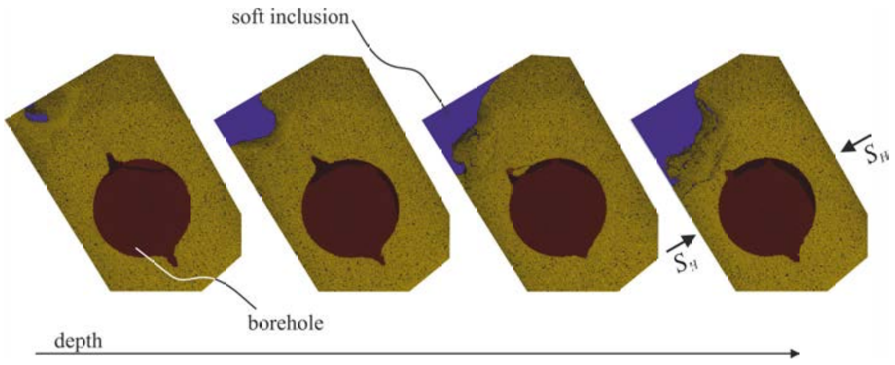

Figure 5.5 Breakout development in proximity of a soft inclusion at different positions along the borehole axis. The soft inclusion is marked in blue, the borehole is red, and the rock material is yellow.

After deformation, the cores from specimens BE2, BE3 and BE4 showed severe core disking whereas the core from BE1 was intact. The obtained disks are approximately one cm thick with flat surfaces. Core disking is an indicator for high horizontal stress differences (e.g., Song, 1998), consistent with our observation.

5.4.2 Posidonia Shale

True triaxial experiments were performed on PS samples with the borehole oriented parallel to the bedding planes. Failure type and failure stresses strongly depend on the loading direction with respect to bedding in PS, e.g. no breakout occurred if the strike of the bedding plane was oriented normal to the maximum horizontal stress (PS8), while a breakout developed for bedding planes striking parallel to the maximum horizontal stress (PS10) at the same stress conditions.

For samples deformed with the maximum horizontal stress oriented parallel to the strike of the bedding (γ = 0°, samples PS10, PS11, PS12), breakouts developed by cracks propagating along the bedding (Figure 5.6). Sometimes slabs of broken rock fragments buckle and eventually break in the middle, facilitating the creation of blocks that rotate towards the pressure-free borehole (Figure 5.6b). These blocks disconnect from the rock by tensile cracks oriented perpendicular to the bedding (see Figure 5.6a), forming spalls of blocky fragments with height limited by the spacing of the bedding planes. Fragments close to the borehole are ejected and commence/allow the fragmentation process for further slabs. Zig-zag fractures located in the remaining intact rock presumably prescribe future failure pattern. The shape of the borehole breakout is trapezoidal.

Breakout depth can vary significantly on both sides of the borehole due to the heterogeneous microstructure of the shale, i.e., spacing of the bedding planes and distribution of soft and stiff minerals, suggesting a reduction of breakout depth with decreasing differential stress, while breakout width seems to be unaffected (compare Table 5.3 and Figure 5.7).

Figure 5.6e-g illustrates the concept of trapezoidal breakout development in shale. At the onset of breakout, high shear (grey areas) and tangential (red area) stresses reactivate pre-existing bedding planes as shown in Figure 5.6e. The reactivated bedding planes open up and form slabs that buckle towards the pressure-free borehole (Figure 5.6f). The spalls get disconnected from the rock material by tensile cracks forming a breakout in the form of a trapezoid (Figure 5.6g).

In the case in which the maximum horizontal stress was applied normal to the strike of the bedding (γ = 90°, samples PS8, PS9), breakouts developed by shear failure cutting across the bedding. One breakout observed under this condition showed failure almost around the entire borehole wall (Figure 5.6d, sample PS9) and can be referred to as an "overbreak". Presumably, the onset of the breakout occurred at positions of maximum shear stress forming a double-lobbed breakout at the initial stage of loading, as observed in shales (e.g., Meier et al., 2015; Labouise and Vietor, 2013), and turned into an overbreak due to very high stresses.

For samples PS 8, PS10-12 the drill core could not be obtained. The drill core from experiment PS9 is intact and shows no indication of core disking.

In PS, breakout widths and breakout length are less clearly related to the applied stress compared to BS (Figure 5.7a and b). Width and length of the breakouts vary between 60° to 90° and 4 to 10 mm, respectively, for all samples with S_H parallel to the bedding.

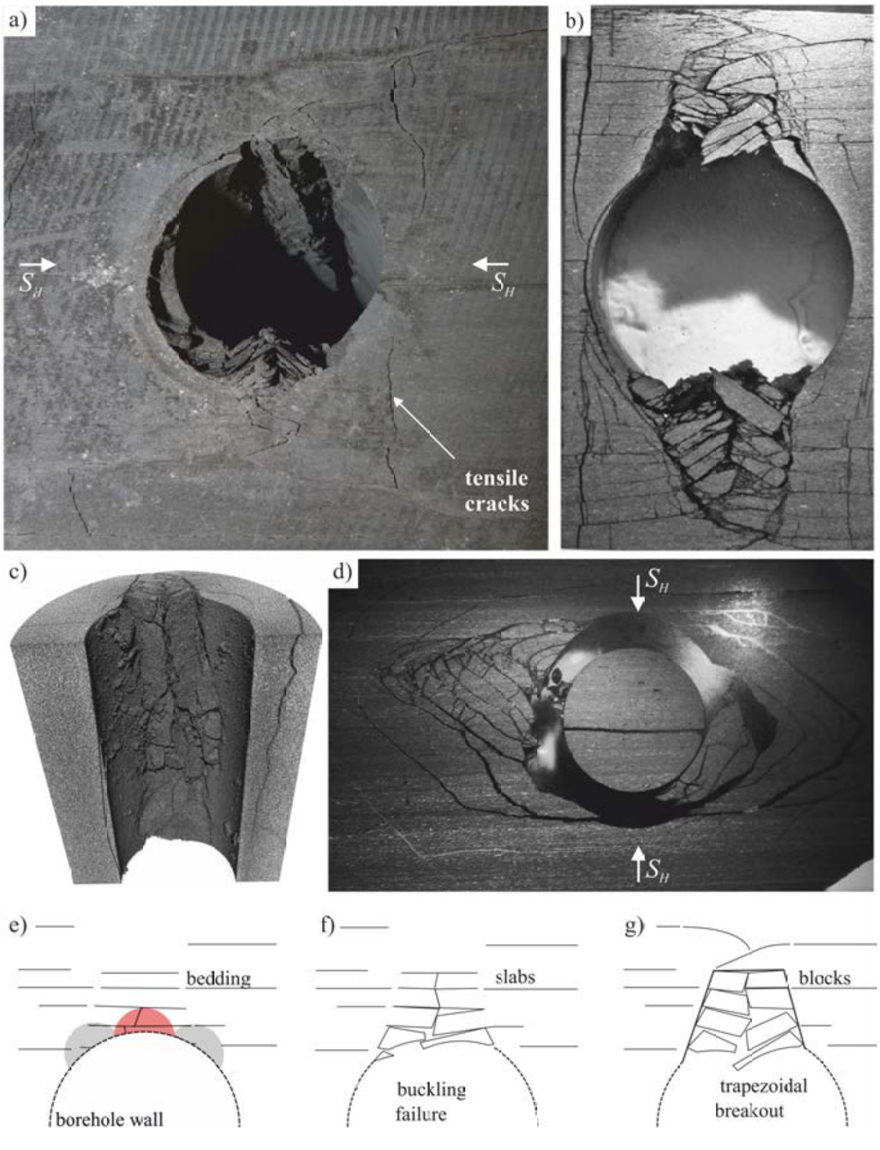

Figure 5.6 (a) Photograph, (b) thick section, and c) X-ray CT scan of deformed sample PS12. d) Thick section of a breakout formed in sample PS9. e) – g) sketch of breakout development (see text for details).

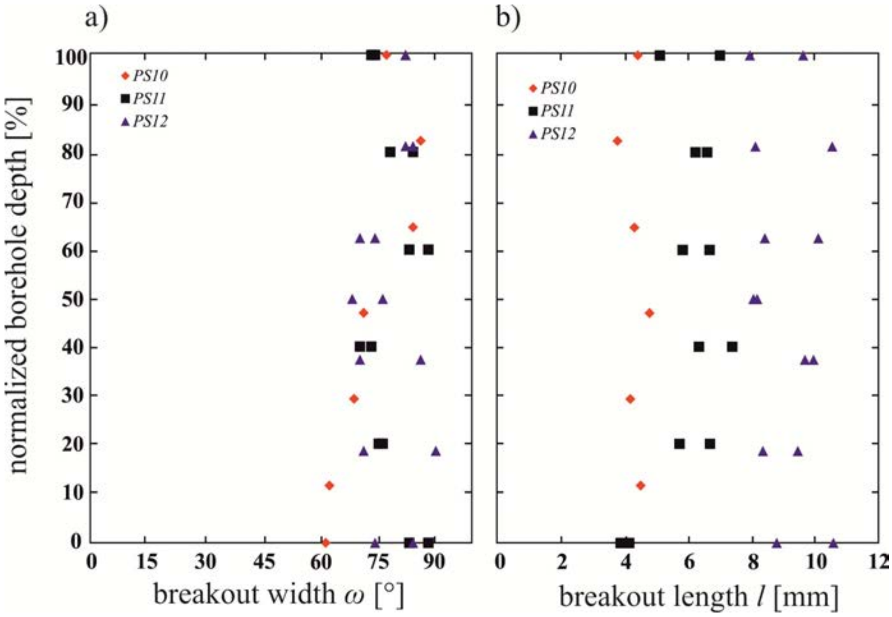

Figure 5.7 Breakout width *ω* (a) and breakout length *l* (b) obtained along the borehole from X-ray CT slices normal to the specimen axis for Posidonia shale. For sample PS10 the breakout occurred only on one side for which the breakout length and width are plotted.

5.5 Discussion

In the next subchapters the breakout shapes under conventional triaxial loading and true triaxial loading conditions are compared for the two rock types studied. Then a fracture mechanic based failure criterion is presented to describe the breakout extent and initiation stress.

5.5.1 Bentheim Sandstone

Breakouts observed in BE are similar by means of the transition from cusp- or "triangular" shaped breakouts to slot-like breakouts with increasing stress, as also observed for a variety of high porous sandstones (Haimson, 2003). The crack damage in BE loaded under conventional triaxial and true triaxial conditions, however, changes remarkably with increasing stress. While under true triaxial conditions microcracking seems to reduce with increasing breakout length and increasing stress, it is the opposite under conventional triaxial conditions where Dresen et al. (2010) mention "a triangular shape of the initial breakout" accompanied with transgranular and intragranular microcracking. At positions normal to the breakout, only a few borehole wall tangential microcracks were observed by Dresen et al. (op. cit.). Similar microstructures have been observed in various other sandstones loaded under conventional triaxial loading conditions (e.g., Cuss et al., 2003a). At true triaxial conditions microcracking is observed only at positions normal to S_H leading to cusp-shaped breakouts in BE. The absence of microcracking parallel to S_H under true triaxial conditions is related to the reduced tangential stress at those positions, while under conventional triaxial conditions the complete borehole wall is subjected to a uniform increased tangential stress.

The transition from cusp-shaped to slot-like breakouts with increasing differential stress is reported for some sandstones with porosities > 20% (e.g., Haimson, 2003). The slot-like breakout pattern is most likely due to grain crushing at the tip of the breakout and constant removal of the crushed material due to water flushing (Haimson, 2003). It is speculated that this breakout pattern may be the nucleus for the formation of compaction bands (e.g., Haimson, 2001; Haimson and Kovacich, 2003; Dresen et al., 2010). However, experiments by Haimson and Kovacich (2003) indicate that flow rates available in the laboratory are too low to transport the damaged material away. Hence, it is surprising that we did not observe the formation of compactions bands or at least intense grain damage and microcracking at the tip of the breakouts in BE deformed under true triaxial conditions as observed under conventional loading conditions.

The effect of drilling a hole while the specimen is loaded as done within this laboratory work compared to the pre-drilled hole used in conventional triaxial tests seems to be negligible since the rock was subjected to far-field stresses below the strength of the rock and no additional microcrack damage prior to drilling the hole could be initiated. Also, we did not observe drilling-related damage around the bore after unloading.

5.5.2 Posidonia Shale

Breakouts observed in Posidonia shale samples from N Germany loaded under conventional triaxial loading conditions with bedding planes sub-parallel to the borehole axis (Figure 5.8a) show similar structures as those that were produced in true triaxial tests as shown in Figure 5.8b. Shear failure along the bedding planes initiated the breakout process at four points around the borehole turning the initially circular borehole into a rectangle. At elevated stresses in conventional triaxial tests, Meier et al. (2015) found a transition from shear failure to buckling failure of blocky fragments with thicknesses related to the bedding plane spacing. The buckling of blocky fragments is also obvious under true-triaxial loading conditions as shown in Figure 5.8 and seems to be a common feature for a variety of shales independent of scale, composition, and loading conditions (Blümling et al., 2007; Labiouse and Vietor, 2013; Labiouse et al., 2014; Meier et al., 2015; Økland and Cook, 1998).

Beyond the trapezoidal breakout, zig-zag fractures cut the bedding at angle of 15° to 45° separating the rock into spalls of triangular shape. It is interesting to note that the breakout width seems to depend on the applied stress field. While conventional triaxial loading conditions seem to initiate broad breakouts with breakout width > 90°, breakout width under true triaxial loading conditions is < 90°. This may be explained by the uniform stress concentration around the borehole wall under conventional loading in comparison to the localized stress concentration under true triaxial loading conditions.

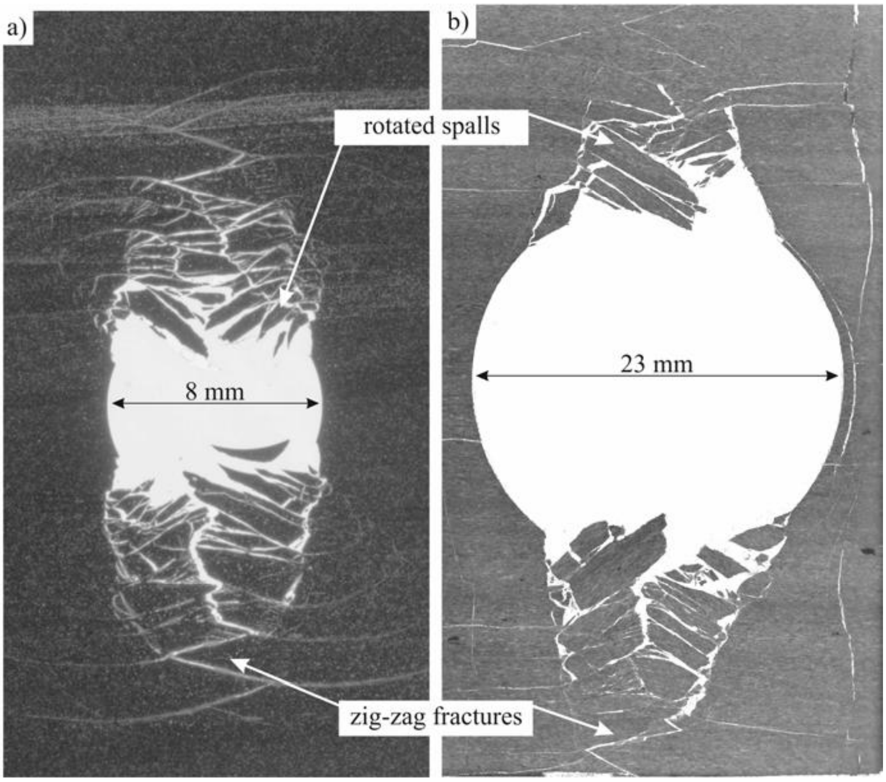

Figure 5.8 Micrographs of Posidonia shale samples with bedding sub-parallel to the borehole axis under a) conventional and b) true triaxial loading conditions. The breakout pattern shows rotated spalls due to buckling failure and zig-zag fractures beyond the trapezoidal breakout. Bedding is orientated horizontally as is the maximum horizontal stress in b).

5.5.3 Stress Field Under True-Triaxial Loading Conditions and Critical Breakout Initiation Stress

The stress field in the vicinity of a vertical borehole surrounded by a linear elastic, isotropic or TVI material, with bedding planes normal to the borehole, can be calculated in cylindrical coordinates (e.g., Jaeger et al., 2007) with the radial (σ_r), tangential (σ_θ), shear ($\sigma_{r\theta}$), and vertical (σ_z) stresses given by

$$\sigma_r = \frac{S_H + S_h}{2}\left(1 - \frac{a^2}{r^2}\right) + \frac{S_H - S_h}{2}\left(1 - 4\frac{a^2}{r^2} + 3\frac{a^4}{r^4}\right)\cos 2\theta \tag{5.1}$$

$$\sigma_\theta = \frac{S_H + S_h}{2}\left(1 + \frac{a^2}{r^2}\right) - \frac{S_H - S_h}{2}\left(1 + 3\frac{a^4}{r^4}\right)\cos 2\theta \tag{5.2}$$

$$\sigma_{r\theta} = \frac{S_H - S_h}{2}\left(1 + 2\frac{a^2}{r^2} - 3\frac{a^4}{r^4}\right)\sin 2\theta \tag{5.3}$$

$$\sigma_z = S_V \tag{5.4}$$

where *a* is the borehole radius, *r* is the radial distance from the axis of the hole oriented at an angle θ measured counter-clockwise with respect to maximum horizontal stress S_H. S_h and S_v denote the minimum horizontal and vertical stress, respectively.

The equations may be modified to include the pressure difference between the borehole mud pressure and the pore pressure in the rock and thermal stresses (see Schmitt et al., 2012 and reference therein). However, in our experiments pressure and thermal effects can be neglected since the experiments were performed at room temperature on dry samples and under drained conditions, respectively.

The stress field in TVI materials with bedding planes parallel to the borehole is more difficult to obtain analytically (e.g., Hwu, 2010; Gaede et al., 2012; Pei, 2008; Ong and Roegiers, 1993, 1996). Existing analytical solutions are limited to holes in an infinite plate and derive the stress field only at the borehole wall. Meier et al. (2015) could show numerically that the difference in the obtained stress fields between TVI Posidonia shale and an isotropic medium is less 10%, which is considered negligible in the context of this paper.

For BE, we measured a decrease of the average breakout length on both sides of the borehole with decreasing tangential stress calculated from Equation 5.2 (see Table 5.2). A linear fit to the data is presented in Figure 5.9a.

For PS, a very poor linear relationship between breakout length and tangential stress with R^2 = 0.12 was obtained (see Table 5.3, Figure 5.9b). The low correlation is possibly influenced by the varying bedding plane spacing ranging from 1 mm to 5 mm, which is in the range of the observed breakout length. Better correlation coefficients can be expected in case of greater breakout depths or significantly smaller bedding plane spacing in which case the breakout process becomes less dependent on the abundance of existing bedding planes.

Assuming that the linear relationships of breakout length and tangential stress are valid for BE and PS, the tangential stress at the onset of breakout formation can be estimated from a theoretical infinitesimal small breakout length of $l \rightarrow 0$ mm, yielding critical tangential stresses (σ_θ^*) of about 94 MPa and 132 MPa for BE and PS, respectively. However, the uncertainty in σ_θ^* is large for PS due to the low correlation coefficient.

The critical tangential stress at the onset of breakout formation can be compared for different rock types by normalizing σ_θ^* with the uniaxial compressive strength of the material (e.g., Dresen et al., 2010; Perras and Diederichs, 2016). For most isotropic rocks, this critical ratio (CR^*) is similar at given borehole diameter and increases non-linearly with decreasing borehole diameter as shown for a couple of selected rocks in Figure 5.10. With increasing borehole diameter CR^* converges against a factor of approx. 2 in laboratory experiments. For microtunnels and tunnels the ratio might decrease to a value of 1 or below (e.g., Perras and Diederichs, 2016). Normalizing the extrapolated critical tangential stresses with the measured uniaxial compressive strength (UCS_{xy} for PS) yields a critical ratio of about $CR^* = 1.90$ for BE and $CR^* = 1.86$ for PS, fitting to the trend of other sand- and limestones (Figure 5.10).

The critical ratio can be used to predict the formation of breakouts as ratios greater than CR^* induce breakouts whereas smaller ratios indicate no breakout formation. For example, in sample PS10 the breakout occurred only on one side and was rather short (Table 5.3). The ratio CR^* for PS10 is 1.83. In line with this observation, experiment PS8 a normalized tangential stress ratio of 1.63 was reached, well below CR^* and no breakouts were initiated. All samples with ratios greater than CR^* developed breakouts.

The non-linear decrease of the critical ratio with increasing borehole diameter may be fitted with a power-law regression as shown in Figure 5.10 by a solid line for BE ($CR^* = 23.68a^{-0.6}$, $R^2 = 0.96$) and a dashed line for PS ($CR^* = 12.4a^{-0.378}$, $R^2 = 0.96$).

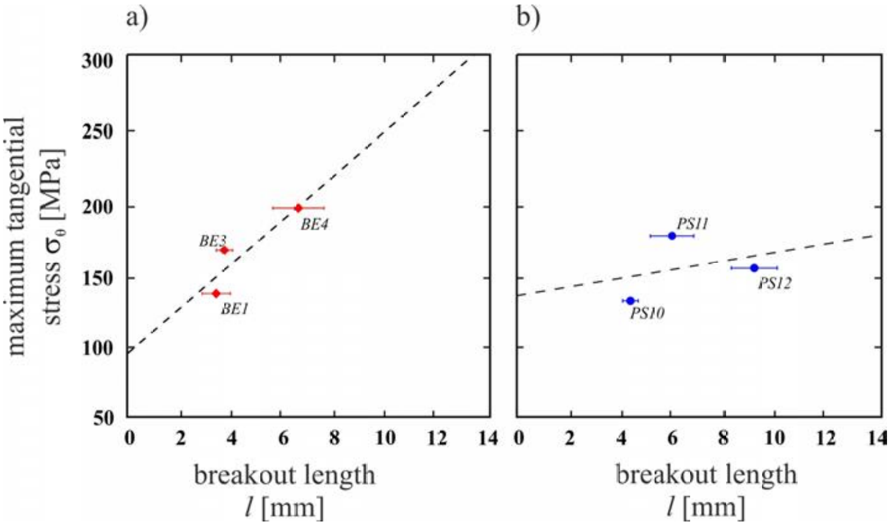

Figure 5.9 Breakout length *l* versus maximum tangential (breakout) stress at the borehole wall for a) Bentheim sandstone. The dashed lines represent linear regression fits with a correlation coefficient of $R^2 = 0.83$. The linear regression intersects the y-axis at 94 MPa and has a slope of 15.5 MPa per 1 mm breakout length. b) Posidonia shale with $\gamma = 0°$. The linear regression intersects the y-axis at 132 MPa and has a slope of 3.1 MPa per 1 mm breakout length.

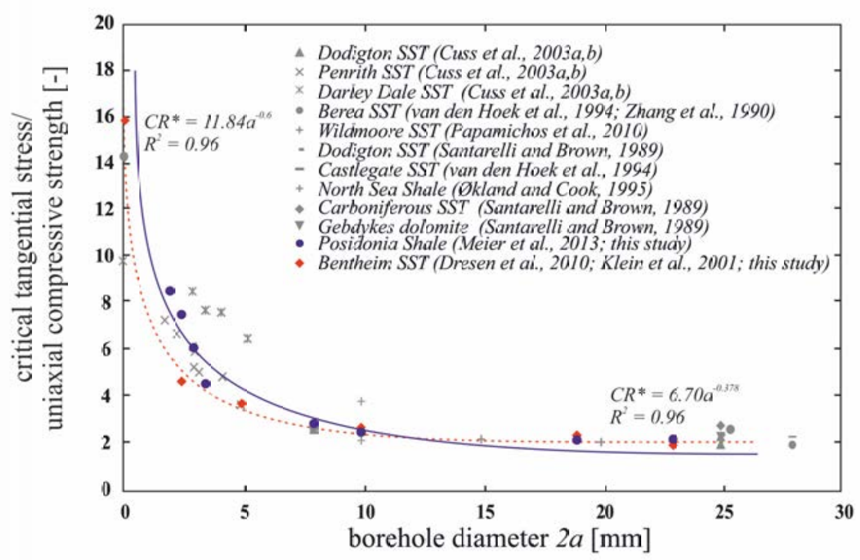

Figure 5.10 Influence of borehole diameter (2a) on breakout initiation stress normalized with the uniaxial compressive strength for various sandstones, shales and dolomite. Red dashed and blue solid lines are exponential fits for isotropic Bentheim sandstone and TVI Posidonia shale, respectively.

5.5.4 Breakout Initiation Criterion for Isotropic Bentheim Sandstone and TVI Posidonia Shale Under Conventional Loading Conditions

Dresen et al. (2010) proposed a failure criterion to describe the scale-dependent borehole breakout formation observed in BE under conventional triaxial conditions based on a fracture mechanics failure criterion (Ashby and Hallam, 1986) of the form:

$$\sigma_1 = \mathrm{K}_{\mathrm{Term}} + \mu_{\mathrm{Term}}\sigma_3 \qquad 5.5$$

with $K_{Term} = \frac{\sqrt{3}\mathrm{K}_{\mathrm{IC}}}{\left(\sqrt{1+\mu^2}-\mu\right)\sqrt{\pi c}}$ and $\mu_{Term} = \frac{\left(\sqrt{1+\mu^2}+\mu\right)}{\left(\sqrt{1+\mu^2}-\mu\right)}$.

where σ_1 and σ_3 are the maximum and minimum principal stresses, respectively, K_{IC} is the Mode I fracture toughness, μ is the internal friction coefficient, and c is the half defect length of a pre-existing initial defect. The criterion can be re-arranged to predict the critical confining pressure P^* at the onset of breakout formation under conventional triaxial conditions in thick-walled hollow cylinders ($S_v > S_H = S_h$) assuming $\sigma_1 = \sigma_\theta$ and $\sigma_3 = \sigma_r$, (Dresen et al., 2010):

$$P^* = \frac{\frac{\sqrt{3}\mathrm{K}_{\mathrm{IC}}}{\left(\sqrt{1+\mu^2}-\mu\right)\sqrt{\pi c}}}{\frac{b^2}{b^2-a^2}\left(1+\frac{a^2}{r^2}\right)-\frac{b^2}{b^2-a^2}\left(1-\frac{a^2}{r^2}\right)\frac{\left(\sqrt{1+\mu^2}+\mu\right)}{\left(\sqrt{1+\mu^2}-\mu\right)}} \qquad 5.6$$

Equation 5.6 was successfully applied to predict the onset of borehole breakouts under conventional triaxial loading for sandstones (Dresen et al., 2010) and shales (Meier et al., 2013) with varying borehole diameters.

This criterion can be extended further by relating K_{IC} with the bedding plane inclination by a linear increasing function with increasing bedding plane angle of the form

$K_{IC}(\gamma) = K_{IC,xy}+(\gamma/90)*0.65$

where γ is the angle between the maximum principal stress and strike of the bedding plane, so that $K_{IC}(0°)$ equals $K_{IC,xy}$ parallel to the bedding plane and $K_{IC}(90°)$ equals $K_{IC,z}$ normal to the bedding plane as presented in Table 5.1.

Utilizing the measured parameters given in Table 5.1, this criterion allows to determine P^* for PS with bedding plane inclinations ranging from 0° to 90°, yielding a 3D failure surface, which decreases with increasing borehole radius and decreasing bedding angle as shown in Figure 5.11a. Figure 5.11 also compiles published critical confining pressures at the onset of breakout development from thick-walled hollow cylinder experiments (Meier et al., 2013, 2015) performed on Posidonia shale from the NW and SW German Basin under conventional triaxial conditions and varying borehole diameters (Figure 5.11b) and bedding angle (Figure 5.11c). The data supports the applied failure criterion as all critical confining pressures are in very good agreement with the calculated failure criterion, indicating the formation of breakouts.

The predicted decrease of P^* with decreasing bedding plane angle is largest for small boreholes and diminishes as the borehole radius increases. Especially for small boreholes (< 1mm radius) the absolute difference in P^* drops significantly by approx. 150 MPa while the drop is only about 80 MPa at 4 mm radius (see for example Figure 5.11c) between $\gamma = 90°$ and $\gamma = 0°$.

Posidonia shale specimens from the NW German Basin (PN) follow the predicted trend of decreasing tangential stress with increasing bedding angle (red dots in Figure 5.11c), but plot above predicted by the failure criterion (Equation 5.6) at $\gamma \leq 70°$, probably due to a higher Mode I fracture toughness normal to the bedding planes. For $\gamma \rightarrow 90°$, the critical confining pressures drop slightly below the failure criterion, indicating a stronger anisotropy in K_{IC} for PN, i.e., $K_{IC,xy}$ in PN is smaller than $K_{IC,xy}$ in PS and $K_{IC,z}$ in PN is greater than $K_{IC,z}$ in PS.

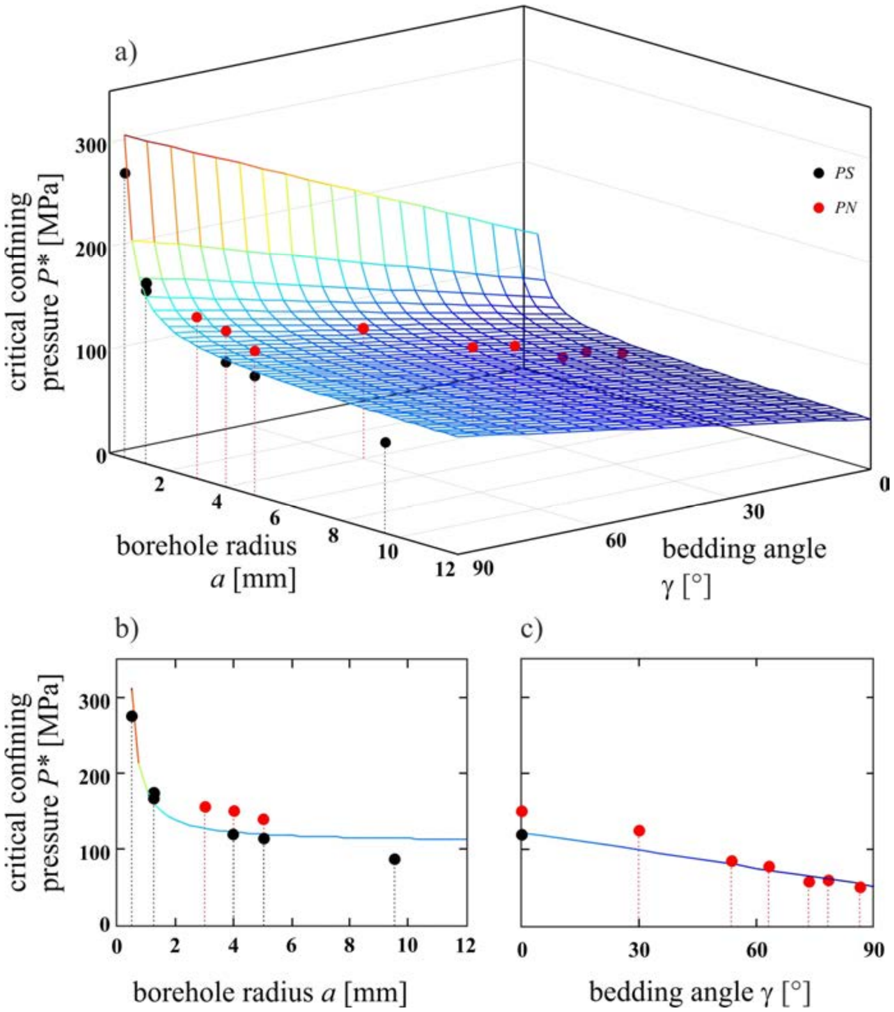

Figure 5.11 Plot of the failure surface predicted by Equation 5.6 and measurements of conventional triaxial experiments on PN (red) and PS (black) as a function of borehole radius a b) and bedding plane orientations γ (c).

5.5.5 Breakout Initiation Criterion for Isotropic Bentheim Sandstone and TVI Posidonia Shale Under True Triaxial Loading Conditions

Replacing σ_1 and σ_3 in Equation 5.5 with σ_θ and σ_r from Equation 5.1 and Equation 5.2, the failure criterion by Ashby and Hallams (op. cit.) may be modified for true triaxial loading conditions containing the two horizontal stress components, S_H and S_h. S_h may be determined in the field using hydraulic fracturing or extended leak off tests. We therefore define a critical maximum horizontal stress at the onset of breakout initiation S_H^*:

$$S_H^* = \frac{r^2[a^2(1+\mu_{Term})S_h + r^2(-2K_{Term} + S_h - S_h\mu_{Term})] + [3a^4(1+\mu_{Term}) - 4a^2r^2\mu_{Term} + (1+\mu_{Term})r^4]S_h\cos(2\theta)}{-a^2r^2(1+\mu_{Term}) + (-1+\mu_{Term})r^4 + [3a^4(1+\mu_{Term}) - 4a^2r^2\mu_{Term} + (1+\mu_{Term})r^4]\cos(2\theta)}$$

5.7

For θ = 90°, the tangential stress (σ_θ) reaches a maximum and the critical maximum horizontal stress S_H^* at the onset of breakout development reduces to

$$S_H^* = \frac{2r^4K_{Term} + (3a^4(1+\mu_{Term}) - a^2(1+5\mu_{Term})r^2 + 2r^4\mu_{Term})S_h}{3a^4(1+\mu_{Term}) + a^2(1-3\mu_{Term})r^2 + 2r^4} \qquad 5.8$$

At the borehole wall ($r = a$), Equation 5.8 reduces further to $S_H^* = (K_{Term}+S_h)/3$.

Figure 5.12 compares the critical maximum horizontal stress S_H^* versus radial distance from the borehole wall and magnitude of minimum horizontal stress for BE using Equation 5.8 for a defect size c of 180 μm for breakout initiation as observed by Dresen et al. (2010) (Figure 5.12a) with an infinitely large defect ($c \to \infty$) in Figure 5.12b. In both cases, S_H^* reaches a maximum at a radial distance of about twice the borehole radius. At larger distances from the borehole wall ($r \to \infty$), S_H^* drops to a constant value of $K_{Term}+\mu_{Term}S_h$ for small defects and to $S_H^* = \mu_{Term}S_h$ for large defects, e.g. fractures or faults. It is interesting to note that the latter condition defines the frictional equilibrium of a fault favorably oriented for slip (e.g., Zoback, 2007).

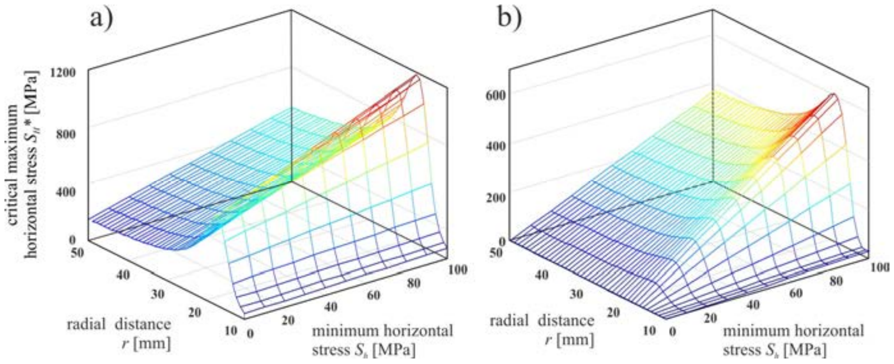

Figure 5.12 Critical maximum horizontal stress S_H^* versus radial distance r and minimum horizontal stress S_h for a half defect size c of 180 μm a) and an infinite defect size b).

For the calculation of breakout initiation stresses in BE, we assume a minimum distance from the borehole wall $\Delta r = (r\text{-}a) = 0.185$ mm (Dresen et al., 2010). Using fracture toughness, elastic parameters and defect size for BE as listed in Table 5.1, we obtain a decrease in S_H^* with increasing wellbore radius and decreasing horizontal stress S_h (Figure 5.13). For comparison we also plotted measured data for Bentheim sandstone from conventional and true triaxial tests (Dresen et al., 2010, this study). The measured and predicted failure data are in very good agreement for both isostatic ($S_H = S_h$, blacks dots) and non-isostatic conditions (red dots).

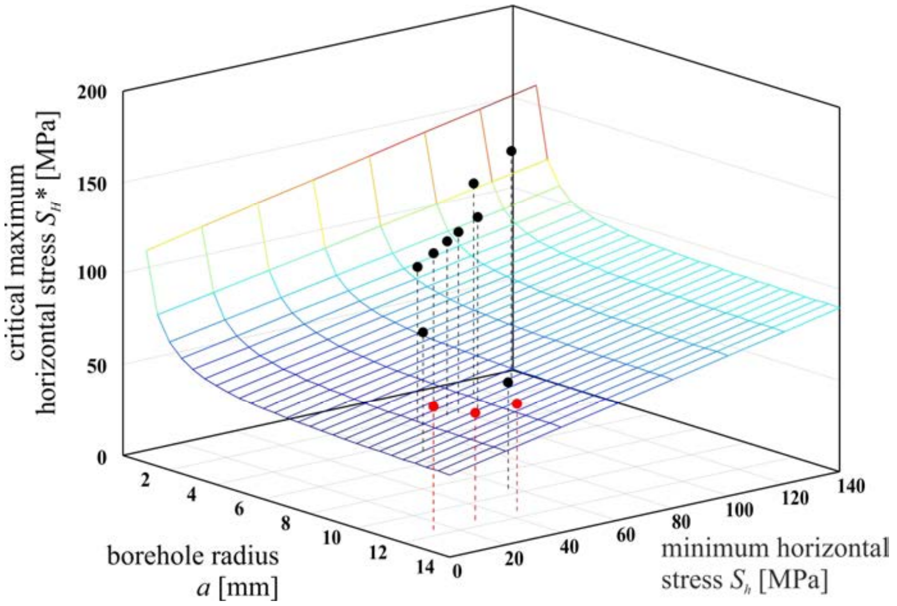

Figure 5.13 Critical maximum horizontal stress S_H^* as a function of borehole radius a and minimum horizontal stress S_h for BE. Black dots represent critical stresses for conventional triaxial loading (Dresen et al., 2010). Red dots represent true triaxial experiments from this study.

Similar plots have been created for PS based on the parameters listed in Table 5.1 with $\gamma = 0°$ ($K_{IC,xy}$) (Figure 5.14a) and $\gamma = 90°$ ($K_{IC,z}$) (Figure 5.14b). We find a very good agreement between the failure surface and critical borehole breakout stresses measured in conventional tests (black dots, Meier et al., 2013; 2014) and true triaxial tests (red dots, this study). The lowermost red point in Figure 5.14b shows the stress state, for which no borehole breakout occurred in this specific experiment.

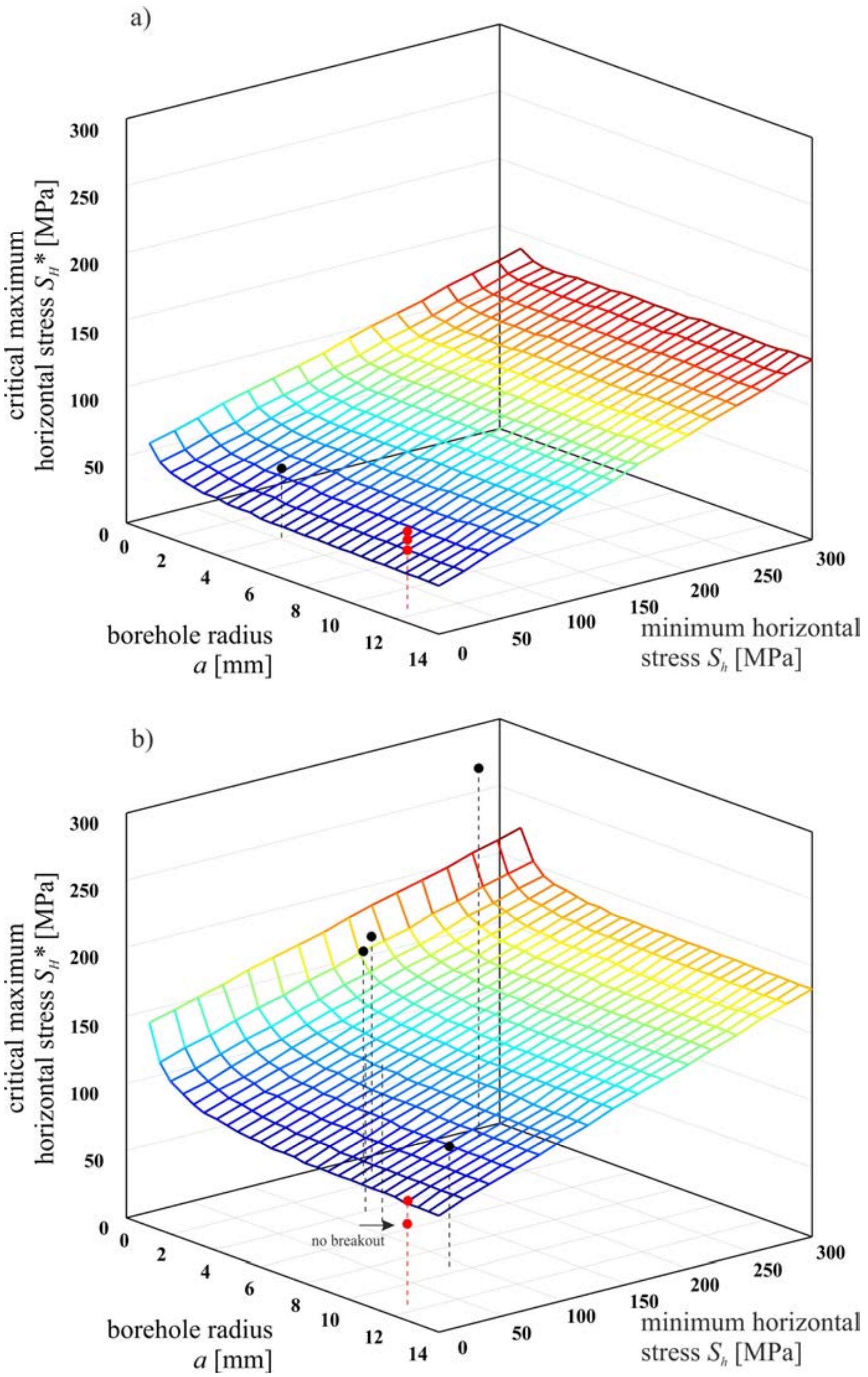

Figure 5.14 Critical maximum horizontal stress S_H^* as a function of borehole radius a and minimum horizontal stress S_h for PS with bedding angle a) $\gamma = 0°$ and b) $\gamma = 90°$. Black dots represent critical stress taken from conventional triaxial experiments (Meier et al., 2013, 2014). Red dots represent true triaxial experiments from this study.

5.5.6 Estimation of the Extent of Borehole Breakouts

The width of the breakout may be estimated graphically from Equation 5.7 again assuming that wellbore failure occurs where $S_H = S_H^*$. Figure 5.15 shows the predicted S_H^* distribution for BE (Figure 5.15a) and PS (Figure 5.15b) for S_h = 20MPa. S_H^* is lowest and increases with increasing distance from the borehole wall until reaching a local maximum at about twice the borehole radius as described in the previous section. This agrees with our observation that breakouts initiate close to the borehole wall and subsequently propagate into the rock. Values of S_H^* exceeding 1000 MPa or smaller than S_h = 20 MPa are clipped and marked in red. For BE, the angular width of the breakouts reaches a minimum at a radial distance of about twice the borehole radius (Figure 5.15a), while PS shows a broader width at the same distance (Figure 5.15b). With further increasing distance from the local peak, S_H^* decreases and the angular range of low S_H^* values widens again, approaching $S_H^* = K_{Term}+\mu_{Term}S_h$ for $\theta = 90°$.

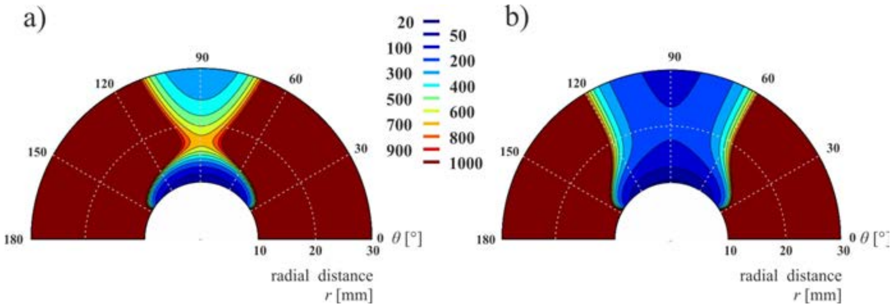

Figure 5.15 Maximum critical horizontal stress S_H^* for (a) BE and (b) PS with S_h = 20MPa. Red domain indicates stresses of S_H > 1000 MPa or $S_H < S_h$. See text for details.

5.6 Conclusions

True triaxial deformation experiments on isotropic Bentheim sandstone and transverse isotropic Posidonia shale developed borehole breakouts. The breakouts initiated at stresses comparable to conventional triaxial loading conditions. The patterns of the breakouts depend on the rock type and also show similarities with breakouts produced at conventional triaxial loading conditions, i.e., slot-like breakouts in Bentheim sandstone and trapezoidal breakouts in Posidonia shale if bedding planes are oriented parallel to the borehole axis and maximum horizontal stress. Therefore, it can be concluded that both loading configurations can be used to study the breakout development. This is further supported as samples exposed to true triaxial loading conditions initiated breakouts at critical stress to uniaxial compressive strength ratios that are in excellent agreement to conventional triaxial experiments.

A fracture mechanics based failure criterion was extended from conventional loading conditions to true triaxial loading conditions to accommodate the influence of bedding planes and borehole radius. The criterion is fit to forecast the initiation of borehole breakouts under true and conventional loading conditions. The criterion predicts breakout initiation stresses in very good agreement to measured breakout stresses for BE and PS under conventional and true triaxial loading conditions.

ACKNOWLEDGMENTS

Peter Sobol and Neil Lord (both UWM) are thanked for their hands-on introduction to the true-triaxial testing machine and for boosting the morale during lunch breaks. The authors would also like to thank Brian Hess (UWM) and Stefan Gehrmann (GFZ) for excellent job in specimen handling and preparation. Michelle Szabo (UWM) is thanked for her strong nerves in getting the rock samples through the U.S. Customs. The colleagues at geomecon GmbH are thanked for fruitful discussions.

6 GENERAL CONCLUSIONS

The main objective of this thesis is to improve the understanding of borehole related instabilities in unconventional oil and gas shales. Posidonia shale from northern and southern Germany is chosen for this purpose as the shale is considered to be the most prolific source rock in Europe (Littke et al., 2011) and a potential target for unconventional oil and gas production (Andruleit et al., 2012). Several petrophysical and geomechanical experiments have been conducted on the shale to characterize its composition, porosity, strength, and elastic properties subsequently. Afterwards, the development of borehole breakouts was studied by pressurizing thick-walled hollow cylinders with varying borehole diameter and bedding plane orientation until formation of borehole breakouts. At last, a series of true-triaxial experiments with the maximum horizontal stress orientated normal and parallel to the bedding planes have been performed to gain insight into the breakout formation under in situ conditions. All deformed specimen have been analyzed by means of X-ray CT scans, thick-, and thin sections. Latter have been studied under scanning electron microscopy or binoculars. The stress field in the specimens has been calculated analytically and numerically to take the variable specimen geometry and the transverse isotropic nature of the shale into account.

In the following section the questions which were formulated in **Chapter 1** will be discussed and answered synoptically in the light of the results from each contribution presented in **Chapter 2**, **3**, **4**, and **5**.

1) What are the geomechanical properties controlling borehole instabilities in unconventional shales under in-situ conditions?

Borehole breakouts develop in case the stress concentration in the vicinity of the borehole exceeds the strength of the rock. This principle holds true under each of the applied laboratory conditions, i.e., conventional and true-triaxial loading conditions, for Posidonia shale, too. However, the stress concentration and the strength around the borehole might differ from isotropic rocks and might lead to wrong assumption of the stress concentration or strength in case the vector normal to the bedding planes of the shale is not aligned with the borehole axis or the stress field tensor at the borehole wall. For latter case, the shale needs to be treated as anisotropic. In the particular case of Posidonia shale, it could be shown that the shale can be regarded as transverse isotropic, meaning that the material properties within the bedding plane are homogeneous but differ across them.

The stress field around a borehole in a transverse isotropic material, such as Posidonia shale, is a function of the elastic properties of the rock and the acting far field stress. The theory behind the stress concentration in transverse isotropic rocks is summarized among others by Pei (2009). Within the context of this study, the stress field acting in the specimen was calculated numerically as presented in **Chapter 4** since the analytical solutions for transverse isotropic materials are only valid at the borehole wall and for a hole located in an infinite plate, which does not reflect the laboratory conditions.

For transverse isotropic Posidonia shale, the difference between the stress field calculated for isotropic and transverse isotropic rocks is minor; for example the maximum tangential stress is up to 10% higher than in an isotropic rock. This is in line with Blümling (1986), who concluded that ratios in the Young's modulus, measured in bedding normal and parallel direction, smaller than three will not result in significant deviations in the stress field around a bore between isotropic and transverse isotropic materials. Only a few unconventional shales with clay and kerogen volumes > 50% seem to show such ratio (Sone and Zoback, 2013). At ambient conditions, Posidonia shale form northern or southern Germany show ratios in the Young's modulus below a factor of two. It can hence be concluded that the elastic anisotropy does not significantly affect the breakout process in Posidonia shale and that the shale can be treated as isotropic from an elastic point of view irrespective of bedding plane angle.

The influence of confining pressure and temperature, among other influencing parameters such as water content, strain rate or composition, on the strength was investigated in **Chapter 2.1** for a variety of European black shales and Posidonia shale in particular. The presented data shows consistently that Posidonia shale weakens with increasing temperature and decreasing confining stress. While drilling a borehole, the rock adjacent to the hole is quickly relieved from its initial confining pressure while the temperature remains high. It can be concluded that both effects will considerably reduce the strength of the rock around the borehole and enhance the formation of borehole breakouts.

Since, geomechanical properties are sometimes hard to obtain due to the lack of sample material or difficulties in specimen preparation, an effort was made in **Chapter 2.1** to link the geomechanical parameters with petrophysical properties or mineralogical composition, which can both be derived from plugs or drill cuttings. The correlations work best for temperature and pressure regimes in which the shales behave brittle, i.e., confinement < 100 MPa and temperature < 100°C. In case of elevated temperature and pressure conditions, the shale behavior transitions into semibrittle and correlation trends between the strength and elastic properties with petrophysical parameters and compositions are more equivocal. From the correlations it can be concluded that the strength and the stiffness of Posidonia shale increase with decreasing porosity since the mineralogical composition is very similar between the two tested Posidonia shales. Hence, the lower porous Posidonia shale is less prone to the formation of borehole breakouts, which was supported by the higher tangential stress necessary to induce them.

It can be concluded that the development of borehole breakouts in unconventional Posidonia shale is primarily due to the complex interplay of the acting reservoir conditions, the strength of the rock as a function of bedding plane orientation, porosity, temperature and confining pressure, but only secondarily influenced by its anisotropy in elastic properties.

While the geomechanical factors and in-situ conditions of the shale reservoir cannot be controlled to suppress the formation of breakouts, the well might be planned and designed to achieve this goal, leading on to the question:

2) How can borehole stability be assured in unconventional shales?

Generally, the risk for borehole breakouts can be reduced if the well is drilled in a direction in which the differential stress acting in a plane normal to the borehole axis is reduced. A couple of preferred horizontal drilling direction for different stress regimes can easily be obtained by this approach for isotropic formations (e.g., Addis et al., 1993). For example, a horizontal borehole drilled in a normal faulting regime should be drilled towards the direction of the smallest horizontal stress to reduce the differential stress in the plane normal to the borehole axis. This advice does not hold true for shale formations, where most of the drilling problems are encountered during angle built-up, doglegs or in sub- to horizontal sections of the well (e.g., Blümling, 1986; Økland and Cook, 1998; Ottesen, 2010).

As pointed out in **Chapter 5**, the stress necessary to induce breakout reduces linearly with increasing α (angle between the bedding plane normal and the borehole axis), so that the lowest stress is required for breakout formation when drilling parallel to the bedding in Posidonia shale. This can be explained by the fact that the lowest strength, i.e., bedding parallel uniaxial compressive strength, of the shale gets exposed simultaneously with increasing angle built-up or by a plane of weakness that rotates from an unfavorable orientation towards a favorable orientation for slip with increasing angle built-up. Both concepts have been successfully analyzed in **Chapter 5**.

This observation could be manifested under true-triaxial loading, presented in **Chapter 6**, too. In particular, specimens subjected to the same stress field initiated breakouts if the strike of the bedding planes was parallel to the maximum tangential stress, while breakouts did not occur in experiments with the strike of the bedding planes normal to the maximum horizontal stress. This is mainly due to the anisotropy in strength, which is largest when drilling parallel to the bedding. Hence, the recommendation for maintaining stable horizontal wells penetrating shale formations should be extended in a way that the maximum tangential stress should be always oriented normal to the strike of the bedding.

Borehole stability can further be tested by increasing the angle of attack slowly, i.e., large borehole curvature, in order to test the strength of the formation. As soon as breakouts form at a certain angle, a prognosis can be made about the severity of the breakout if angle built up is commenced. A maximum angle of attack can then be formulated to avoid severe borehole breakouts as was also suggested by Økland and Cook (1998). However, since, horizontal drilling is required to increase the interaction of the well with the unconventional formation, another key parameter in assuring borehole stability lies in the diameter of the well. Experiments performed under conventional triaxial and true-triaxial loading conditions show a non-linear reduction of the stress required to induce breakouts with increasing hole size (**Chapter 4**). This concept can be used to shift to smaller borehole diameters when drilling parallel to the bedding or before angle built-up. Similar approaches have been already tested in the oil and gas industry by means of fishbone drilling (e.g., Priskila 2014).

Based on the research presented in this thesis, a fracture mechanic based failure criterion has been developed and presented in **Chapter 6**, which predicts the critical maximum horizontal stress necessary to induce borehole breakout for varying borehole diameters, bedding plane orientations and stress fields. It is based on a linear decrease of the Mode I fracture toughness observed in Posidonia shale and assumes that the breakout process initiates at a small distance from the borehole wall within the rock. With the help of this criterion the influence of borehole diameter, bedding plane orientation and stress field can be evaluate to successfully assure borehole stability in Posidonia shale.

3) Can breakouts in unconventional shales be used to derive the orientation and magnitude of the maximum horizontal stress?

The orientation of the maximum horizontal stress can be derived in a vertical borehole penetrating unconventional shales, if the bedding planes are oriented normal to the borehole axis and the stress difference between the horizontal stresses is significant. In this case, the shale can be treated isotropic and the induced breakout will be formed by intersecting shear failure planes at positions normal to the maximum horizontal stress that will form a clear cusp-shaped breakout.

7 OUTLOOK

Within the context of this work, all experiments on the development of borehole breakouts have been performed by neglecting the influence of temperature and pore pressure, which are important in-situ reservoir parameters, affecting the strength and elastic properties of Posidonia shale. The limitation in the testing parameters arose partly in the difficulty to handle sample material, which is prone to the uptake of water into the bedding planes and the related disintegration of them, and partly in the exclusiveness of the testing machines to apply only stress conditions under conventional and true-triaxial loading conditions.

However, **Chapter 2** highlights the importance of these reservoir parameters on the strength and elastic properties of Posidonia shale. Increases in temperature and pressure have severe impacts on the load bearing capacity of Posidonia shale and might therefore significantly alter the results presented here. The same applies to the variation in elastic parameters with changing pressure and temperature conditions, which might further affect the stress distribution around the hole in a stronger manner than calculated under ambient pore pressure and temperature conditions. Future laboratory investigations on borehole stability should therefore focus on the development of borehole breakouts under in-situ stress, temperature and pressure conditions.

Nowadays numerical software packages based on the eXtended Finite Element Method (X-FEM) model allow the simulation of the fracturing process (Backers, 2010) during the formation of hydraulic fractures (Stöckhert et al., 2015) or borehole breakouts (e.g., Backers et al., 2012). Within the context of this research, the X-FEM based software package roxol^{TM} has been successfully employed to model the experiments performed under various loading rates and bedding plane orientations (Meier et al., 2015b). The modeled fracture patterns match the observed fracture pattern in the laboratory experiments and allow the estimation of the extent of borehole breakouts in transverse isotropic shale formations. By reactivating pre-existing bedding planes and the propagation of new fractures from the borehole wall into the rock this modelling approach incorporates the existing structural anisotropy in Posidonia shale and thereby yields a deeper understanding of the fragmentation process during the breakout formation. Future numerical modelling should try to incorporate the scale-effect by incorporating the fracture mechanic based failure criterion presented in **Chapter 6**.

8 REFERENCES

A

Aadnoy, B.S., Ong, S., 2003. Introduction to special issue on Borehole Stability. J. Pet. Sci. Eng.; 38(3-4): 79-82.

Aadnoy, B.S., 1989. Stresses around horizontal boreholes drilled in sedimentary rocks. J. Pet. Sci. Eng.; 2(4): 349-360.

Addis, M.A., Barton, N.R., Bandis, S.C., Henry, J.P., 1990. Laboratory studies on the stability of vertical and deviated boreholes. SPE J;20406:19–30.

Addis, M.A., Wu, B., 1993. The Role of the Intermediate principal stress in wellbore stability studies: evidence from hollow cylinder tests. Int. J. Rock Mech. Min. Sci.; 30(7):1027–30.

Addis, T., Last, N., Boulter, D., Roca-Ramisa, L., Plumb, D., 1993. The quest for borehole stability in the Cusiana field, Colombia. Oilfield Rev 1993; April/July: 33-43.

Al-Ajmi, A.M., Zimmerman, R.W., 2009. A new well path optimization model for increased mechanical borehole stability. J. Pet. Sci. Eng.; 69(1-2):53–62.

Allen, F., Tooms, P., Conran, G., Lesso, B., Van de Slijke, P., 1997. Extended-reach drilling: breaking the 10-km Barrier. Oilfield Rev 1997; Winter: 32–47.

Allix, P., Burnham, A., Fowler, H., Herron, M., Kleinberg, R., Symington, B., 2010. Coaxing oil from shale. Oilfield Rev 2010/2011; Winter: 4–15.

Amadei, B., 1983. Lecture notes in engineering, 2 series volume: rock anisotropy and the theory of stress measurements. Springer, Berlin Heidelberg.

Amadei, B., Stephansson, O., 1997. Rock stress and its measurement. *Springer*.

Andruleit, H., Bahr, A., Bönnemann, C., Erbacher, J., Franke, D., Gerling, J.P., Gestermann, N., Himmelsbach, T., Kosinowski, M., Krug, S., Pierau, R., Pletsch, T., Rogalla, U., Schlömer, S., NiKo-Projekt Team, 2012. Abschätzung des Erdgaspotenzials aus dichten Tongesteinen (Schiefergas) in Deutschland. Hannover: Bundesanstalt für Rohstoffe (BGR), Fachbereich B1.3 - „Geologie der Energierohstoffe, Polargeologie“.

Aoki, T., Tan, C.P., Bamford, W.E., 1993. Effects of deformation and strength anisotropy on borehole failure in saturated shales. Int. J. Rock Mech. Min. Sci. Geomech. Abstr.; 30(7): 1031-1034.

Ashby, M., Hallam, S., 1986. The failure of brittle solids containing small cracks under compressive stress states. Acta Metallugica; 34(3):497–510.

Ask, D., Ask, M.V.S., 2007. Detection of potential borehole breakouts in boreholes KFM01A and KFM01B. SKB Report P-07-235 Forsmark site investigation.

Atkinson, C., Bradford, I., 2002. Effect of inhomogeneous rock properties on the stability of wellbores. In: Karihaloo BL (ed) IUTAM symposium on analytical and computational fracture mechanics of non-homogeneous material. Kluwer Academic Publishers, pp 95-104.

B

Backers, T., Dresen, G., Rybacki, E., Stephansson, O., 2004. New data on mode II fracture toughness of rock from the punch-through shear test. Int. J. Rock Mech. Min. Sci.; 41 (S1), 2–7.

Backers, T., 2010. Applications of fracture mechanics numerical modelling in rock engineering. first break; 28(3): 13 - 22.

Backers, T., Gruehser, C., Meier, T., Dresen, G., 2012. Fracture Pattern of Borehole Breakouts in Shale - Comparison of Physical and Numerical Experiments. EAGE. Copenhagen, Denmark.

Barton, C., Zoback, M.D., Burns, K.L., 1988. In-situ stress orientation and magnitude at the Fenton Geothermal Site, New Mexico, determined from wellbore breakouts. Geophys. Res. Letts; 15(5):467–70.

Barzegar, A.R., Oades, J.M., Rengasamy, P., Murray, R.S., 1995. Tensile strength of dry, remoulded soils as affected by properties of the clay fraction. Geoderma; 65(1-2): 93–108.

Bell, J.S., Gough, D.I., 1979. Northeast-southwest compressive stress in Alberta evidence from oil wells. Earth and Planetary Science Letters; 45(2):475-482.

Bennetzen, B., Fuller, J., Isevcan, E., Krepp, T., Meehan, R., Mohammed, N., Poupeau, J-F., Sonowal, K., 2010. Extended-reach wells. Oilfield Rev. 2010; 22(3):4–15.

Berard, T., Liu, Q., Dubost, F.X., Jing, B., 2012. A Screening Process for Shale Gas Prospecting. SPE Paper 154736: 19.

Bernard, S., Horsfield, B., 2014. Thermal maturation of gas shale systems. Annu. Rev. Earth Planet. Sci.; 42: 635–651.

Bernard, S., Wirth, R., Schreiber, A., Bowen, L., Aplin, A.C., Mathia, E.J., Schulz, H.M., Horsfield, B., 2013. FIB-SEM and TEM investigations of an organic-rich shale maturation series from the lower Toarcian Posidonia shale, Germany: nanoscale pore system and fluid–rock interactions. In: Camp, W., Diaz, E., Wawak, B. (Eds.), Electron Microscopy of Shale Hydrocarbon Reservoirs: AAPG Memoir 102, pp. 53–66.

Bieniawski, Z.T., Bernede, M.J., 1979a. Suggested methods for determining the uniaxial compressive strength and deformability of rock materials: Part 1. Suggested method for determination of the uniaxial compressive strength of rock materials. Int. J. Rock Mech. Min. Sci.; 16(2):137.

Bieniawski, Z.T., Bernede, M.J., 1979b. Suggested methods for determining the uniaxial compressive strength and deformability of rock materials: Part 2. Suggested method for determining deformability of rock materials in uniaxial compression. Int. J. Rock Mech. Min. Sci.; 16(2):138–40.

Bieniawski, Z.T., Hawkes, I., 1978. Suggested methods for determining tensile strength of rock materials. Int. J. Rock Mech. Min. Sci. Geomech. Abstr.; 15: 99–103.

Birchwood, R., Noeth, S., 2012. Horizontal stress contrast in the shallow marine sediments of the Gulf of Mexico sites Walker Ridge 313 and Atwater Valley 13 and 14—geological observations, effects on wellbore stability, and implications for drilling. Mar. Pet. Geol.; 34(1):186-208.

Bjorlykke, K., 2010. Petroleum Geoscience: From Sedimentary Environments to Rock Physics. Springer, Berlin, p. 508.

Blümling, P., 1986. In-situ-Spannungsmessung in Tiefbohrungen mit Hilfe von Bohrlochrandausbrnchen und die Spannungsverteilung in der Kruste Mitteleuropas und Australiens. Doctoral dissertation. University of Karlsruhe.

Blümling, P., Bernier, F., Lebon, P., Martin, C.D., 2007. The excavation damaged zone in clay formations time-dependent behaviour and influence on performance assessment. Phys Chem Earth Parts A/B/C 32(8-14):588-599.

Boyer, C., Kieschnick, J., Suarez-Rivera, R., Lewis, R.E., Waters, G., 2006. Producing gas from its source. Oilfield Rev 2006; Autumn: 36–49.

Brady, B.H.G., Brown, E. T. (2006). Rock Mechanics for underground mining (3rd edition). *Springer.*

Britt, L.K., Schoeffler, J., 2009. The Geomechanics of a Shale Play: What Makes a Shale Prospective. SPE Paper 125525: 9.

C

Cander, H., 2012. What are unconventional resources? A simple definition using viscosity and permeability. Search and Discovery Article 80217.

Carranza-Torres, C., Fairhurst, C., 1999. The elasto-plastic response of underground excavations in rock masses that satisfy the Hoek–Brown failure criterion. Int. J. Rock Mech. Min. Sci.; 36(6):777–809.

Chang, C., Zoback, M.D., 2009. Viscous creep in room-dried unconsolidated Gulf of Mexico shale (I): experimental results. J. Pet. Sci. Eng.; 69(3-4):239–246.

Chang, C., Zoback, M.D., Khaksar, A., 2006. Empirical relations between rock strength and physical properties in sedimentary rocks. J. Pet. Sci. Eng.; 51(3-4):223–227.

Charles, P.A., 1997.Rock mechanics: petroleum applications. *Editions Technip.*

Chenevert, M.E., Gatlin, C., 1965. Mechanical anisotropies of laminated sedimentary rocks. SPE J 890-PA; 5(1):67-77.

Chong, K.P., Boresi, A.P., 1990. Strain rate dependent mechanical properties of New Albany reference shale. Int. J. Rock Mech. Min. Sci. Geomech. Abstr.; 27(3): 199–205.

Chong, K.P., Hoyt, P.M., Smith, J.W., Paulsen, B.Y., 1980. Effects of strain rate on oil shale fracturing. Int. J. Rock Mech. Min. Sci. Geomech. Abstr.; 17(1): 35–43.

Chong, K.P., Smith, J.W., 1984. Mechanics of oil shale. *Elsevier.*

Cogan, J., 1976. Triaxial creep test of Opohonga limestone and Ophir shale. Int. J. Rock Mech. Min. Sci. Geomech. Abstr.; 13(1):1–10.

Conti, J.J., Holtberg, P.D., Diefenderfer, J.R., Napolitano, S.A., Schaal, A.M., Turnure, J.T., Westfall, L.D., 2015. Annual Energy Outlook 2015 with projections to 2040. Washington (USA): U.S. Energy Information Administration (EIA), Office of Integrated and International Energy Analysis, U.S. Department of Energy.

Covey-Crump, S.J., Schofiels, P.F., Stretton, I.C., Daymond, M.R., Knight, K.S., Tant, J., 2013. Monitoring in situ stress/strain behavior during plastic yielding in polymineralic rocks using neutron diffraction. J. Struct. Geol.; 47, 36–51.

Cuisiat, F.D.E, Haimson, B.C., 1992. Scale effects in rock mass stress measurements. Int. J. Rock Mech. Min. Sci.; 29(2):99–117.

Cuss, R.J., Rutter, E.H., Holloway, R.F., 2003. Experimental observations of the mechanics of borehole failure in porous sandstone. Int. J. Rock Mech. Min. Sci.; 40(5):747–61.

Cuss, R.J., Rutter, E.H., Holloway, R.F., 2003. The application of critical state soil mechanics to the mechanical behaviour of porous sandstones. Int. J. Rock Mech. Min. Sci.; 40(6):847–62.

D

Daemen, J.J.K., 1983. Slip zones for discontinuities parallel to circular tunnels or shafts. Int. J. Rock Mech. Min. Sci. Geomech. Abstr.; 20(3):135-148.

Davies, R. J., Almond, S., Ward, R. S., Jackson, R. B., Adams, C., Worrall, F., Herringshaw, L.G., Gluyas, J.G., Whitehead, M. A., 2014. Oil and gas wells and their integrity: Implications for shale and unconventional resource exploitation. Marine and Petroleum Geology, 56, 239–254.

Dewhurst, D.N., Siggins, A.F., 2006. Impact of fabric, microcracks and stress field on shale anisotropy. Geophys. J. Int.; 165(1):135-148.

Donath, F.A., 1961. Experimental study of shear failure in anisotropic rocks. Geol. Soc. Am. Bull.; 72(6):985-990.

Dresen, G., Stanchits, S., Rybacki, E., 2010. Borehole breakout evolution through acoustic emission location analysis. Int. J. Rock Mech. Min. Sci.; 47(3):426-435.

Dusseault, M.B., Bruno, M.S., Barrera, J., 2001. Casing shear: causes, cases, cures. In: SPE international. Oil and gas conference and exhibition, pp 98-107.

E

Economides, M.J., Nolte, K.N., 2000. Reservoir Stimulation. 3rd ed. *Wiley*.

EIA, 2015. Technically Recoverable Shale Oil and Shale Gas Resources: An Assessment of 137 Shale Formations in 41 Countries Outside the United States. Washington (USA): U.S. Energy Information Administration (EIA), Office of Independent Statistics & Analysis, U.S. Department of Energy.

Eseme, E., Littke, R., Krooss, B. M., 2006. Factors controlling the thermo-mechanical deformation of oil shales: Implications for compaction of mudstones and exploitation. Marine and Petroleum Geology; 23(7): 715–734.

Evans, B., Fredrich, J.T., Wong, T.F., 1990. The brittle–ductile transition in rocks: recent experimental and theoretical progress. In: Duba, A.G., Durham, W.B., Handin, J.W., Wang, H.F. (Eds.), The Brittle–ductile Transition in Rocks: The Heard volume 56. AGU Geophysical Monograph, Washington, pp. 1–20.

Evans, B., Kohlstedt, D.L., 1995. Rheology of Rocks. In: Ahrens, T.J. (Ed.), Rock Physics and Phase Relations: A Handbook of Physical Constants. AGU Reference Shelf, Washington, pp. 148–165.

F

Fjaer, E., Holt, R.M., Horsrud, P., Raaen, A.M., Risnes, R., 2008. Petroleum related rock mechanics. 2nd ed. *Elsevier.*

Füchtbauer, H., 1988. Sedimente und Sedimentgesteine. *E. Schweizerbart'sche Verlagsbuchhandlung.*

Fuller, J., Meehan, R., 2010. Extended-reach wells. Oilfield Rev 2010; Autumn: 4–15.

G

Gabrielsen, G.K., Stenebråten, J.F., Nes, O-M., Holt, R.M., Horsrud, P., 2010. Use of modified hollow cylinder test in laboratory for simulation of downhole drilling condition in shale. SPE J;131356:1–14.

Gaede, O., Karpfinger, F., Jocker, J., Prioul, R., 2012. Comparison between analytical and 3D finite element solutions for borehole stresses in anisotropic elastic rock. Int. J. Rock Mech. Min. Sci.; 51:53-63.

Gallant, C., Zhang, J., Wolfe, C.A., Freemann, J., Al-Bazali, T., Reese, M., 2007. Wellbore stability considerations for drilling high-angle wells through finely laminated shale: a case study from Terra Nova. SPE 110742-MS.

Gasc-Barbier, M., Chanchole, S., Berest, P., 2004. Creep behavior of Bure clayey rock. Appl. Clay Sci.; 26(1-4):449–458.

Gasparik, M., Bertier, P., Gensterblum, Y., Ghanizadeh, A., Krooss, B.M., Littke, R., 2014. Geological controls on the methane storage capacity in organic-rich shales. Int. J. Coal Geol.; 123, 34–51.

Gazaniol, D., Forsans, T., Boisson, M.J.F., Piau, J-M., 1995. Wellbore failure mechanisms in shales: prediction and prevention. J. Pet. Technol.; 47(7): 589-595.

Gebrande, H., 1982. Elastic wave velocities and constants of elasticity of rocks and rock forming minerals. In: Angenheister, G. (Ed.), Landolt-Börnstein, Numerical Data and Functional Relationships in Science And Technology 7 (1) Physical Properties of Rocks. *Springer.*

Ghanizadeh, A., Amann-Hildenbrand, A., Gasparik, M., Gensterblum, Y., Krooss, B. M., Littke, R., 2014b. Experimental study of fluid transport processes in the matrix system of the European organic-rich shales: II. Posidonia shale (Lower Toarcian, northern Germany. Int. J. Coal Geol.; 123, 20–33.

Ghanizadeh, A., Gasparik, M., Amann-Hildenbrand, A., Gensterblum, Y., Krooss, B. M., 2014a. Experimental study of fluid transport processes in the matrix system of the

European organic-rich shales: I. Scandanavian Alum shale. Mar. Pet. Geol.; 51: 79-99.

Gholami, R., Moradzadeh, A., Rasouli, V., Hanachi, J., 2014. Practical application of failure criteria in determining safe mud weight windows in drilling operations. J. Rock Mech. Geotech. Eng.; 6(1):13–25.

Gholami, R., Rasouli, V., 2014. Mechanical and elastic properties of transversely isotropic shale. Rock Mech. Rock Eng.; 47(5):1763–1773.

Glorioso, J.C., Rattia, A., 2012. Unconventional Reservoirs: Basic Petrophysical Concepts for Shale Gas. SPE Paper 153004, p. 38.

Goebel, T.H.W., Becker, T.W., Schorlemmer, D., Stanchits, S., Sammis, C., Rybacki, E., Dresen, G., 2012. Identifying fault heterogeneity through mapping spatial anomalies in acoustic emission statistics. J. Geophys. Res.; 117, B03310.

Grieser, B., Bray, J., 2007. Identification of Production Potential in Unconventional Reservoirs, SPE Paper 106623: 6.

Guenot, A., 1989. Borehole breakouts and stress fields International. J. Rock Mech. Min. Sci.; 26(3–4): 185–95.

Gupta, D., Zaman, M., 1999. Stability of boreholes in a geologic medium including the effects of anisotropy. Appl. Math. Mech.; 20(8): 837-866.

H

Haimson, B. C., 2001. Fracture-like borehole breakouts in high-porosity sandstone: Are they caused by compaction bands? Physics and Chemistry of the Earth, Part A: Solid Earth and Geodesy; 26(1-2): 15–20.

Haimson, B. C., 2003. Borehole Breakouts in Berea Sandstone Reveal a New Fracture Mechanism. Pure and Applied Geophysics; 160(5): 813–831.

Haimson, B., Kovacich, J., 2003. Borehole instability in high-porosity Berea sandstone and factors affecting dimensions and shape of fracture-like breakouts. Engineering Geology; 69: 219-231.

Haimson, B., Lee, H., 2004. Borehole breakouts and compaction bands in two high-porosity sandstones. Int. J. Rock Mech. Min. Sci.; 41(2): 287–301.

Haimson, B.C., Song, I., 1993. Laboratory study of borehole breakouts in Cordova Cream: a case of shear failure mechanism. Int. J. Rock Mech. Min. Sci.; 30(7): 1047–56.

Heidbach, O., Tingay, M., Barth, A., Reinecker, J., Kurfeß, D., Müller, B., 2008. The World Stress
Map database release 2008.

Helm, D., 2013. All change: the Unfolding Geopolitics of Oil and Gas in the US and the Middle East.

Hoek, E., 1999. Support for very weak rock associated with fault and shear zones. In:International Symposium on Rock Support and Reinforcement Practice in Mining, Kalgoorlie, Australia.

Horsfield, B., Scheck-Wenderoth, M., Krautz, H.J., Mitti, M., 2010. Geoenergy: from visions to solutions. Geochemistry; 70(S3): 1.

Horsfield, B., Schulz, H-M., 2010. Die Rolle von Shale-Gas im europäischen Energiemix: Forschungsschwerpunkte, Methoden, Neue Entwicklungen, Presentation at the EnergieMix 2050, Berlin, Germany.

Horsrud, P., 2001. Estimating Mechanical Properties of Shale from Empirical Correlations. SPE Paper 56017: 68–73.

Horsrud, P., Sonstebo, E.F., Boe, R., 1998. Mechanical and petrophysical properties of North Sea shales. Int. J. Rock Mech. Min. Sci.; 35(8): 1009–1020.

Hoskins, E., 1969. The failure of thick-walled hollow cylinders of isotropic rock. Int. J. Rock Mech. Min. Sci.; 6(1): 99–125.

Hunsche, U., Walter, F., Schnier, H., 2004. Evolution and failure of the Opalinus clay: relationship between deformation and damage, experimental results and constitutive equation. Appl. Clay Sci.; 26(1-4): 403–411.

Hwu, C., 2010. Anisotropic Elastic Plates. *Springer.*

I

Ibanez, W.D., Kronenberg, A.K., 1993. Experimental deformation of shale: mechanical properties and microstructural indicators of mechanisms. Int. J. Rock Mech. Min. Sci. Geomech. Abstr.; 30(7): 723–734.

Islam, Md.A., Skalle, P., 2013. An experimental investigation of shale mechanical properties through drained and undrained test mechanisms. Rock Mech. Rock Eng.; 46(6): 1391–1413.

J

Jaeger, J.C., Cook, N.G.W., Zimmerman, R.W., 2007. Fundamentals of rock mechanics. Imaging, 4th edn. *Blackwell.*

Jarvie, D.M., Hill, R.J., Ruble, T.E., Pollastro, R.M., 2007. Unconventional shale-gas systems: the Mississippian Barnett shale of north-central Texas as one model for thermogenic shale-gas assessment. AAPG Bull.; 91:, 475–499.

Ji, S., 2004. A generalized mixture rule for estimating the viscosity of solid–liquid suspensions and mechanical properties of polyphase rocks and composite materials. J. Geophys. Res.; 109, B10207.

Ji, S., Wang, Q., Xia, B., Marcotte, D., 2004. Mechanical properties of multiphase rocks: a phenomenological approach using generalized means. J. Struct. Geol.; 26(8): 1377–1390.

Ji, S., Zhao, P., 1994. Strength of two-phase rocks: a model based on fiber-loading theory. J. Struct. Geol.; 16(2): 253–262.

Jochum, J., Friedrich, G., Leythaeuser, D., Littke, R., Ropertz, B., 1995. Hydrocarbon-bearing fluid inclusions in calcite-filled horizontal fractures from mature Posidonia Shale (Hils Syncline, NW Germany). Ore Geol Rev; 9: 363–70.

Johnston, D.H., 1987. Physical properties of shale at temperature and pressure. Geophys.; 52(10): 1391–1401.

Johnston, J.E., Christensen, N.I., 1995. Seismic anisotropy of shales. J. Geophys. Res.; 100(B4):5991-6003.

Jordan, P., Nüesch, R., 1989. Deformational behavior of shale interlayers in evaporate detachment horizons, Jura overthrust, Switzerland. J. Struct. Geol.; 11(7):859–871.

K

Kaiser, P.K., Morgenstern, N.R., 1985. Deformation of small tunnels - IV. Behaviour during failure. Int. J. Rock Mech. and Min. Sci. & Geomech. Abstr.; 22(3): 141-152.

Kaufhold, A., Gräsle, W., Plischke, I., Dohrmann, R., Siegesmund, S., 2013. Influence of carbonate content and micro-fabrics on the failure strength of the sandy facies of the Opalinus Clay from Mont Terri (Underground Rock Laboratory). Eng. Geol.; 156: 111–118.

Keller, L.M., Holzer, L., Wepf, R., Gasser, P., 2011. 3D geometry and topology of pore pathways in Opalinus clay: Implications for mass transport. Appl. Clay Sci.; 52(1–2): 85–95.

Kerschke, D. I., Schulz, H.-M., 2015. Sedimentological and Diagenetic Controls of Gas in Lower and Early Upper Carboniferous Sediments, NE Germany. Sedimentary Geology; 325: 192-209.

Khan, S., Ansari, S., Han, H., Khosravi, N., 2011. Importance of shale anisotropy in estimating in-situ stresses and wellbore stability analysis in Horn River basin. SPE Int CSUG/SPE.

Kirsch, G., 1898. Die Theorie der Elastizität und die Bedürfnisse der Festigkeitslehre. Zeitschrift des Vereins Deutscher Ingenieure, 42: 797-807.

Klein, E., Baud, P., Reuschle, T., Wong, T-F., 2001. Mechanical behaviour and failure mode of Bentheim sandstone under triaxial compression. Phys. Chem. Earth; 26(1–2): 21–5.

Kronenberg, A.K., Kirby, S.H., Pinkston, J., 1990. Basal slip and mechanical anisotropy of biotite. J. Geophys. Res.; 95: 19257–19278.

Kuila, U., Dewhurst, D.N., Siggins, A.F., Raven, M.D., 2011. Stress anisotropy and velocity anisotropy in low porosity shale. Tectonophysics; 503: 34–44.

Kwon, O., Kronenberg, A.K., 1994. Deformation of Wilcox Shale: Undrained Strength and Effects on Strain Rate. ARMA Papers. 1994-0757, p. 9.

L

Labiouse, V., Sauthier, C., You, S., 2014. Hollow cylinder simulation experiments of galleries in Boom Clay formation. Rock Mech. Rock Eng.; 47(1): 43-55.

Labiouse, V., Vietor, T., 2014. Laboratory and in situ simulation tests of the excavation damaged zone around galleries in opalinus clay. Rock Mech. Rock Eng.; 47(1): 57-70.

Lee, H., 2005. Borehole breakouts in arkosic sandstones and quartz- rich sandstones. Ph.D. thesis, University of Wisconsin-Madison.

Lee, H., Ong SH., Azeemuddin, M., Goodman, H. 2012. A wellbore stability model for formations with anisotropic rock strengths. J. Pet. Sci. Eng.; 96-97: 109-119.

Lekhnitskii, S.G., 1968. Anisotropic plates. *Gordon and Breach Science Publishers.*

Littke, R., Baker, D.R., Leythaeuser, D., 1988. Microscopic and sedimentologic evidence for the generation and migration of hydrocarbons in Toarcian source rocks of different maturities. Org. Geochem.; 13(1-3): 549-559.

Littke, R., Krooss, B., Uffmann, A.K., Schulz, H.M., Horsfield, B., 2011. Unconventional gas resources in the Paleozoic of Central Europe. Oil Gas Sci. Technol.; 66: 953–977.

Littke, R., Leythaeuser, D., Rullkotter, J., Baker DR., 1991. Keys to the depositional history of the Posidonia Shale (Toarcian) in the Hils Syncline, northern Germany. Geological Society, London, Special Publication, vol. 58.

Lockner, D.A., 1995. Rock failure. In: Ahrens, T.J. (Ed.), Rock Physics and Phase Relations: A Handbook of Physical Constants 3. AGU Reference Shelf, Washington, pp. 127–147.

Lutterotti, L., Bortolotti, M., Ischia, G., Lonardelli, I., Wenk, H-R., 2007. Rietveld texture analysis from diffraction images. Z. Kristallogr. Supplements; 26: 125–30.

M

Mann, U., Duppendecker, S., Langen, A., Ropertz, B., Welte, D.H., 1990. Pore network evolution of the lower toarcian posidonian shale during petroleum generation and expulsion—a multidisciplinary approach. Zbl Geologische Palaontologie Teil I 8: 1051-1071.

Martin, C.D., Lanyon, G.W., 2003. Measurement of in situ stress in weak rocks at Mont Terri Rock Laboratory, Switzerland. Int. J. Rock Mech. Min. Sci.; 40(7-8): 1077-1088.

Masri, M., Sibai, M., Shao, J.F., Mainguy, M., 2014. Experimental investigation of the effect of temperature on the mechanical behavior of Tournemire shale. Int. J. Rock Mech. Min. Sci.; 70: 185–191.

Maury, V.M., Sauzay, J-M., 1987. Borehole instability: case history, rock mechanics approach, and results. SPE/IADC, vol. 16051, p. 11–24.

Mavko, G., Mukerji, T., Dvorkin, J., 2009. The Rock Physics Handbook: Tools for Seismic Analysis of Porous Media. Cambridge University Press, *Cambridge.*

McClintock, F.A., Walsh, J.B., 1962. Friction of Griffith cracks in rock under pressure. In: Proceedings of 4th US Congress of Applied Mechanics, American Society of Mechanical Engineers, p. 1015–21.

McGlade, C., Speirs, J., Sorrell, S., 2013. Unconventional gas – a review of regional and global resource estimates. Energy 55: 571–584.

Meier, T., Rybacki, E., Backers, T., Dresen, G., 2015. Influence of bedding angle on borehole stability: a laboratory investigation of transverse isotropic oil shale. Rock Mech. Rock Eng.; 48: 1535–1546.

Meier, T., Rybacki, E., Reinicke, A., Dresen, G., 2013. Influence of borehole diameter on the formation of borehole breakouts in black shale. Int. J. Rock Mech. Min. Sci.; 62: 74-85.

Meier, T., Rybacki, E., Backers, T., Dresen, G., 2015b. Laboratory and Numerical Investigation on Borehole Stability in Shales. Proceedings of the Geomechanical and Petrophysical Properties of Mudrocks Workshop at the Geological Society of London.

N

Naumann, M., Hunsche, U., Schulze, O., 2007. Experimental investigations on anisotropy in dilatancy, failure and creep of Opalinus clay. Phys. Chem. Earth; 32: 889–895.

Niandou, H., Shao, J.F., Henry, J.P., Fourmaintraux, D., 1997. Laboratory investigation of the mechanical behaviour of Tournemire shale. Int. J. Rock Mech. Min. Sci.; 34: 3–16.

O

Økland, D., Cook, J.M., 1998. Bedding-related borehole instability in high-angle wells. In: SPE/ISRM rock mechanics in petroleum engineering, 8-10 July, Trondheim, Norway. SPE/ISRM; 47285: 413–22.

Ong, S.H., Roegiers, J-C., 1993. Influence of anisotropies in borehole stability. Int. J. Rock Mech. Min. Sci. Geomech. Abstr.; 30(7): 1069-1075.

Ong, S.H., Roegiers, J-C., 1996. Fracture initiation from inclined wellbores in anisotropic formations. J. Pet. Technol.; 612-619.

Ottesen, S., 2010. Wellbore stability in fractured rock. In: IADC/SPE drilling conference and exhibition; 128728: 1-8.

P

Papamichos, E., 2010. Borehole failure analysis in a sandstone under anisotropic stresses. Int. J. Numer. Anal. Methods Geomech.; 34(6): 581–603.

Papamichos, E., Tronvoll, J., Skjxrstein, A., Unander, T.E., 2010. Hole stability of Red Wildmoor sandstone under anisotropic stresses and sand production criterion. J. Pet. Sci. Eng.; 72(1-2): 78-92.

Papamichos, E., van den Hoek, P.J., 1995. Size dependency of Castlegate and Berea sandstone hollow-cylinder strength on the basis of bifurcation theory. In: Daemen JJK, Schultz RA, (editors). Proceedings of 35th US Symp on RockMechanics, Lake Tahoe, CA, Rock Mechanics, Balkema, Rotterdam, p.301–06.

Papanastasiou, P., Vardoulakis, I., 1992. Numerical treatment of progressive localization in relation to borehole stability. Int. J. Numer. Anal. Meth. Geomech.; 16(6): 389–424.

Pasic, B., Gaurina-Medimurec, N., Matanovic, D., 2007. Wellbore instability: causes and consequences. Rud-Geol-Naftnizbornik; 19: 87–98.

Paterson, M.S., 1970. A high-pressure, high-temperature apparatus for rock deformation. Int. J. Rock Mech. Min. Sci.;7: 517–526.

Pei, J., 2008. Strength of transversely isotropic rocks. Doctoral dissertation, Massachusetts Institute of Technology.

Peltonen, C., Marcussen, O., Bjorlykke, K., Jahren, J., 2009. Clay mineral diagenesis and quartz cementation in mudstones: the effects of smectite to illite reaction on rock properties. Mar. Pet. Geol.; 26: 887–898.

Perras, M.A., Diederichs, M. S., 2016. Predicting excavation damage zone in brittle rocks. J. Rock Mech. and Geotechn. Eng.; 8(1): 60-74.

Peters, K.E., Walters, C.C., Moldowan, J.M., 2008. Biomarker Guide: Biomarkers and isotopes in the environment and human history, 2nd ed. (Volume 1). *Cambridge University Press.*

Petley, D.N., 1999. Failure envelopes of mudrocks at high-confining pressure. Geol. Soc. Lond. Spec. Publ.; 158: 61–71.

Popp, T., Salzer, K., 2007. Anisotropy of seismic and mechanical properties of Opalinus clay during triaxial deformation in a multi-anvil apparatus. Phys. Chem. Earth; 32(8-14): 879–888.

Priskila, L.M., 2014. Evaluation of Fishbone Lateral Stimulation. Norwegian University of Science and Technology.

Q

R

Rahimi, R., 2014. The effect of using different rock failure criteria in wellbore stability analysis. Master Theses 7270. Missouri University.

Rahmati, E., Nouri, A., Fattahpour, V., 2014. Caprock Integrity Analysis During a SAGD Operation Using an Anisotropic Elasto-Plastic Model. SPE Paper 170114, p. 23.

Rahmati, E., Nouri, A., Fattahpour, V., Trivedi, J., 2015. Numerical Assessment of the Maximum Operating Pressure for Anisotropic Caprock in SAGD Projects. SPE Paper 174509, p.21.

Reinicke, A., 2009. Mechanical and hydraulic aspects of rock-proppant systems — laboratory experiments and modelling approaches. Ph.D. thesis, University of Potsdam.

Reinicke, A., Rybacki, E., Stanchits, S., Huenges, E., Dresen, G., 2010. Hydraulic fracturing stimulation techniques and formation damage mechanisms – implications from laboratory testing of tight sandstone – proppant systems. Geochemistry; 70(S3): 107–117.

Riekman, R., Mullen, M., Grieser, B., Kundert, D., 2008. A Practical Use of Shale Petrophysics for Stimulation Design Optimization: All Shale Plays are not Clones of the Barnett Shale. SPE Paper 115258, p. 11.

Röhl, H-J., Schmid-Röhl, A., 2005. Lower Toarcian (Upper Liassic) black shales of the central European epicontinental basin: A sequence stratigraphic case study from the SW German Posidonia shale. Deposition of Organic-Carbon-Rich Sediments: Models, Mechanisms, and Consequences, SEPM Special Publication; 82: 165-189.

Röhl, H-J., Schmid-Röhl, A., Osmann, W., Frimmel, A., Schwark, L., 2001. The Posidonia Shale (Lower Toarcian) of SW-Germany: an oxygen-depleted ecosystem controlled by sea level and palaeoclimate. Palaeogeography, Palaeoclimatology, Palaeoecology; 165: 27-52.

Rummel, F., 1982. Fracture and flow of rocks and minerals. In: Angenheister, G. (Ed.), Landolt-Börnstein, Numerical Data and Functional Relationships in Science and Technology 7 (1) Physical Properties of Rocks. Springer, Berlin, pp. 141–238.

Russell, K.A., Ayan, C., Hart, N.J., Rodriguez, J.M., Scholey, H., Sugden, C., Davidson, J.K., 2003. Predicting and preventing wellbore instability using the latest drilling and logging technologies: Tullich Field Development, North Sea. In: SPE annual technical conference and exhibition, 5-8 October, Denver, Colorado.

Rybacki, E., Meier, T., Dresen, G., 2016. What controls the mechanical properties of shale rocks? - Part II: Brittleness. J. Petr. Sci. Eng.; 144: 39-58.

Rybacki, E., Morales, L.F.G., Naumann, M., Dresen, G., 2014. Strain localization during high temperature creep of marble: the effect of inclusions. Tectonophysics; 634: 182–197.

Rybacki, E., Reinicke, A., Meier, T., Makasi, M., Dresen, G., 2015. What controls the mechanical properties of shale rocks? - Part I: strength and elasticity. J. of Petr. Sci. and Eng.; 135: 702-722.

S

Santarelli, F.J., Brown, E.T., 1989. Failure of three sedimentary rocks in triaxial and hollow cylinder compression tests. Int. J. Rock Mech. Min. Sci.; 26(5): 401–13.

Schmitt, L., Forsans, T., Santarelli, F.J., 1994. Shale testing and capillary phenomena. Int. J. Rock Mech. Min. Sci. Geomech. Abstr.; 31: 411–427.

Schmitt, R.D., Currie, C.A, Zhang, L., 2012. Crustal stress determination from boreholes and rock cores: Fundamental principles, Tectonophysics; 580: 1-26.

Schon, J.H., 2004. Physical properties of rocks: Fundamentals and principles of petrophysics. 1st ed. *Elsevier.*

Schwark, L., Frimmel, A., 2004. Chemostratigraphy of the Posidonia Black Shale, SW-Germany II. Assessment of extent and persistence of photic-zone anoxia using aryl isoprenoid distributions. Chemical Geology; 206: 231-248.

Seedsman, R.W., 1987. Strength implications of the crystalline and osmotic swelling clays shales. Int. J. Rock Mech. Min. Sci. Geomech. Abstr.; 24: 357–363.

Seidle, J., 2011. Fundamentals of Coalbed Methane Reservoir Engineering. Pennwell, Tulsa, p. 387.

Sheoerey, P.R., 1997. Empirical Rock Failure Criteria. *Balkema.*

Skelton, J., Hogg, T.W., Cross, R., Verheggen, L., 1995. Case history of directional drilling in the Cusiana Field in Colombia. In: SPE/ IADC drilling conference, Amsterdam, Netherlands.

Soliman, M.Y., Daal, J., East, L., 2012. Fracturing unconventional formations to enhance productivity. J. Nat. Gas Sci. Eng.; 8: 52–67.

Sondergeld, C.H., Newsham, K.E., Comisky, J.T., Rice, M.C., Rai, C.S., 2010. Petrophysical Considerations in Evaluating and Producing Shale Gas Resources. SPE Papers 131768, p. 34.

Sone, H., Zoback, M.D., 2013a. Mechanical properties of shale-gas reservoir rocks –Part 2: ductile creep, brittle strength, and their relation to the elastic modulus. Geophys. 78, D393–D402.

Sone, H., Zoback, M.D., 2013b. Mechanical properties of shale-gas reservoir rocks –Part 1: Static and dynamic elastic properties and anisotropy. Geophysics 78,D381–D392.

Sone, H., Zoback, M.D., 2014. Time-dependent deformation of shale gas reservoir rocks and its long-term effect on the in situ stress state. Int. J. Rock Mech. Min. Sci.; 69: 120–132.

Song, I., 1998. Borehole breakouts and core disking in Westerly granite: Mechanisms of formation and relationship to in situ stress. Ph.D. thesis, University of Wisconsin-Madison.

Speight, J.G., 2013. Shale Gas Production Processes. *Elsevier.*

Steiger, R.P., 1993. Advanced triaxial swelling tests of preserved shale cores. Int. J. Rock Mech. Min. Sci. Geomech. Abstr.; 30: 681–685.

Stephansson, O., Zang, A., 2012. ISRM Suggested Methods for Rock Stress Estimation—Part 5: Establishing a Model for the In Situ Stress at a Given Site. Rock Mech. Rock Eng.; 45: 955–969.

Stöckhert, F., Molenda, M., Brenne, S., Alber, M., 2015. Fracture propagation in sandstone and slate – Laboratory experiments, acoustic emissions and fracture mechanics. J. Rock Mech. Geotech. Eng.; 7(3): 237-249.

Swan, G., Cook, J., Bruce, S., Meehan, R., 1989. Strain rate effects in Kimmeridge Bay shale. Int. J. Rock Mech. Min. Sci. Geomech. Abstr.; 26: 135–149.

T

Takahashi, M., Kiode, H., 1989. Effect of the intermediate principal stress on the strength and deformation behavior of sedimentary rocks at the depth shallower than 2000 m. In: Maury, V., Fourmaintraux, D. (Eds.), Rock at Great Depth. Balkema, Rotterdam, pp. 19–26.

Thyagaraj, T., Rao, S.M., 2013. Osmotic swelling and osmotic consolidation behavior of compacted expansive clay. Geotech. Geol. Eng.; 31: 435–445.

Timoshenko, S., Goodier, J.N., 2010. Theory of Elasticity, *Mcgraw Hill Education Private Limited.*

U

V

Van den Hoek, P, Smit, D-J., Kooijman, A.P., deBree, P., Kenter, C.J., Khodaverdian, M., 1994. Size-dependency of hollow-cylinder stability.Eurock'94. Rotterdam: Balkema; 191–7.

Van den Hoek, P.J., Kooijman, A.P., Kenter, C.J., Khodaverdian, M., Hyland, C.R., McLennan, J.D., 1992. Size-dependency of hollow cylinder collapse strength. SPE J 24800:351–5.

Van Oort, E., 2003. On the physical and chemical stability of shales. J. Pet. Sci. Eng.; 38, 213–235.

Vernik, L., Liu, X., 1997. Velocity anisotropy in shales; a petrophysical study. Geophysics; 62(2): 521-532.

Vernik, L., Zoback, M.D., 1990. Strength anisotropy in crystalline rock: implications for assessment of in situ stresses from wellbore breakouts. In: The 31th US symposium on rock mechanics (USRMS), 18-20 June, Golden, Colorado, pp 841-848.

W

Wang, F.P., Gale, J.F.W., 2009. Screening criteria for shale-gas systems. Gulf Coast Assoc. Geol. Soc. Trans.; 59: 779–793.

Wang, J.J., Zhu, J.G., Chiu, C.F., Zhang, H., 2007. Experimental study on fracture toughness and tensile strength of clay. Eng. Geol.; 94: 65–75.

Wang, Y., Dusseault, M.B., 1994. Stresses Around a Circular Opening in an Elastoplastic Porous Medium Subjected to Repeated Hydraulic Loading. Int. J. Rock Mech. Min. Sci.; 31(6): 591-616.

Warpinski, N.R., Mayerhofer, M.J., Vincent, M.C., Cipolla, C.L., Lolon, E.P., 2008. Stimulating Unconventional Reservoirs: Maximizing Network Growth While Optimizing Fracture Conductivity. SPE Paper 114173, p. 19.

Wenk, H-R., Voltolini, M., Kern, H., Popp, T., Mazurek, M., 2008. Anisotropy in shale from Mont Terri. Lead Edge 2: 742-748.

Wenk, H-R., Voltolini, M., Mazurek, M., Van Loon, L.R., Vinsot, A., 2008. Preferred orientations and anisotropy in shales: Callovo-oxfordian shale (France) and Opalinus clay (Switzerland). Clays Clay Miner.; 56(3): 285–306.

Willson, S.M., Last, N.C., Zoback, M.D., Moos, D., 1999. Drilling in South America: a wellbore stability approach for complex geologic conditions. In: Latin American and Caribbean petroleum engineering conference, 21-23 April, Caracas, Venezuela.

X

Xing, G., Guo, F., Song, C., Sun, Y., Yu, J., Wang, G., 2012. Fishbone Well Drilling and Completion Technology in Ultra-thin Reservoir. SPE-155958-MS.

Y

Yale, D.P., Jamieson, W.H., 1994. Static and Dynamic Rock Mechanical Properties in the Hugoton and Panoma Fileds, Kansas, SPE Paper, SPE 27939, pp. 209–219.

Z

Zang, A., Stephansson, O., 2010. Stress field of the Earth's crust. *Springer.*

Zhang, J., Wong, T-F., Davis, D.M., 1990. Micromechanics of pressure-induced grain crushing in porous rocks. J. Geophys. Res.; 95(B1): 341–52.

Zhou, Y., Rybacki, E., Wirth, R., He, C., Dresen, G., 2012. Creep of partially moltenfine-grained gabbro under dry conditions. J. Geophys. Res. 117, B05204.

Zoback, M.D., 2007. Reservoir geomechanics. *Cambridge University Press.*

Zoback, M.D., 2010. Reservoir geomechanics. *Cambridge University Press.*

Zoback, M.D., Moos, D., Mastin, L., 1985. Well bore breakouts and in situ stress. J. Geophys. Res; 90(B7): 5523-5530.

Zoback, M., Kitasei, S., Copithoren, B., 2010. Addressing the Environmental Risks from Shale Gas Development. Briefing Paper 1, World Watch Institute Natural Gas and Sustainable Energy Initiative.